Thermal Modeling Validation Techniques for Thermoset Polymer Matrix Composites

by

Nathan Avery Slesinger

A thesis submitted in partial fulfillment of the requirements for the degree of

MASTER OF APPLIED SCIENCE

in

The Faculty of Graduate Studies

(Materials Engineering)

THE UNIVERSITY OF BRITISH COLUMBIA

(Vancouver)

July 2010

Abstract

Process modeling is becoming a widely-accepted tool to reduce the time, cost, and risk in producing increasingly large and complicated composite structures. Process modeling reduces the need for physical parts, as it is not practical or economical to design and fabricate large composite structures using a trial-and-error approach. The foundation of the composite manufacturing process, and thus of process models, is the thermal history of the composite part during cure. Improperly curing the composite part will compromise its mechanical properties. Consequently, proper validation of the thermal model input parameters is critical, since the simulation output depends on the accuracy of the input. However, there are no standard methods to validate thermal process model input parameters.

In this work, repeatable and robust methods were developed to isolate and validate the conductive heat transfer, thermochemical, and convective heat transfer sub-models. By validating the sub-models, the uncertainty of the complete thermal simulation was significantly reduced. Conductive and thermochemical material models were validated by comparing the thermal response of a material surrounded by rubber bricks to a 1-D simulation of the same materials. Four composite prepreg systems and their respective material models were tested, with agreement ranging from excellent (errors less than 1.0 °C) to poor (errors greater than 5.0 °C).

Calorimetery, visual monitoring, and CFD were used to characterize the convective heat transfer environment inside the UBC autoclave. The validation methods were also used to better understand the capabilities and limitations of the autoclave. Local variations in airflow patterns and heat transfer coefficients showed that heat transfer can be highly variable in an individual piece of equipment. Simple procedures for characterization of an autoclave or oven were demonstrated.

The developed methods can be used individually, or in combination, to validate thermal models and reduce uncertainties associated with the cure of composites. With further refinement, the demonstrated methods can be developed into validation standards for thermal modeling of composite materials.

Preface

The work that appears in this thesis is that of the author. However, some of the material in this thesis has been reproduced and/or adapted from previously published papers. This author was the primary author of all of the papers, and said papers were based off of this author's work. This author would like to acknowledge Abdul Arafath and Takayuki Shimizu for helping to develop the HTC measurement techniques and editing the 2009 paper. Also, acknowledgement is due to Anoush Poursartip and Göran Fernlund for their assistance in writing and editing final drafts of the 2010 papers. The publications are:

Slesinger, N., Shimizu, T., Arafath, A.R.A, Poursartip, A. (2009). Heat Transfer Coefficient Distribution Inside and Autoclave. *17th International Conference on Composite Materials, July 2009,* Edinburgh, UK.

Slesinger, N., Fernlund, G., Poursartip, A. Development of a Test Method to Validate Cure Kinetics Models Used in Process Simulation. (2010). *2010 SAMPE Spring Conference, May 2010,* Seattle, WA.

Slesinger, N., Fernlund, G., Poursartip, A. Simple Visualization of Autoclave Airflow Using Wireless Cameras. (2010) *2010 SAMPE Spring Conference, May 2010,* Seattle, WA.

Table of Contents

List of Tables

List of Figures

Nomenclature

A	area
Bi	Biot number
C_p	specific heat capacity
h	convective heat transfer coefficient
H_R	heat of reaction
k	thermal conductivity
k_{11}	longitudinal thermal conductivity
k_{22}	transverse thermal conductivity
L	length
m	mass
Pr	Prandtl number
q	heat flux
Re	Reynold's number
t	time
T	temperature
ΔT_s	difference between surface and surrounding fluid temperatures
V_f	Fiber volume fraction
x	length coordinate
α	thermal diffusivity (for heat transfer), or degree of cure (for cure kinetics)
μ_∞	free-stream fluid velocity
ρ	density
ν	kinematic viscosity
ζ	dimensionless thickness coordinate

Acknowledgements

I wish first to thank my supervisor, Dr. Anoush Poursartip, for all the mentoring, guidance, ideas, and assistance he offered me for the duration of this work. Dr. Göran Fernlund, Dr. Reza Vaziri, and Dr. Daan Maijer are three other UBC faculty members to whom I owe thanks for their thoughtful discussions, excellent teaching, and feedback on my work. Dr. Abdul Arafath, for spending many hours helping me with finite-element models and codes; without his assistance, many of my numerical results would not exist. Thanks to Dr. Anthony Floyd, who graciously handled my many software questions and bug reports.

I also offer much thanks to numerous other past, present, and future members of the UBC Composites group, including Takayuki Shimizu, Roger Bennett, Malcolm Lane, David Van Nee, Bryan Louis, Steven Zacharski, Leyla Farhang, Alireza Forghani, Dr. Navid Zobeiry, and Robert Courdji.

Finally, I would like to thank my family for their encouragement throughout this endeavor, but a special thanks to three people: my wife, Leanne, for patiently indulging my quest for knowledge while I uprooted her for several years; my father, Jeff, for much sound advice and inspiration; and my grandfather, Dr. Edward Wellin, who provided insightful commentary and spent many hours editing my writing.

Dedication

To my wife, my mother, and my grandmother - the three women who made all this possible with their generosity, patience, and love.

1 Introduction

The use of fiber-reinforced composite materials has been steadily increasing over the last two decades as the material systems and manufacturing methods have matured. Although composites can now be found in consumer goods, the push continues for higher performance, faster manufacturing, and lower costs in increasingly demanding applications. It is therefore becoming less efficient to design and produce composite structures using trial-and-error or parametric experimental development methods. To overcome the inefficiencies, process modeling techniques can be used to simulate the manufacturing process in a virtual environment and provide data for analysis and optimization with a reduced need for physical parts. Accurately modeling the thermal response is critical, since the thermal response of the composite during cure is the foundation for the final composite properties.

The thermal response of the composite cure assembly (consisting of a part, tool, and vacuum-bagging materials) is a coupled convective heat transfer, conductive heat transfer, and thermochemical problem. Fibers, typically carbon or glass, are covered by a polymer-matrix, typically epoxy or polyester, which solidifies during cure. For curing, heat is typically applied to the cure assembly through forced convection in ovens or autoclaves. The heat on the surfaces is transferred through the thickness of the cure assembly, making the thermal response a conduction problem through the cure assembly. The resulting chemical reaction of the thermoset cure generates internal heat. The response of the composite over the entire cycle (the thermal history) can be an indicator of the quality of the cure. Proper cure of the matrix material is critical, because the composite properties increase by up to six orders of magnitude during the cure process (Roberts, 1987).

Although no standard procedure currently exists for validating thermochemical, conductive, and convective composite material models, many different aspects of the composite cure process are modeled using widely available 1-, 2-, and 3-Dimensional finite element software packages and material property data. The chemical problem is challenging to validate because the response of the composite must be isolated from the multiple additional materials required for a composite lay-up. Validating the heat transfer problem is also difficult because the convective environment in the autoclave or oven has poorly oriented and highly turbulent airflow.

A 1-D method for validation of the thermochemical and conductive heat transfer models, which overcomes the above challenges, is presented in this work. A flat laminate is insulated in such a

way that heat transfer is 1-D through the thickness and the laminate is placed between two rubber bricks of known thermal properties. The bricks isolate the response of the laminate and calibrate the conductive boundaries on the laminate and rubber brick model. The uncertainty of the heat transfer coefficient (HTC) boundary is reduced by using set-temperature boundaries from recorded thermocouple data. The test, however, remains a robust test of the model because the boundaries on the composite are free; the boundaries are driven by the lag through the calibrated bricks.

Several methods for measuring convective heat transfer boundaries and for determining airflow patterns are also presented in this work. The measurements can also be used to characterize autoclave or oven performance. Because of the individuality of equipment designs, the capabilities and limitations for a specific autoclave or oven are frequently unknown or ignored. The methods can be used individually for a basic understanding, or together for a more detailed understanding of the convective heat transfer environment. The uncertainty associated with process simulation of the composite cure process is significantly reduced with the validation of the composite material model and an increased understanding of the convective boundaries.

1.1 Scope and Objectives

The two primary objectives of this work are to reduce uncertainties in process modeling by:

- Developing robust and reliable methods for experimentally validating thermochemical and conductive heat transfer sub-models of thermoset polymer-matrix prepreg composite materials.
- Reducing uncertainties associated with the convective sub-model and characterization of an autoclave or oven by developing techniques for qualitative airflow visualization, and quantitative HTC measurement.

2 Background

The thermal history of a cured composite is a coupled problem that can be broken down into conductive, thermochemical, and convective heat transfer components. Heat transfer through the cure assembly is through conduction, and the chemical reaction of the cure process generates internal heat. The environment surrounding the cure assembly is forced convection in an autoclave or oven. Each model component has an associated level of uncertainty, and the uncertainty compounds when the three components are combined into a complete thermal simulation. Figure 2-1 is the cure assembly and the modes of heat transfer through a 1-D system. The rate of internal heat generation in the composite depends not only on how quickly it is heated by the surrounding materials, but also how quickly those materials remove the heat through conduction and how quickly the surrounding convective environment removes the heat from the assembly. Proper validation of the thermal model against experimental data is needed to manage the uncertainty of the thermal simulation.

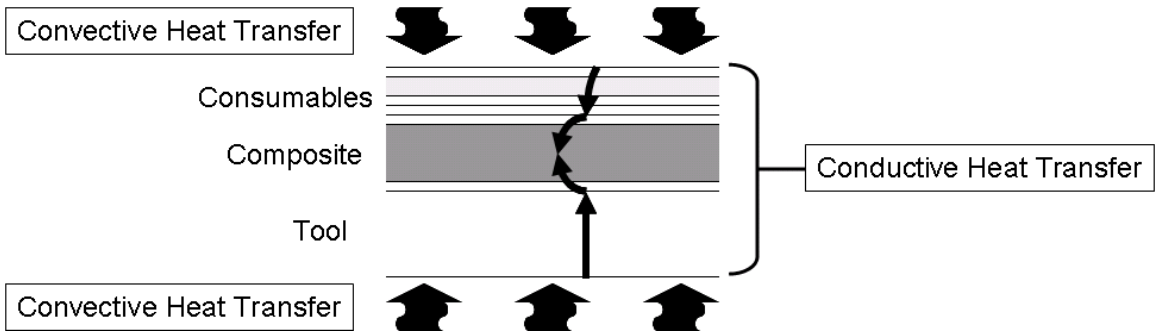

Figure 2-1: Coupling of convective and conductive heat transfer for the cure assembly in 1-D.

For this work, the distinction between the terms verification and validation must be stressed. A 2006 guide published by The American Society of Mechanical Engineers (ASME V&V 10-2006, 2006) provides a detailed discussion of the roles of both verification and validation in numerical simulation. Verification confirms whether the mathematical simulation of the solution is correctly implemented. A known set of input parameters should result in a known output for a properly verified simulation. Validation shows whether the simulation is an accurate representation of reality by comparing simulation results to experimental data. According to ASME (2006), a model can be "considered validated . . . once its predetermined requirements for demonstration of accuracy and predictive capability have been fulfilled".

The accuracy requirements will vary depending on the application, but this thesis proposes that an accuracy of ±2.0 °C should be considered the largest allowable error for composites processing validation. Thermocouples (TC) are the most commonly used temperature

measurement tool in composites processing, and standard J-type TCs have a standard limit of error of ±2.2 °C (Omega, 2010d). J-type TCs are inexpensive and the calibration range, 0.0 - 750.0 °C, covers the temperature range of most composite manufacturing processes (MIL-HDBK-17-2F, 2002). Special J-type TCs are available with a standard limit of error of ±1.1 °C if additional accuracy is needed.

High accuracy for model validation is needed because the typical allowable temperature deviation during the isothermal hold portion of the cure cycles is ±5.0 °C (MIL-HDBK-17-3F, 2002). The properties of the cured composite are sensitive to the thermal history of cure, and departing the allowable window means the composite may not have attained the properties around which the part was designed, and it could be unsafe for use.

Process modeling can help to prevent temperature excursions by simulating the thermal history. However, if the uncertainty of the thermochemical model is near the tolerance limit, the predicted temperatures may appear acceptable when they are not. For example, a predicted peak temperature 3.0 °C above the hold temperature, using a model with 4.0 °C of uncertainty, would mean the actual part temperature could vary from the hold temperature by -1.0 °C up to +7.0 °C. A prediction with 2.0 °C of uncertainty makes the model truly valuable to a user; there is room within the tolerance window for other uncertainties that occur during processing such as batch-to-batch material variability and processing equipment variability.

2.1 Thermal Modeling of Composites

A survey of literature shows that, although heat transfer is a well studied field of engineering, the relation of heat transfer to composites and composites processing has been less thoroughly investigated. Thermal modeling of the cure assembly has either traditionally ignored or made gross assumptions about the numerous sources of uncertainty found in composites processing. Major sources of uncertainty in thermal modeling of composites include:

- Ensuring the simulation boundary conditions properly represent processing conditions.
- Accurately measuring and modeling the thermal properties of the multiple materials in the cure assembly such as: density, specific heat capacity, thermal conductivity, and temperature dependant property changes.
- Thermal contact resistances at the interfaces of the materials in the cure assembly.

- Accurately modeling the heat generation during cure at many temperatures and temperature rates.
- The validity of the model at both small (laboratory) scales and large (industrial) scales.
- Highly turbulent and poorly oriented airflow in the autoclave environment.
- Complicated part geometries interfering with local airflow patterns and heat transfer around the cure assembly.

2.1.1 Conductive Heat Transfer

Conductive heat transfer is the transfer of heat through a solid or stationary fluid. Heat applied to a surface changes the temperature through the object as a function of distance and a proportionality constant k (Lienhard, 2006):

$$q = -k\frac{dT}{dx} \tag{2-1}$$

where q is the heat flux, k is the thermal conductivity, and dT/dx is the through-thickness temperature gradient. Increasing the heat flux will increase the through-thickness temperature gradient for a constant thermal conductivity. Lienhard simplifies Equation (2-1) for 1-D, steady-state conduction to:

$$q = -k\frac{\Delta T}{L} \tag{2-2}$$

where L is the half-thickness of the material. The solution for transient conduction adds a rate term. For a 1-D slab, the conduction equation for the thermal gradient through the slab, from Leinhard, is:

$$\frac{\partial^2 T}{\partial x^2} = \frac{1}{\alpha}\frac{\partial T}{\partial t} \tag{2-3}$$

where T is the temperature, x is the distance through the slab, α is the thermal diffusivity, t is the time, and

$$\alpha = \frac{k}{\rho C_p} \tag{2-4}$$

where ρ is the density and C_p is the specific heat capacity. Heisler charts can be used to look up an approximate solution to the conductivity equation (Heisler, 1947). Another method, from (Rasekh, Vaziri, & Poursartip, 2004), can be used to calculate the temperature lag during a temperature ramp:

$$\Delta T_{ss} = -\dot{T}\frac{L^2}{\alpha}\left(0.5 + \frac{1}{Bi}\right) \quad \textbf{(2-5)}$$

where ΔT_{ss} is the steady-state temperature lag at the mid-plane, $\dot{T}$ is the temperature ramp rate, and Bi is the Biot number. Modern technology also allows an exact solution to be obtained using a number of available math or finite element software packages.

The conduction problem is further complicated when multiple objects and materials are used. Perfect contact between two surfaces does not occur due to natural variation in the surface finishes and the contact pressure applied to the objects. At the microscopic level, the material surfaces have peaks and valleys. Contact at the peaks produces good conduction, but gaps in the valleys impede conduction. From Leinhard, the contact resistance from a gap is quantified as:

$$R_c = \frac{\Delta T}{q} \quad \textbf{(2-6)}$$

where ΔT is the temperature difference across the interface.

Multiple layers of materials are required to vacuum-bag a composite, and the layers can build up significant interfacial resistances. Antonucci, et al. (2002) reported localized thermal variations across the cure assembly surface due to deformation of the bagging materials. However, contact resistance is assumed to be negligible or is ignored in current composite thermal modeling literature.

Instead, literature has focused on the conductivity of the composite, and not on that of surrounding materials. The conductivity of the composite depends on the conductivities of the fiber and matrix. Fiber conductivities are difficult to measure, and carbon fibers have different longitudinal (k_{11}) and transverse (k_{22}) thermal conductivities (Johnston, 1997; MIL-HDBK-17-2F, 2002). Longitudinal conductivities can be 3 to 10 times higher than transverse conductivities, Table 2-1. Published thermal conductivity values do not consistently report longitudinal and transverse properties. Toray T300 conductivities, for example, range from 2.5-100.0 W/mK, and only one out of the four sources indicates if the conductivities are in the longitudinal or transverse fiber directions.

Table 2-1: Survey of the range of carbon fiber thermal conductivities from literature and manufacturers

Fiber	K11	k22	Reference
AS	26		(Loos & Springer, 1983)
AS4	7.7	2.4	(Johnston, 1997)
AS4	6.8		(Hexcel Corporation, 2010a)
CN80	320	11	(Schuster, Heider, Sharp, & Glowania, 2009)
IM7	5.4		(Hexcel Corporation, 2010c)
IM10	6.1		(Hexcel Corporation, 2010b)
M35J	39		(Toray Inc., 2010a)
M40J	68.6		(Toray Inc., 2010b)
M46J	84.5		(Toray Inc., 2010c)
M50J	97.9		(Toray Inc., 2010d)
M55J	155.6		(Toray Inc., 2010e)
M60J	151.8		(Toray Inc., 2010f)
P-25	26-36		(Cytec Industries Inc., 2003a)
P-30	62		(Cytec Industries Inc., 2003b)
T300	2.5		(Guo, Du, & Zhang, 2005)
T300	100	11	(Schuster et al., 2009)
T300	10.5		(Toray Inc., 2010h)
T300J	9.3		(Toray Inc., 2005)
T-300	5		(Cytec Industries Inc., 2003c)
T400H	10.5		(Toray Inc., 2005)
T650	14	5	(Cytec Industries Inc., 2003d)
T700	100	11	(Schuster et al., 2009)
T700S	9.4		(Toray Inc., 2010i)
T800H	35.1		(Toray Inc., 2010j)
T1000G	32		(Toray Inc., 2010g)
YS80	320	11	(Schuster et al., 2009)

Matrix conductivities are isotropic, but the resin conductivity can change as the resin cures. A numerical sensitivity analysis of changing resin properties during cure by Twardowski et al. (1993) showed a 40% change in density and specific heat capacity, and an 80% change in thermal conductivity. They declared these changes to be "relatively unimportant", but the published results show that there was excellent agreement only until the cure reaction accelerated. The peak exotherm temperatures in their study varied from nominal temperatures by more than 10.0 °C (Twardowski, Lin, & Geil, 1993). Although they make no distinction regarding what percent of the variation is specifically the result of conductivity, density, or specific heat capacity changes, resin conductivity is a factor if model predictions are to be within the 2.0 °C target.

Because of the anisotropic fiber properties, the composite has different in-plane and through-thickness conductivities. Composite conductivities are also affected by the ratio of fiber to matrix. For in-plane conductivity, the rule-of-mixtures is used:

$$k_{11C} = V_f\, k_{11f} + (1 - V_f)\, k_r \tag{2-7}$$

where V_f is the fiber volume fraction, k_{11f} is the longitudinal conductivity of the fiber, and k_r is the conductivity of the resin (Peters, 1998). Fiber conductivities are higher than resin, so increasing V_f increases the composite conductivity.

The Springer-Tsai relationship is used for calculating through-thickness composite thermal conductivities (Springer & Tsai, 1967). The Springer-Tsai relationship assumes isotropic conductivity in the fibers and a packing arrangement with isolated fibers in a square grid of resin. From a micro-mechanical point of view, the assumption of no fiber contact in the Springer-Tsai relationship is incorrect. Fiber-fiber contact raises the through-thickness conductivity, and higher V_fs increase the frequency of fiber-fiber contact (G. Zhang et al., 2010). Using a graphite-filled composite and percolation theory, G. Zhang et al. (2010) showed that through-thickness conductivity increased from less than 1 W/m K at a V_f of 0.2 to 17 W/m K at a V_f of 0.9. Other recent works have used finite-element models of unit-cells consisting of several fibers in partial contact, surrounded by the matrix (Schuster et al., 2009). The unit-cell result can be more accurate than assuming no fiber contact in a closed-form solution, but it is a time consuming approach. A new unit-cell must be analyzed for every change in fiber architecture, and verification that the composite micro-structure matches the unit-cell geometry is difficult.

2.1.2 Thermochemical Model

Loos and Springer published the first definitive work on cure modeling and the definition of the 'thermochemical model'. A thermochemical model is a mathematical model that outputs the temperature, degree of cure, and resin viscosity of a composite undergoing a thermal cycle; it can also be used to predict development of the composite properties during cure (Ciriscioli, Wang, & Springer, 1992; Loos & Springer, 1983).

The thermoset cure process occurs by one of two polymerization reactions: addition or condensation (Peters, 1998). Addition polymers require a catalyst to start the reaction, and the reaction continues as long as there are free radicals at the ends of polymer chains. Condensation polymers have two or more molecules that react by losing pendant groups which form a by-product and the main molecular back-bones bond together. Both reactions involve creating a 3-

D polymer network as polymer chains are linked to each other with 'crosslinks', Figure 2-2 (Peters, 1998).

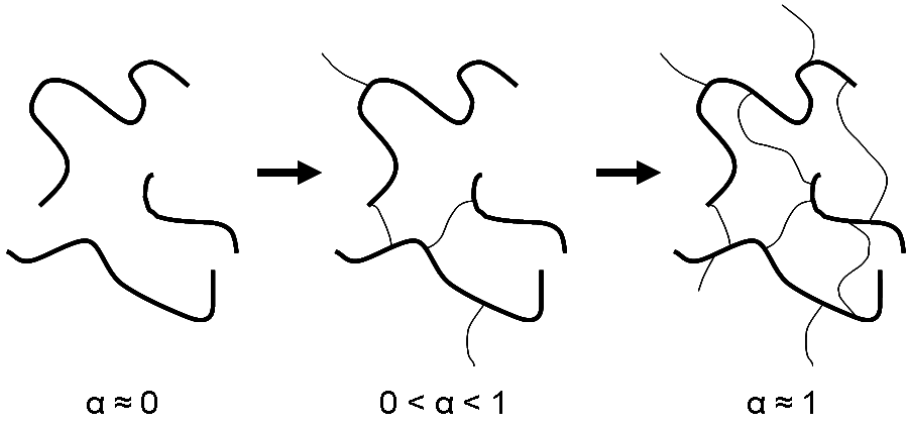

Figure 2-2: Development of crosslinks between polymer chains as cure progresses. α is the non-dimensional term for degree of cure. α is zero when uncured and approaches one when fully cured.

Heat can be used to accelerate the reaction, and both types of cure reactions are exothermic. The progress of the cure is quantified with a degree of cure (DoC) term, α:

$$\alpha = \frac{H(t)}{H_R} \tag{2-8}$$

where $H(t)$ is the total heat generated by time t, and H_R is total amount of heat that is generated from a complete cure reaction (Loos & Springer, 1983). $\alpha = 0$ for uncured resin, and $\alpha = 1$ for fully cured resin; thus, at any point in the cure process, $0 < \alpha < 1$. Nominal resin properties occur at maximum DoC.

Thermochemical models are typically generated from differential scanning calorimetry (DSC) data. DSC compares the thermal response of a material to that of an inert sample. Differences in temperatures and heat flows between the two samples are used to extract material properties such as specific heat capacity, glass transition temperature, phase changes, and heats of reaction (TA Instruments, 2010; Zielenkiewicz, 2008). Standards and guides are readily available for using DSC to create thermochemical models including ASTM standards and the MIL-17 Composite Materials Handbook (ASTM Standard E 2041, 2008; ASTM Standard E 2070, 2008; ASTM Standard E 2160, 2004; ASTM Standard E 698, 2005; MIL-HDBK-17-1F, 2002; MIL-HDBK-17-2F, 2002).

Validation of the DSC generated model is typically conducted against additional DSC results. Using DSC to validate models is problematic, since a DSC sample is of the order of milligrams, but the composite structures that use the models can be hundreds of kilograms. Variability

occurs in the distribution of resin on a sheet of prepreg, and the small samples required for DSC can come from resin-rich or resin-starved areas (D. Dykeman, 2008). Different resin quantities lead to different kinetic responses.

The rate of cure is the response used in traditional thermochemical models, as it is a determining factor for the final DoC (D. Dykeman & Poursartip, 2004). An improperly designed cycle can prevent the resin from ever reaching full cure by reacting too slowly to crosslink sufficiently before vitrification occurs (D. Dykeman & Poursartip, 2004). In thermochemical models, cure rate is a function of DoC and temperature (D. Dykeman & Poursartip, 2004; Loos & Springer, 1983):

$$\frac{d\alpha}{dt} = f(\alpha, T) \tag{2-9}$$

The function $f(\alpha, T)$ is unique to each resin system, and can have as many terms as needed to properly characterize the resin with the desired level of detail. Development and optimization of cure models is beyond the scope of this work. Instead, existing models are tested for validity by comparing simulated to experimental responses.

Since this work is not concerned with the exact model form and coefficients used in the models, process maps are useful illustrations of the thermochemical model behaviors. Process maps are simple diagrams showing DoC vs. temperature curves which are used to study the cure model behavior, (D. Dykeman & Poursartip, 2004). Process maps for the five material models used in this work are presented in Appendix A to show the different responses of each thermochemical model over a range of DoCs, ramp rates, and hold times.

Several authors have used laminates for validation of their DSC generated thermochemical model, including Loos and Springer (1983), Rai and Pitchumani (1997), and Antonucci et al. (2001). Loos and Springer's thermochemical model can be improved further; only 3 of the 14 layers in their experimental cure-assembly were modeled because "the additional components . . . have no direct effect on the model" (Loos & Springer, 1983). Only the composite, tool, and breather were modeled while the metal caul plate and multiple layers of peel ply, release film, and breather were ignored. The other layers may have been significant if, for example, the metal caul plate had a significant thermal mass and drew heat away from the composite during the cycle. It is possible that the heat generation for the model was incorrect, but the model showed good agreement because the error was masked by the effect of the caul plate or other bagging materials.

Rai and Pitchumani (1997), like Loos and Springer, limited the modeled material stack to the composite and tool. Instead of a set-temperature boundary condition, Rai and Pitchumani used an unspecified convective heat transfer coefficient (HTC) for the simulation boundary. Ensuring the HTC is correct is an additional source of uncertainty introduced into their simulation, and their definition of good agreement for model validation was a prediction within 5.0 °C. An accuracy of 5.0 °C is unacceptable in practice since the uncertainty of the model has consumed the laminate's allowable temperature deviation.

Antonucci et al. (2001 and 2002) proposed validating thermochemical models using a method that ignored the surrounding materials and used the thermal response of the laminate to convert the thermal resistance of the surrounding materials into an effective HTC boundary condition. This method reduced the uncertainty of the HTC boundary by quantifying it with experimental data. However, the maximum absolute difference was still large at 8.0 °C between the experimental and simulated results. As with the set-temperature boundary by Loos and Springer (1983), Antonucci's (2002) effective HTC boundary on the laminate surface did not account for heat flow between the laminate and the surrounding objects. The worst agreement occurred during the reaction peak, which was when internal heat generation was highest and when the tool acted as a heat sink to absorb the heat generated. It is possible that the thermochemical model was correct, but the effective HTC did not replicate the thermal mass of the tooling. Reducing the uncertainty of the boundary conditions and the interactions between the materials in the cure assembly is needed to improve model accuracy to within the 2.0 °C target proposed by this author.

2.1.3 Convective Heat Transfer

Convective heat transfer is driven by fluid motion. As fluid flows over a surface, velocity and thermal boundary layers form as a result of friction between the fluid and surface. The velocity boundary layer is a layer of variable fluid velocity that results from the free-stream velocity being reduced to zero velocity on the surface. As the distance from the leading edge of a surface increases, the velocity boundary layer will transition from a laminar to turbulent velocity layer (Lienhard, 2006). Heat transfer is higher in the turbulent region than in the laminar region, and the laminar-to-turbulent transition can be determined by the critical Reynold's number (Advanced Thermal Solutions, 2007). The Reynold's number, *Re*, is the ratio of the inertial to the viscous fluid forces:

$$Re = \frac{\mu_\infty x}{v} \quad \textbf{(2-10)}$$

where μ_∞ is the free-stream fluid velocity, x is the distance from the leading edge, and v is the kinematic viscosity (Lienhard, 2006).

A high *Re* means the inertial forces of the fluid dominate the viscous interaction between the fluid and slab, making it more likely that the laminar boundary layer will detach from the slab surface and produce a turbulent boundary layer. The critical Reynold's number is affected by the stability of the free-stream airflow, the local geometry, and the slab surface finish; $Re > 5.0 \times 10^5$ is the critical Reynold's number for laminar to turbulent transition for a flat slab, but it can be much lower for curved surfaces or unstable airflow (Kutz, 1998; Lienhard, 2006). The airflow encountered in this work can be considered entirely turbulent ($4.0 \times 10^5 < Re < 3.5 \times 10^6$).

The thermal boundary layer results from the temperature difference between the object surface and the surrounding fluid (Lienhard, 2006). The Prandtl number, *Pr*, is used to characterize the thermal boundary layer; it is the ratio of the fluid's kinematic viscosity to its thermal diffusivity, (Lienhard, 2006):

$$Pr = \frac{\nu}{\alpha} \quad \textbf{(2-11)}$$

where v is the kinematic viscosity, and α is the thermal diffusivity of the fluid. If $Pr > 1.0$, the velocity boundary layer is thicker and convective heat transfer dominates (Lienhard, 2006). If $Pr < 1.0$, the thermal boundary layer is thicker and conductive heat transfer dominates (Lienhard, 2006). $Pr \approx 0.7$ for the processing environment in this work.

The convective heat transfer coefficient (HTC) quantifies the rate of heat transfer from the object surface to the fluid through the boundary layers:

$$h = \frac{q}{\Delta T_s} \quad \textbf{(2-12)}$$

where q is the heat flux, and ΔT_s is the temperature difference between the surrounding fluid and the surface (Kutz, 1998). h is orientation and geometry dependant, and two objects in the same environment can have different HTCs. Relations using the Reynold's number and Prandtl number have been developed to capture how HTC is affected by temperature, pressure, geometry, and velocity changes, Table 2-2.

Table 2-2: Heat transfer coefficient correlations.

Configuration	Correlation	Reference
Laminar external flow across a single cylinder	$h = 0.3 + \frac{0.62\,\mathrm{Re}^{1/2}\,\mathrm{Pr}^{1/3}}{\left[1+\left(\frac{0.4}{\mathrm{Pr}^{2/3}}\right)\right]^{1/4}} \cdot \frac{k_{fluid}}{\pi D}$	**Churchill and Bernstein** (Lienhard, 2006)
Turbulent external flow across a single cylinder	$h = \frac{0.037\,\mathrm{Re}^{0.8}\,\mathrm{Pr}}{1+2.443\,\mathrm{Re}^{-0.1}\left(\mathrm{Pr}^{2/3}-1\right)} \cdot \frac{2k_{fluid}}{\pi D}$	(Lienhard, 2006) (Spang, 2008)
Turbulent external flow across a single cylinder	$h = 0.3 + \frac{0.62\,\mathrm{Re}^{1/2}\,\mathrm{Pr}^{1/3}}{\left[1+\left(\frac{0.4}{\mathrm{Pr}^{2/3}}\right)\right]^{1/4}} \cdot \left[1+\left(\frac{\mathrm{Re}}{282000}\right)^{1/2}\right] \frac{k_{fluid}}{\pi D}$	**Churchill and Bernstein** (Lienhard, 2006)
Laminar forced convection across a flat plate	$h = 0.664\sqrt{\mathrm{Re}}\,\sqrt[3]{\mathrm{Pr}} \cdot \frac{k_{fluid}}{L}$	**Pohlhausen** (Spang, 2008)
Turbulent forced convection across a flat plate	$h = \frac{0.037\,\mathrm{Re}^{0.8}\,\mathrm{Pr}}{1+2.443\,\mathrm{Re}^{-0.1}\left(\mathrm{Pr}^{2/3}-1\right)} \cdot \frac{k_{fluid}}{L}$	**Petukhov** (Lienhard, 2006) (Spang, 2008)

HTC should increase with increasing pressure and decreasing temperature, and a simple relationship for fully developed turbulent flows was observed by Johnston et al. (Johnston, Hubert, Vaziri, & Poursartip, 1998):

$$h \propto \left(\frac{P}{T}\right)^{\frac{4}{5}} \tag{2-13}$$

where P is pressure and T is temperature. Pressure thus has a greater influence than temperature on HTC.

Air and nitrogen are the gases used in oven and autoclave environments, and their properties are similar at room and elevated temperatures, Table 2-3. The heat transfer and scaling correlations are therefore applicable to both air and nitrogen environments.

Table 2-3: Thermal and fluid properties of air and nitrogen gas at 20 and 100 °C (Microelectronics Heat Transfer Laboratory, 1998)**.**

	ρ kg/m^3	C_p J/kg K	k W/m K	α m^2/s	ν m^2/s	Pr	Re 1 m/s	Re 5 m/s
20 °C								
Air	1.205	1006	0.026	2.11E-05	1.51E-05	0.716	66200	330900
N_2	1.165	1041	0.025	2.10E-05	1.51E-05	0.717	66400	332000
100 °C								
Air	0.946	1011	0.031	3.27E-05	2.18E-05	0.704	45900	229300
N_2	0.915	1043	0.031	3.23E-05	2.30E-05	0.711	43500	217400

HTC in an oven or autoclave is affected by all of the above influences: a temperature and pressure cycle is required for cure, turbulent airflow patterns alter air velocities inside the autoclave, and the complicated cure assembly geometry cause localized HTC variation. Because of the difficulty in measuring and characterizing the HTC, gross assumptions and approximations have been made in published process modeling works that use a convective heat transfer boundary condition. Except for Antonucci et al. (2002) and Johnston et al. (1998), HTC values were either approximations based on prior experience and/or literature, or they were parametrically derived for optimal agreement, Table 2-4. All of the works used a constant value for the HTC boundary, even though HTC changes with temperature and pressure.

Table 2-4: Table of various autoclave HTCs used as process simulation boundary conditions from literature.

HTC (W/m^2 K)	Source
11.3	(Ciriscioli et al., 1992)
125 and 87	(Bogetti & Gillespie, 1991)
10-170	(Johnston et al., 1998)
100	(Yi, Hilton, & Ahmad, 1997)
30-100	(V. Antonucci, Giordano, Inserraimparato, & Nicolais, 2001)
21.8 and 59.5	(V. Antonucci, Giordano, Imparato, & Nicolais, 2002)
20-200	(Rasekh et al., 2004)
70	(Guo et al., 2005)
70-170	(Shimizu, Kotlik, Arafath, & Poursartip, 2008)
100	(D. Dykeman, 2008)
5.0, 37.636 and 54.075	(J. Zhang, Xu, & Huang, 2010)

The most recent work in Table 2-4, Zhang, Xu, Huang (2010), shows that a gap remains in the understanding of how numerical and experimental HTC boundary conditions are related in

composite process modeling. The HTC for simulation *verification* was over-defined, especially when compared to the HTC for model *validation*, which was an approximation of the experimental conditions based on previous experience. The HTC was within 0.001 W/m^2 K for simulation verification, but HTC was rounded to an arbitrary integer, 5.0 W/m^2 K, for model validation. Their assumption made for the validation HTC was that there will be some, but unknown, reduction in convective heat transfer by the tooling materials between the composite and air. The uncertainty of the HTC boundaries in the process simulation could have been significantly reduced by measuring the HTCs.

2.1.4 Radiation Heat Transfer

Radiation heat transfer is generally ignored in composites cure models. Certain specialized applications use radiation heat transfer to cure composites, but, in most autoclave and oven cures, radiation effects are small compared to convective effects (Salagnac, Dutournié, & Glouannec, 2004). Since the temperature difference between the autoclave and the cure assembly is small, and the cure assembly is surrounded by the autoclave walls, radiation in the autoclave can be approximated by a radiation heat transfer coefficient (Lienhard, 2006):

$$\text{If} \quad \frac{\left(\frac{\Delta T}{T_m}\right)^2}{4} << 1 \qquad \textbf{(2-14)}$$

$$T_m = \frac{\left(T_A + T_C\right)}{2}$$

$$h_{rad} = 4\sigma T_m^3 \varepsilon_A$$

where T_A is the autoclave temperature, T_C is the cure assembly surface temperature, σ is the Stephan-Boltzmann constant, and ε_A is the emissivity of the autoclave wall (Lienhard, 2006). h_{rad} = 11.0 W/m^{2}K for a high estimate of an autoclave with steel walls ($\varepsilon_A \approx 0.50$), a thermal cycle with a hold temperature of 475.0 K, and a 30.0 K lag in the cure assembly. Thus it is acceptable to include radiation effects within the HTC term for this work; the radiation HTC is 3-10 times smaller than the convective HTC range of the UBC autoclave.

2.2 Autoclave Characterization

Characterization of the equipment used for manufacturing is necessary if the efficiency of the manufacturing process and the accuracy of the process model are to be maximized. For thermal modeling of composites, the airflow patterns and HTCs in the autoclave are the most important equipment parameters. Airflow affects the HTC, HTC affects the heating of the cure assembly,

and the boundaries of the process model. Airflow can be characterized with anemometers, computational fluid dynamics (CFD), visual monitoring, and HTC distributions.

2.2.1 Airflow Characterization

Anemometers are designed to measure air velocity and/or direction, but they have minimal value in autoclaves because of the highly turbulent environment. Ghariban (1992) used a hot-wire anemometer to measure air velocities in an autoclave, and showed 50% variation from the mean air velocity due to turbulence. The study also showed that mean velocities in their autoclave varied from 1.0 to 7.0 m/s at different locations, and a change in the local HTC corresponding to the velocity variation was experimentally measured. Ghariban's (1992) work showed that the assumption of constant airflow and heat transfer over a cure assembly is not representative of actual processing conditions.

CFD is the only offline method to characterize the airflow in the autoclave, but the simulation results should still be validated experimentally. CFD is computationally intensive, expensive, and a CFD model will ignore the wiring, piping, welds, and mechanical limitations of the autoclave components in order to reduce the complexity of the solution. For example, Telikicherla et al. (1994) added a convective heat transfer boundary to the Loos and Springer (1983) model by incorporating a CFD fluid flow simulation over the cure assembly. For simplicity, the walls of the autoclave model were flat, and the airflow was highly oriented and interacted only with the cure assembly. At the time (1994), eight hours of supercomputer time were required for the solution, and, although modern computing technology has advanced significantly, CFD simulation is still time-consuming. CFD has limitations, but it is the only method available to generate a detailed map of airflow magnitudes and orientations without running the equipment.

Simple wind-tunnel visualization techniques could be used to augment CFD analysis for airflow characterization. Smoke streams, specialized paints, or tufts are used to show airflow paths in the highly oriented and laminar flow of wind-tunnels (Merzkirch, 1987). Visual techniques have not been previously used in autoclaves because the wind-tunnel visualization techniques were not designed for the poorly oriented and turbulent airflow in the autoclave environment. Also, a method has not been developed to visually monitor the results through the autoclave shell.

Local HTC measurements can be used for airflow mapping. As noted, velocity changes measured by Ghariban (1992) resulted in local HTC variations by a factor of three. Johnston et al. (1998) also showed variation in local HTCs at different locations in a single autoclave.

Correlations to the airflow can be made, since areas with high HTC values have higher velocity airflow, and areas with low HTC values have lower velocity airflow.

2.2.2 Heat Transfer Coefficient Measurement

For comparing autoclave capabilities, HTC is a better benchmark than either heating or cooling rates, or maximum temperatures and pressures, due to the sensitivity of the thermal history to HTC. When process modeling is used, HTC measurements ensure that the model boundary is representative of the specific forced convection environment to be used for processing. Simple techniques can be used to measure local HTCs from temperature data, further reducing the uncertainty associated with the processing equipment and environment.

Calorimeters are used to back-calculate HTCs from temperature data. The thermal response of the calorimeter is used to determine the amount of heat energy from the environment needed to cause the response of the calorimeter. Calorimeters of various configurations have been developed specifically to measure HTCs in autoclaves including heated metal plates (Ghariban, Lou, & Haji-Sheikh, 1992; Pursley, 1987), steel plates (Johnston, 1997), and composite parts (Shimizu et al., 2008).

The simplest calorimeter is a lumped-mass calorimeter. Back-calculating the HTC from the temperature data of a lumped-mass can be done with a simple, closed-form solution from (Lienhard, 2006) and (Shimizu et al., 2008):

$$h = \frac{\rho C_p V \Delta T}{A \Delta T_s \Delta t} \tag{2-15}$$

where ρ is the density of the calorimeter material, C_p is the specific heat of the calorimeter material, V is the volume of the calorimeter, A is the area of the calorimeter exposed to the convective heat transfer, and ΔT is the change in calorimeter temperature over the time interval Δt.

An object that is not a lumped-mass will develop a through-thickness temperature gradient when heated. The gradient that develops is used to back-calculate the HTC, and, because the profile is quadratic, the top and bottom HTCs are separately back-calculated for a 1-D problem (Shimizu et al., 2008). Due to the quadratic profile, three or more discrete measurement points in a calorimeter under 1-D heat flow are needed for the back-calculation of HTCs:

$$h = \frac{\sum_{i=1}^{n} \rho C_p L \Delta T_i \Delta \zeta_i}{\Delta T_s \Delta t} \quad \textbf{(2-16)}$$

where n is the number of measurement points through the thickness, L is the half-thickness of the calorimeter, and ΔT_i is the change in temperature at the measurement point, and $\Delta \zeta_i$ is the through-thickness distance between measurement points. ζ is a non-dimensional thickness coordinate where ζ = -1.0 at the bottom surface, ζ = 0 at the adiabatic line, and ζ = 1.0 at the top surface.

Autoclaves and ovens are already equipped for temperature measurement, so calorimetry allows HTCs to be measured on unmodified equipment using the simple, closed-form calculations shown in Equations (2-15) and (2-16). The measured HTCs can then be used as equipment performance benchmarks, to ensure optimum heat transfer to a curing part, or as process model boundary conditions.

2.3 Summary

Current composite thermal modeling validation methods can be improved. No standard methods for validation of thermal models are currently available, and the uncertainty of the thermal simulation of the cure assembly can be reduced by validating the sub-components before integrating them into a complete thermal simulation. The components that should be validated are the conductive heat transfer, thermochemical, and convective heat transfer sub-models.

The conductive heat transfer model can be improved with greater understanding of the fiber conductivities and contact resistances between the cure assembly components. Fiber conductivities are difficult to measure, are anisotropic, and the literature varies significantly in the published fiber conductivity values. Validating the conductive model against experimental data from a laminate, instead of from the individual fiber and matrix data, can ensure that the model is accurate in the situation for which it was designed.

The thermochemical model should be validated against experimental laminate data and not against DSC data. There is a significant difference in the thermal cycles for a DSC sample and a laminate. The process simulation is ultimately concerned with full-size structures, and the model should be validated against the response of a laminate. Experimental and model agreement in earlier works can be improved, and the temperature difference that is considered acceptable agreement should be reduced to 2.0 °C so that the uncertainty of the model is less than half of the composite's thermal processing window.

Users of convective heat transfer sub-models have often relied on approximations instead of experimental data for the boundary conditions. Collecting experimental data by measuring the heat transfer coefficients reduces the uncertainty of the simulation boundaries and processing conditions. The measured HTCs can also be used to understand the capabilities and limitations of an individual piece of equipment. Characterization of the equipment used for processing ensures that the process simulation is representative of actual conditions experienced by a part during cure.

3 1-D Thermal Test Calibration and Validation

In this chapter, the 1-D thermal test methodology is calibrated and validated. The ability of a TC to measure surface temperatures is tested, and the material properties of the rubber and vacuum-bagging consumables are measured and validated.

3.1 Surface Temperature Measurement

Surface temperatures can be used as simulation boundary conditions, and a surface thermocouple must accurately measure the actual surface temperature. Surface temperature measurements are influenced by both the surrounding air, and by the thermal mass and thermal resistance of the material used to affix the thermocouple to the surface. Three solutions used by thermocouple manufacturers are:

- covering the wire with a thermal insulator (Omega, 2010b)
- covering the wire with a thermal conductor covered by a thermal insulator (Omega, 2010c)
- flattening the TC tips to a thin leaf and bonding to the surface (Omega, 2010a)

Using a thermal insulator isolates the wire from the air temperature, but the insulating material is thermally massive compared to the TC tip, and induces thermal lag by heating and cooling more slowly than the surface. Thin leaf TCs require a cement to bond to the surface, and the cement can interfere with the temperature measurement.

3.1.1 Methods

Patches of high temperature polyimide tape, acting as an insulator, and aluminum foil, acting as a conductor, were used in various configurations over a surface TC tip, Table 3-1 and Figure 3-1. Discs of foil were cut out and firmly pressed over the TC tip. A ring of polyimide tape was placed over the circumference of the foil to attach the foil to the surface.

Table 3-1: Insulator and conductor combinations used over surface TC

	Tape Diameter	Tape Layers	Foil Diameter	Foil Layers	Wire Gauge
A	-	-	-	-	40
B	-	-	-	-	24
C	-	-	24	2	40
D	-	-	24	2	24
E	-	-	17	4	40
F	-	-	17	4	24
G	15	1	10	3	40
H	15	1	10	3	24

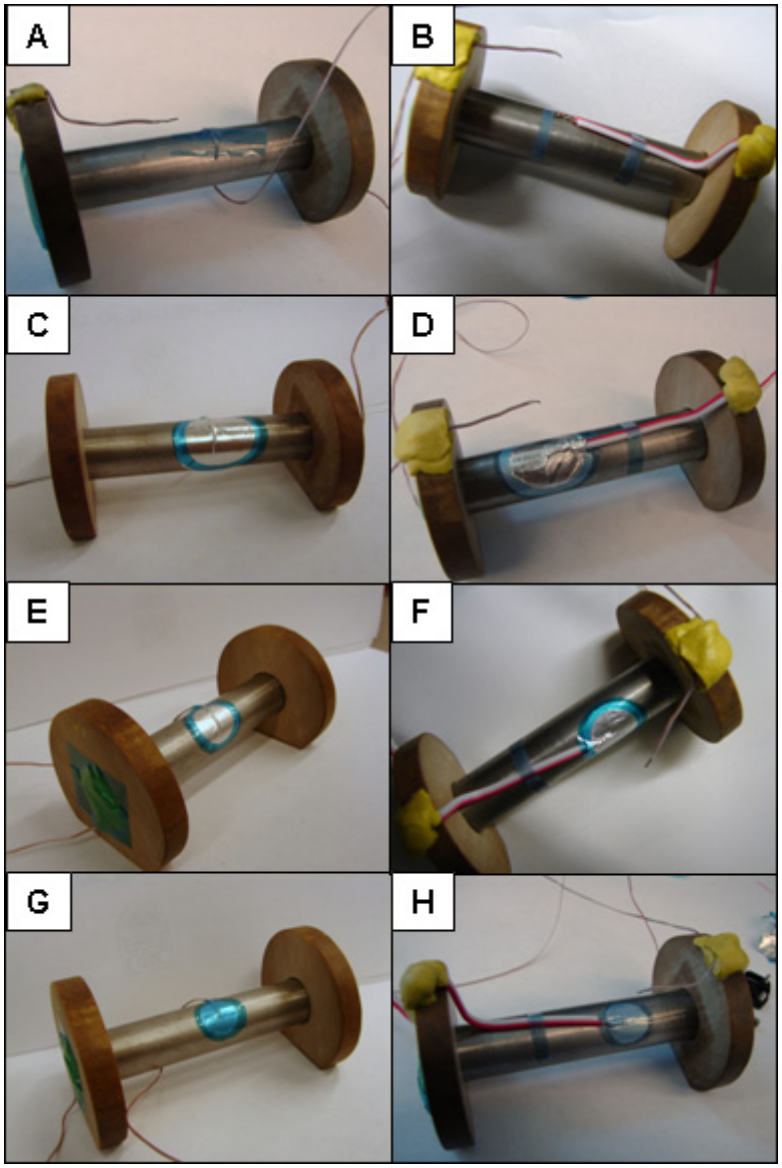

Figure 3-1: Polyimide tape, aluminum foil, and wire combinations used to test surface temperature measurement configurations on a lumped-mass steel rod.

A steel rod had holes drilled along the axis of the rod and a thermocouple inserted into each hole, Figure 3-2. The ends of the steel rod were mounted into non-conductive supports and insulated

with sealant tape. J-type thermocouples were used to measure the surface and interior temperatures of the rod. The surface and interior temperatures should be identical since the rod behaved as a lumped-mass (Bi = 0.04).

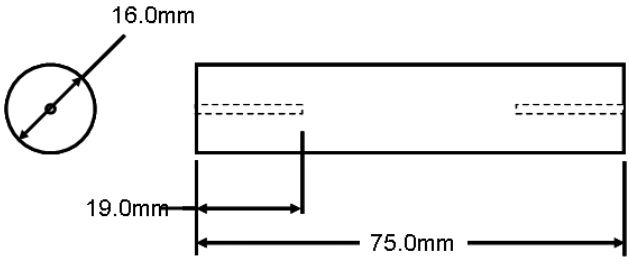

Figure 3-2: Dimensions of lumped-mass steel rod.

The rod was placed into an oven preheated to 150.0 °C, and the temperatures of the TC under the patch and the TC inside the steel rod were recorded until the steel rod reached equilibrium with the oven temperature. The rod was then removed from the oven and naturally cooled to room temperature. The same rod and internal thermocouples were used for every test.

3.1.2 Results and Discussion

ΔT for each configuration was calculated by subtracting the interior temperature from the surface temperature:

$$\Delta T = T_{surface} - T_{interior} \tag{3-1}$$

A positive ΔT indicated the surface temperature was over-reported because the surface led the interior measurement. ΔT, Surface Temperature, Interior Temperature, and Air Temperature were plotted for each configuration.

Configurations A and B, the bare TCs, were heavily influenced by the air temperature. The hot air around the exposed TC increased the measured surface temperature by greater than 20.0 °C, Figure 3-3 and Figure 3-4. Bare TCs are therefore not acceptable for surface temperature measurements.

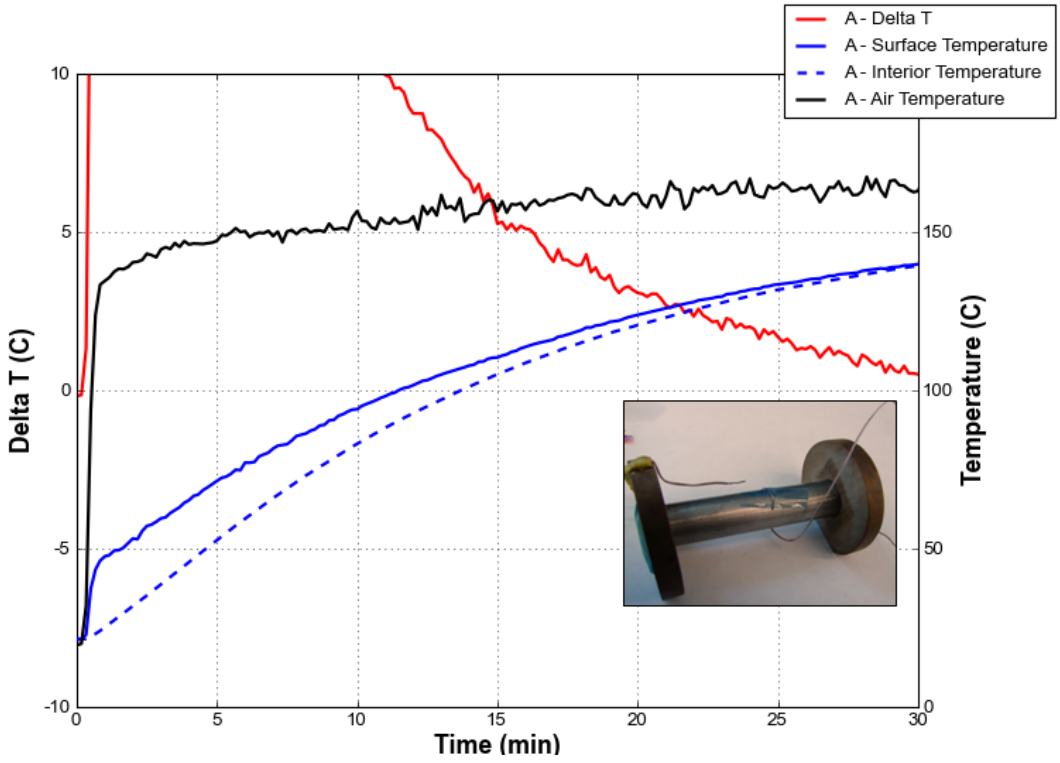

Figure 3-3: ΔT, surface, interior, and air temperatures for configuration A. Air temperature significantly affected the measured surface temperature. (Cool down data not available)

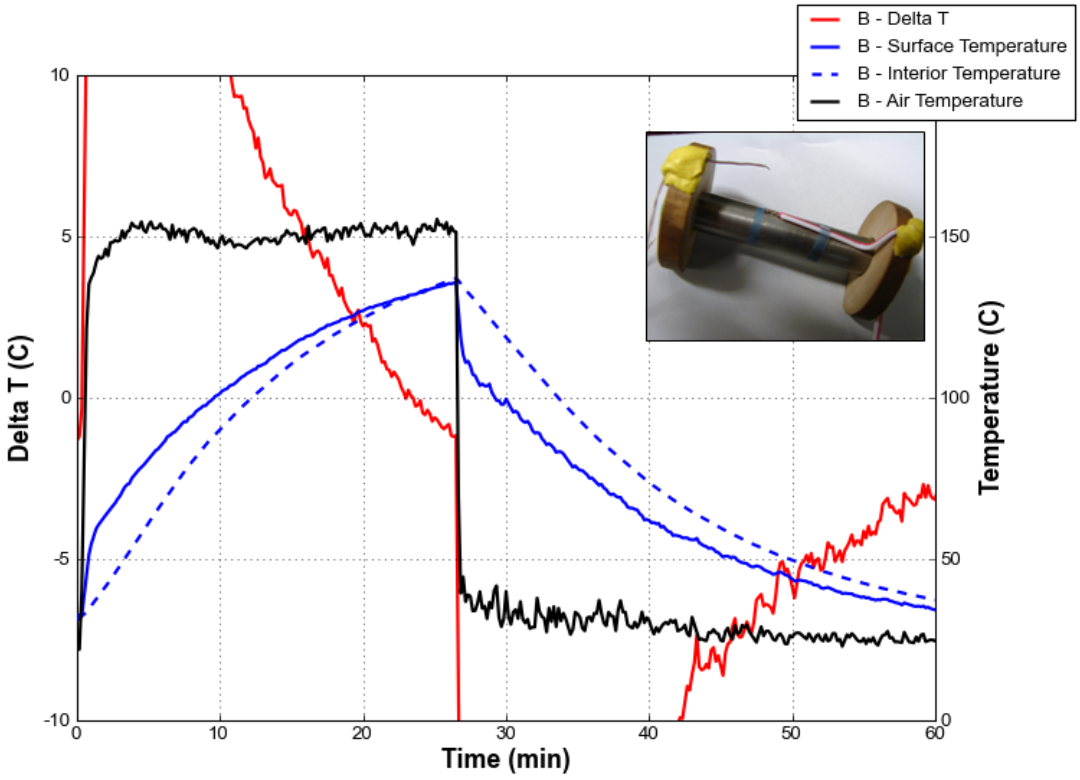

Figure 3-4: ΔT, surface, interior, and air temperatures for configuration B. Air temperature significantly affected the measured surface temperature.

Configurations C showed good agreement between surface and interior temperatures, Figure 3-5. The rapid response of the patch limited the initial error during the temperature changes to less than 2.0 °C. Also, a constant ΔT less than 1.0 °C was achieved because the thin wire of C allowed for a uniform seal between the foil and wire. Configuration D had initial errors greater than 6.0 °C, never reached a constant ΔT, and went from leading to lagging at 12 minutes and 105 °C, then returned to leading again for the duration of the cool down. The thicker wire of D increased the uncertainty of how well the foil patch conformed to the surface, and prevented the offset between surface and interior temperatures from reaching a steady-state ΔT.

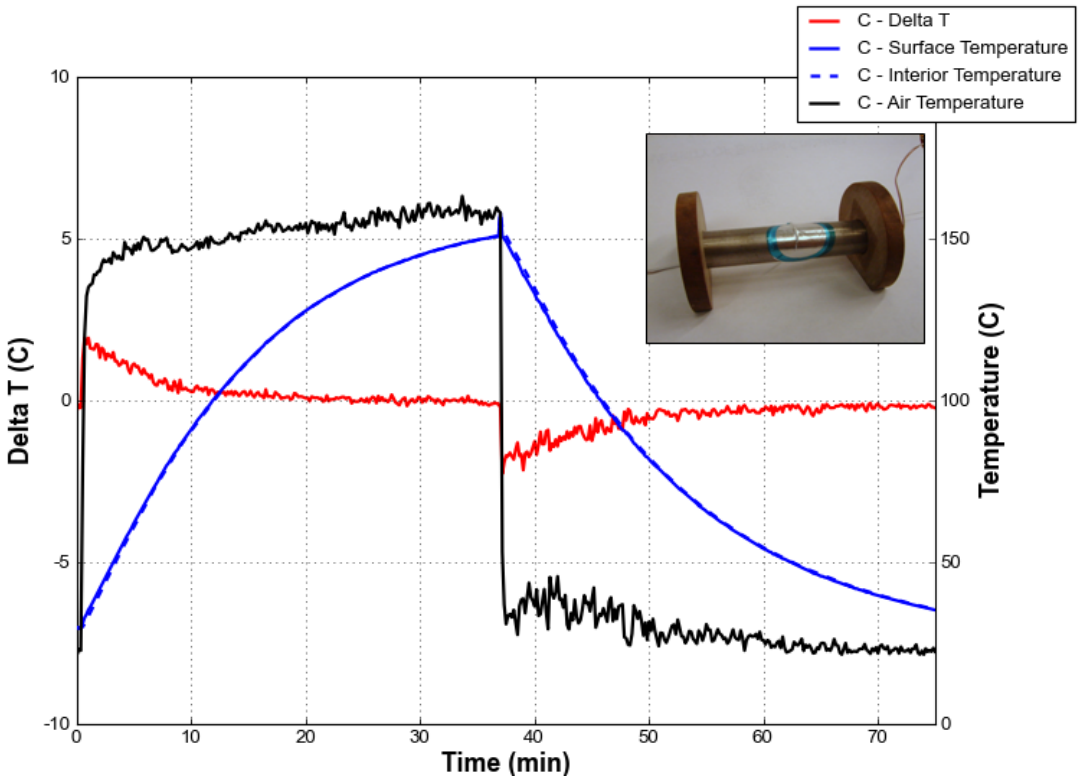

Figure 3-5: ΔT, surface, interior, and air temperatures for configuration C. Conductive layer gives excellent agreement throughout cycle.

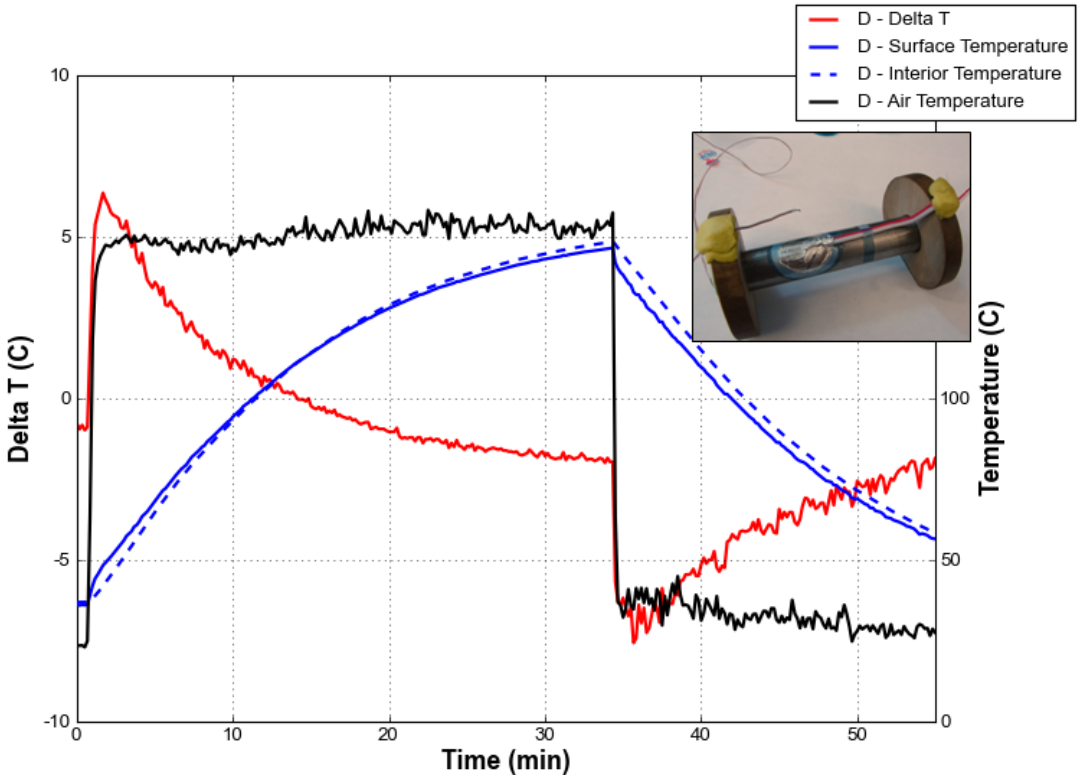

Figure 3-6: ΔT, surface, interior, and air temperatures for configuration D. Measured surface temperature does not reach steady-state.

Changing to a smaller diameter foil with more layers gave results identical to C and D. E had an initial error less than 2.0 °C and reached a constant ΔT less than 1.0 °C, Figure 3-7. F had a large initial error of 7.0 °C, and did not reach a constant ΔT, Figure 3-8. As with D, the increased thickness of the wire of F made it more difficult to get the foil layer to completely conform to the surface and eliminate air pockets.

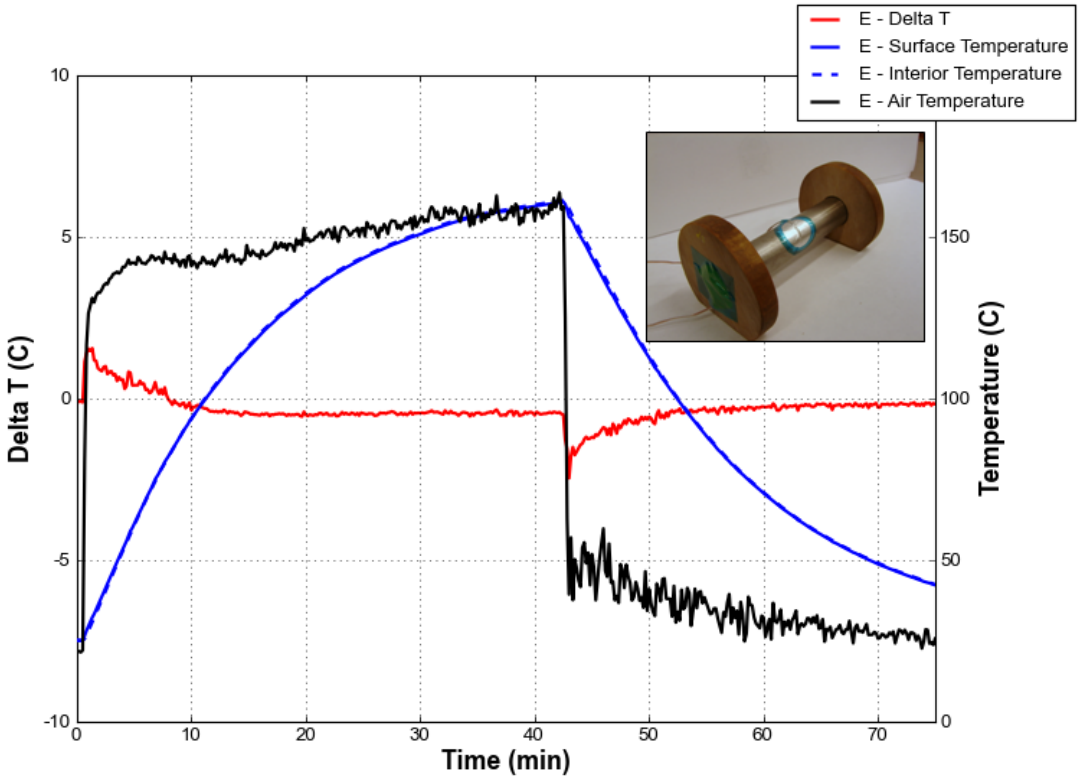

Figure 3-7: ΔT, surface, interior, and air temperatures for configuration E. Alternate foil configuration still gives excellent agreement like that of configuration C.

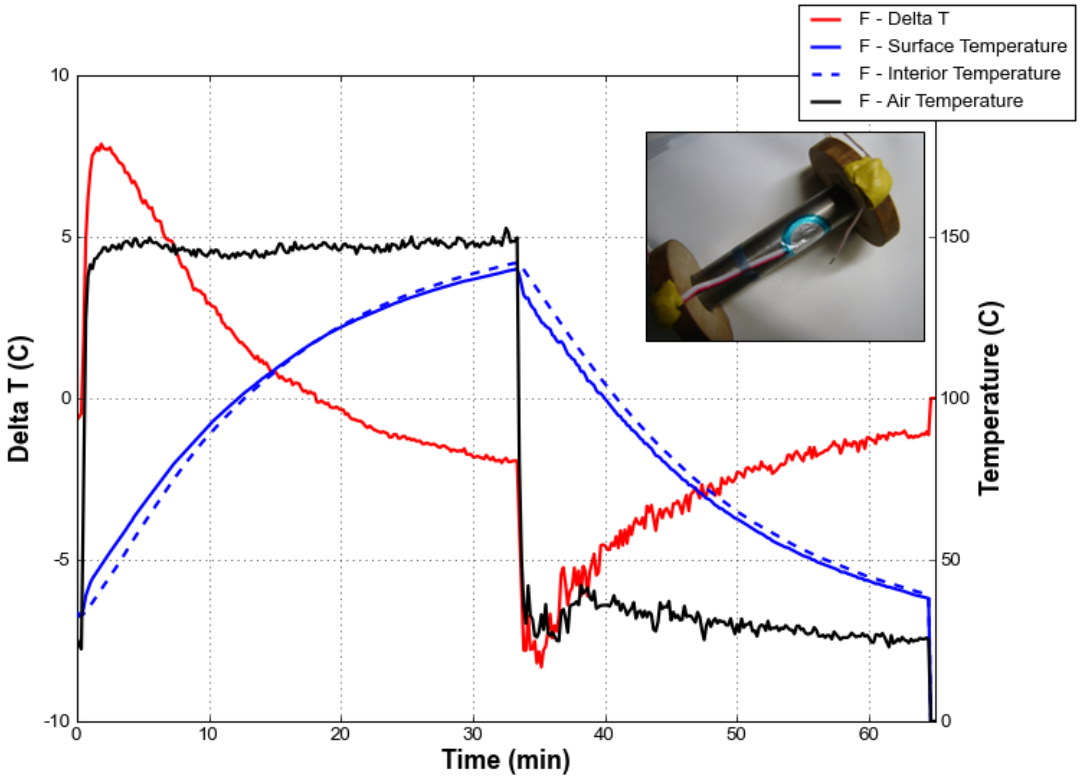

Figure 3-8: ΔT, surface, interior, and air temperatures for configuration F.

Configuration G was the only configuration with thin wiring that did not reach a steady-state ΔT, Figure 3-9. The conductive foil bridged over the TC and created an air pocket. The only difference between G and the other thin-wire configurations, C and E, was complete coverage of the foil by the tape. The tape was not as malleable as the foil, so the tape pulled the foil away and introduced a local air pocket around the TC. H was identical to G, except for the thickness of the wire, and it also did not reach steady-state, Figure 3-10.

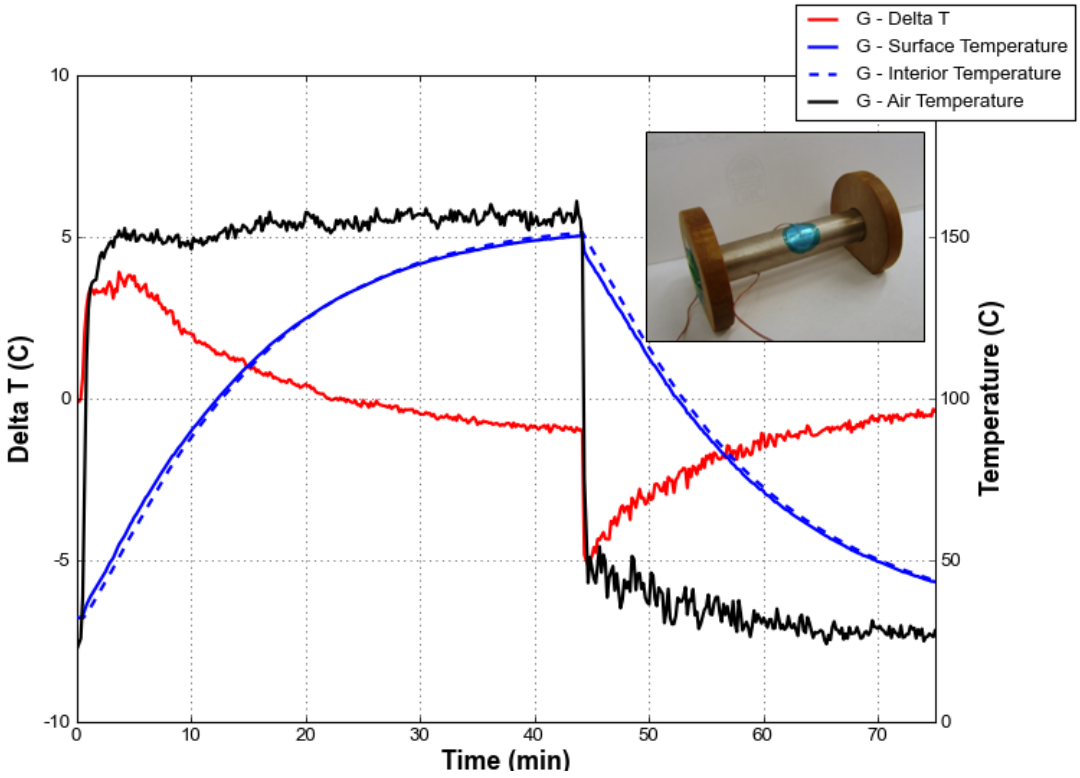

Figure 3-9: ΔT, surface, interior, and air temperatures for configuration G. G was the only configuration with thin wiring that did not reach a steady-state ΔT.

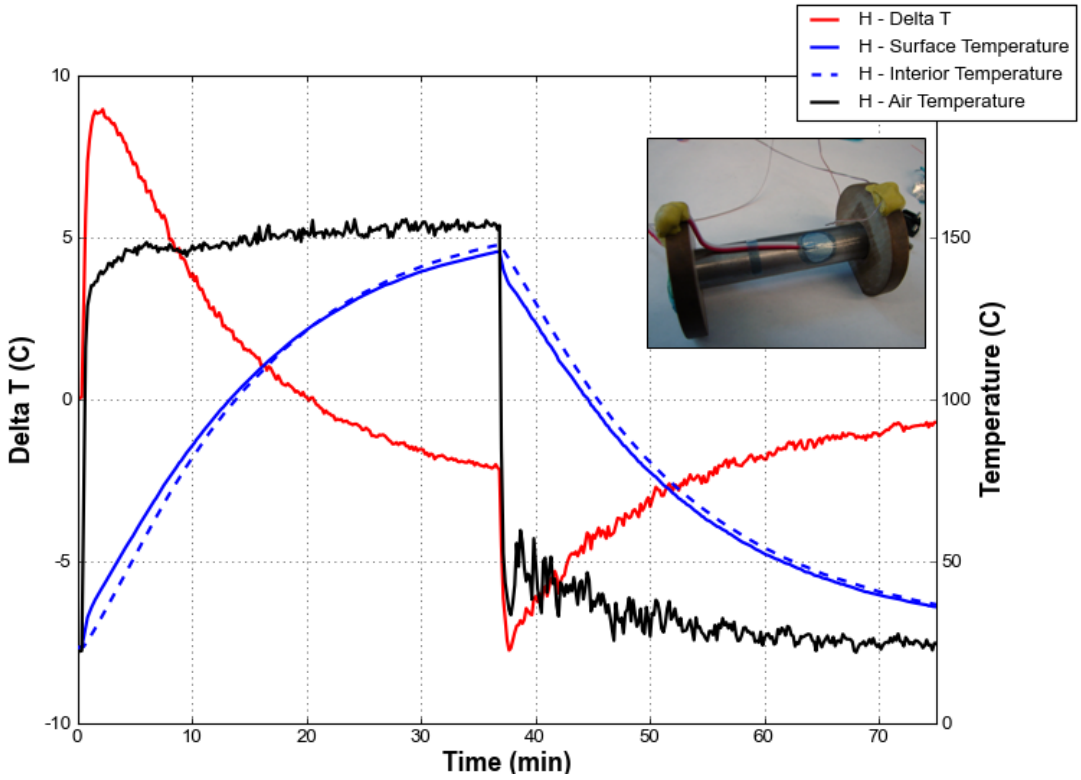

Figure 3-10: ΔT, surface, interior, and air temperatures for configuration H.

In summary, configuration C was the best design. Thin wiring covered by two layers of 24mm diameter foil discs had an initial error during rapid temperature changes that was less than 2.0 °C, and then reached a steady-state ΔT that was within 1.0 °C of the rod's interior temperature. Eliminating gaps between the conductive layer, the TC, and the surface was critical so that stagnant air inside gaps did not affect the measurement The thin, conductive layer isolated the TC from the air temperature while still transferring the heat of the surface to the TC tip.

3.2 1-D Test Validation

3.2.1 Methods

A stack of two rubber bricks, insulated such that heat transfer was 1-D, was used to isolate the conductive response of a material between the bricks. A predictable thermal gradient developed through the thickness of the bricks because the thermal properties of the rubber were known. The gradient was used to verify that the response of the system was not affected by experimental errors and modeled boundary conditions were correctly applied.

Four bricks were cast from Shin-Etsu KE1204 RTV silicone rubber following the procedure in Appendix A. The bricks were grouped into two permanent pairs for the duration of testing. Each brick was 100.0 mm x 100.0 mm x 16.0 mm. TCs were embedded through the thickness at

3.0 mm intervals starting from the bottom of the brick, Figure 3-11. The thermal properties of the rubber are from DSC data, data from this work, and from the Shin-Etsu data sheet, Table 3-2 (Shin-Etsu Chemical Co., 2004).

Table 3-2: Thermal properties of Shin-Etsu KE1204 RTV rubber

Density [1] (kg/m^3)	Specific Heat[2] (J/kg K)	Linear Specific Heat Temperature Dependence[2] (J/kg K)/K	Conductivity[3] (W/m K)	Diffusivity[3] (m^2/s)
1540	1000	3.5	0.53	3.44E-07

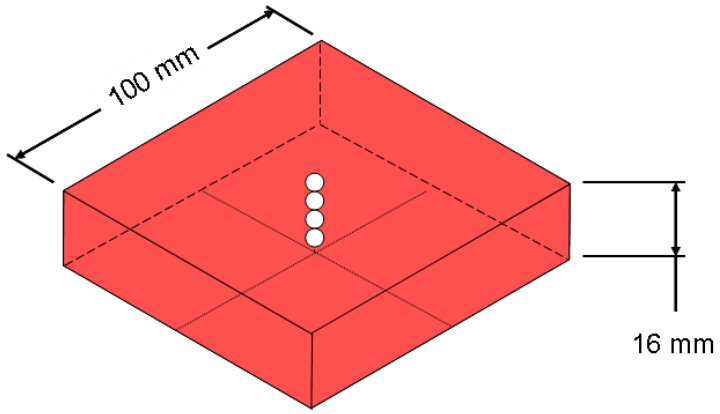

Figure 3-11: Dimensions and thermocouple locations of a rubber brick

Simulation was performed using RAVEN (Convergent Manufacturing Technologies Inc., 2010). RAVEN is a front-end and analysis package using the COMPRO engine, which was developed and is supported by The University of British Columbia. COMPRO is a modular 2-D finite-element solver with thermochemical, stress, and flow sub-models (Hubert, Johnston, Vaziri, & Poursartip, 1995). COMPRO works at the 'local-discretization' level, meaning the model is a cross-section of a composite or composite cure-assembly and not a micro-mechanical or large-scale global model (Hubert et al., 1995). A complete description of the COMPRO engine can be found in Johnston (1997).

The simulation was a 1-D model of the brick/material/brick stack that used the measured thicknesses of the materials. Set-temperature boundary conditions, from experimental thermocouple data, were applied to the top surface of the top brick and bottom surface of the bottom brick.

[1] Shin-Etsu data sheet
[2] DSC data (Appendix C)
[3] Experimental data from this work

3.2.2 Results and Discussion

3.2.2.1 KE1204 Model

To calibrate the inert response of the system, and validate the KE1204 thermal model, two instrumented rubber bricks were stacked with a thermocouple placed at the interface of the bricks, Figure 3-12. The stack was tested following the procedures in Appendix D, and the autoclave cycle was:

- heat at 1.0 °C/minute to 180.0 °C
- hold for 150 minutes
- cool at 5.0 °C/minute to 20.0 °C

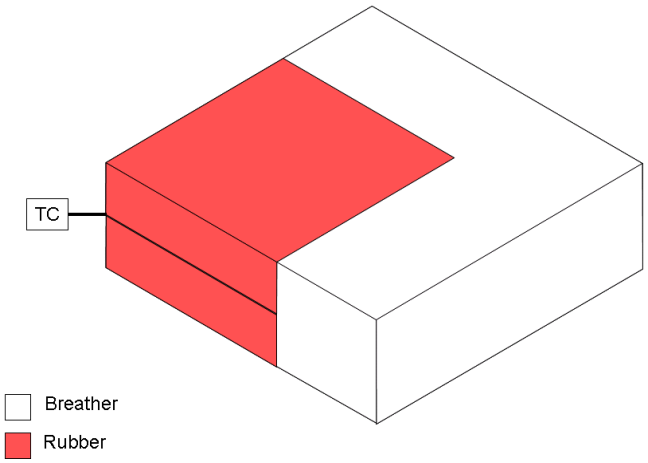

Figure 3-12: Section view showing material stack for validating the material model properties of the rubber. The TC is located in the center of the stack at the interface between the two bricks.

Both pairs of bricks had excellent agreement between the 1-D simulation and the experimental results. Only results for Pair 1 are discussed as the results were identical to Pair 2. The curvature of the through-thickness profiles showed the thermal conductivity was correct, Figure 3-13. The time vs. temperature profile showed the thermal mass (ρC_p) was correctly modeled because the lead and lag of the simulation matched the experiment Figure 3-14.

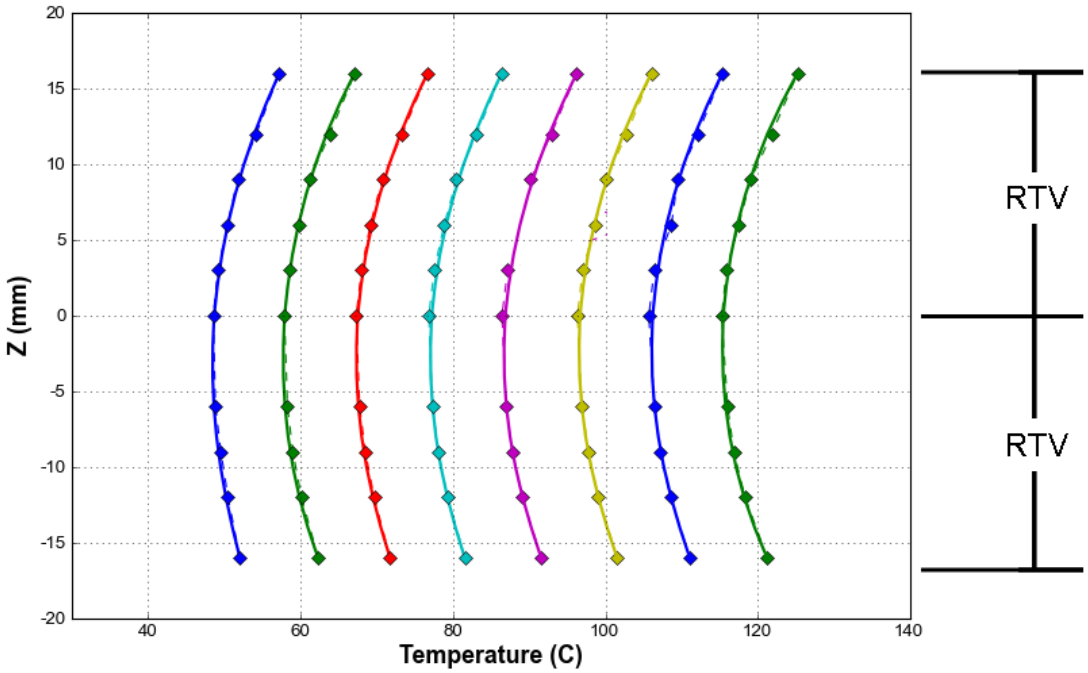

Figure 3-13: Experimental (diamond markers with dashed lines) and simulated (solid lines) through-thickness profile for Pair 1.

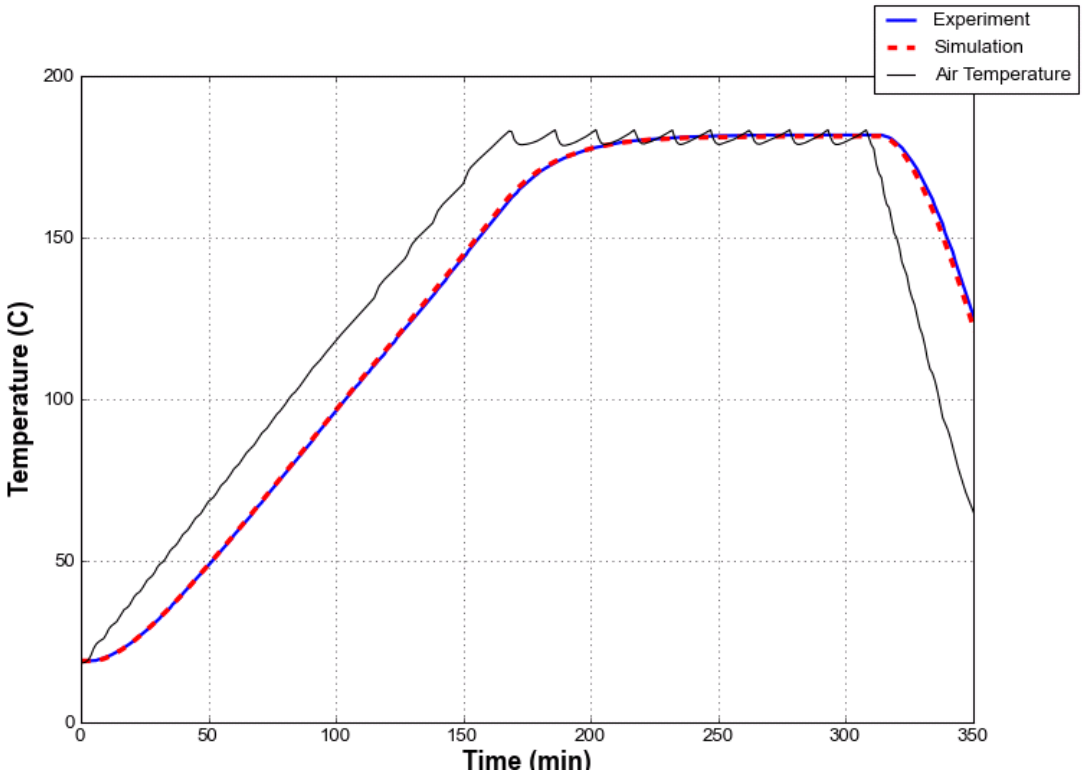

Figure 3-14: Time vs. temperature for the interface of Pair 1.

The top brick in Pair 1 had two additional groups of through-thickness TCs to measure in-plane gradients, Figure 3-15. At 130 minutes into the cycle, the largest measured in-plane gradient during the steady-state ramp was 2.2 °C, Table 3-3. 2.2 °C was close to the measurement error

of the TC, and the in-plane gradients were much smaller than the through-thickness gradient. The gradients confirmed the 1-D heat transfer in the test apparatus.

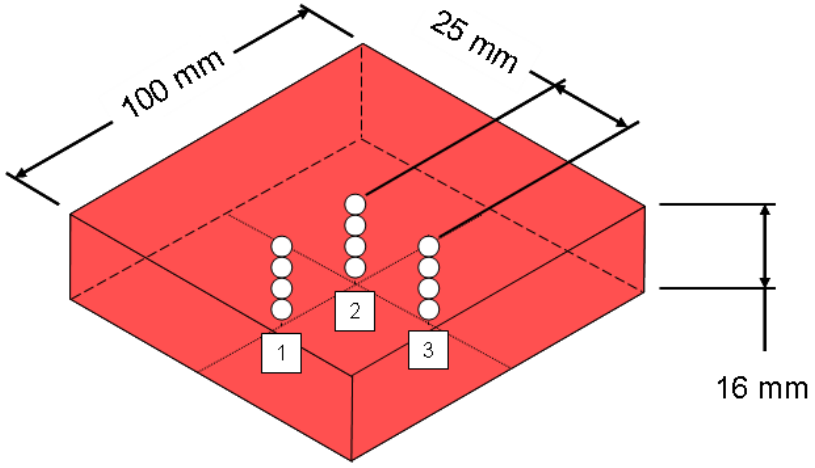

Figure 3-15: Locations of the additional TC groups in zones 1 and 3 in the top brick of Pair 1.

Table 3-3: Largest steady-state gradients in the top brick of Pair 1 at 130 minutes. Note that the through-thickness gradient was much larger than any of the in-plane gradients.

Location	ΔT °C
12 mm	2.2
9 mm	0.1
6 mm	0.2
Through-Thickness	8.4

The uncertainty in using the bricks for additional experiments and simulations was reduced by:

- Validating the thermal properties (conductivity, density, and specific heat) of the material model.
- Validating the use of a set-temperature boundary at the surface of the brick.
- Confirming that breather cloth was effective as insulation. The low conductivity prevented 2-D heat flow, and the low thermal mass did not remove significant amounts of heat from the material stack.

Consequently, a 1-D approximation of the experimental heat transfer was accurate.

3.2.2.2 Aged KE1204 Model

Both pairs of bricks underwent 24 thermal cycles while completing the series of conductive and thermochemical validation tests for this work. To verify that the rubber properties did not

change, the test from Section 3.2.2.1 was repeated on the used bricks. The only changes over time were the failures of several through-thickness TCs, Figure 3-16 and Figure 3-18. Three through-thickness TCs failed in Pair 1, shown by the gaps in the experimental profiles. Other TCs, such as the TC at -12.0 mm, lagged because handling caused imperfect rubber to TC contact when the TC was pulled away from its original position. Lag was induced because the conductivity of air is lower than the rubber. Like the through-thickness profiles, the time vs. temperature profiles for the interface had good agreement for the duration of the cycle, Figure 3-17. Pair 2 also lost three TCs, but at different locations. The remaining TCs in Pair 2 did not show air gap induced lag. The durability of the TC embedment cannot be guaranteed, but the rubber properties did not change with time or temperature exposure.

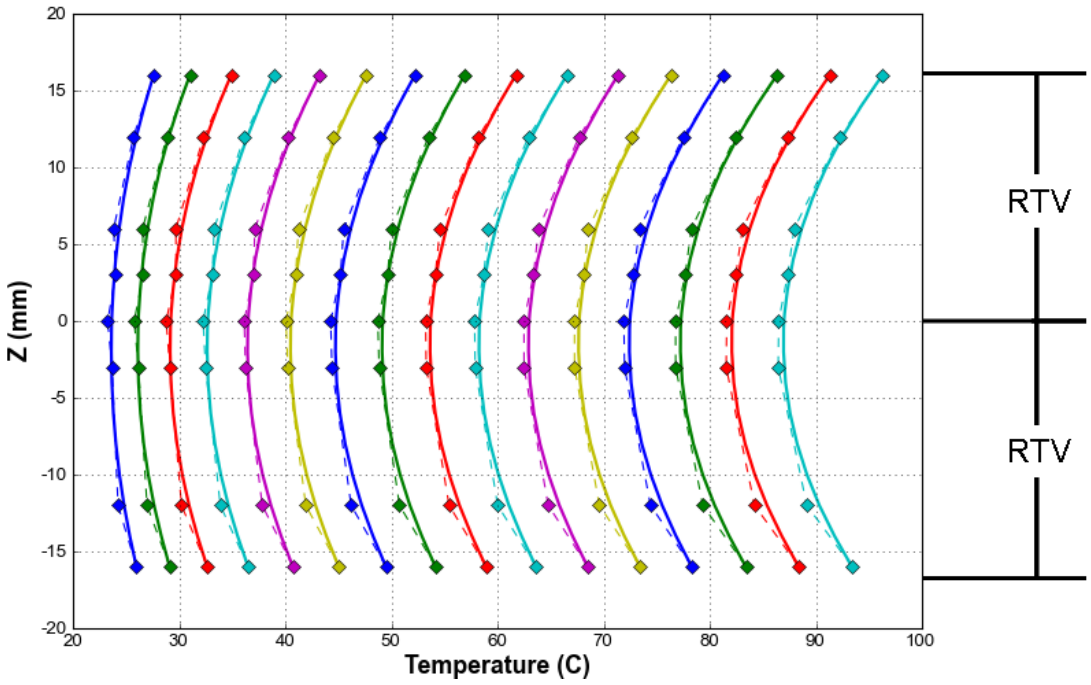

Figure 3-16: Experimental (diamond markers with dashed lines) and simulated (solid lines) through-thickness profiles for Pair 1 at 15 minute intervals.

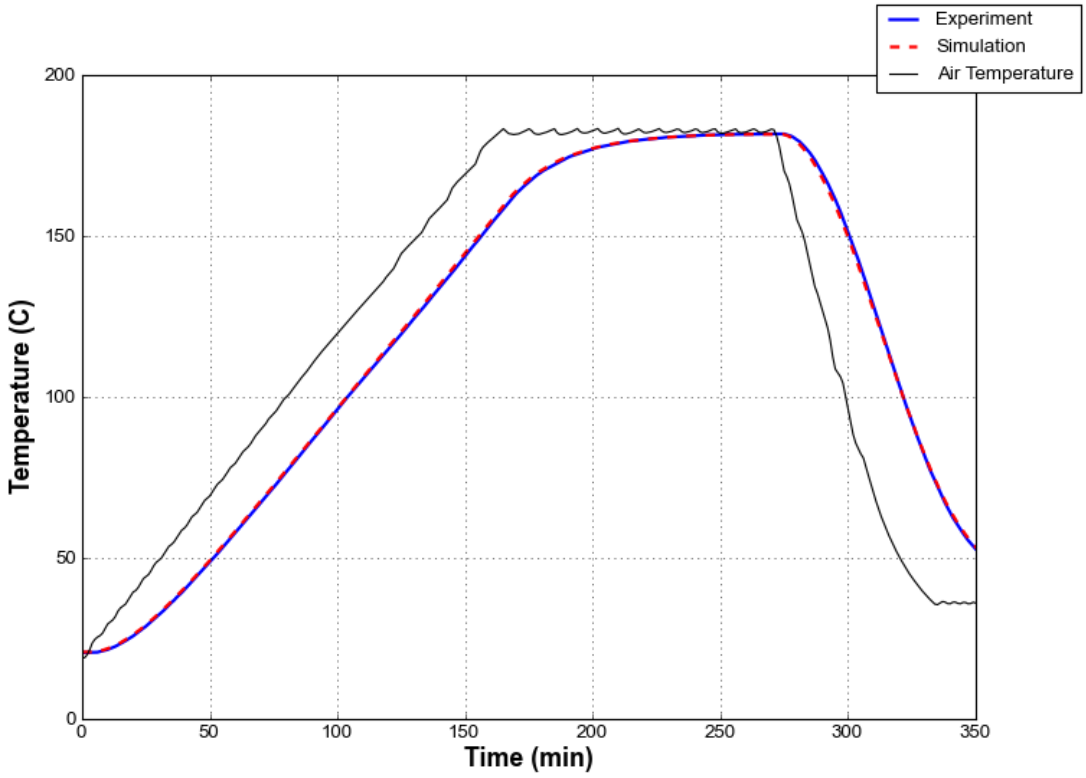

Figure 3-17: Experimental and simulated time vs. temperature profiles for the used brick Pair 1.

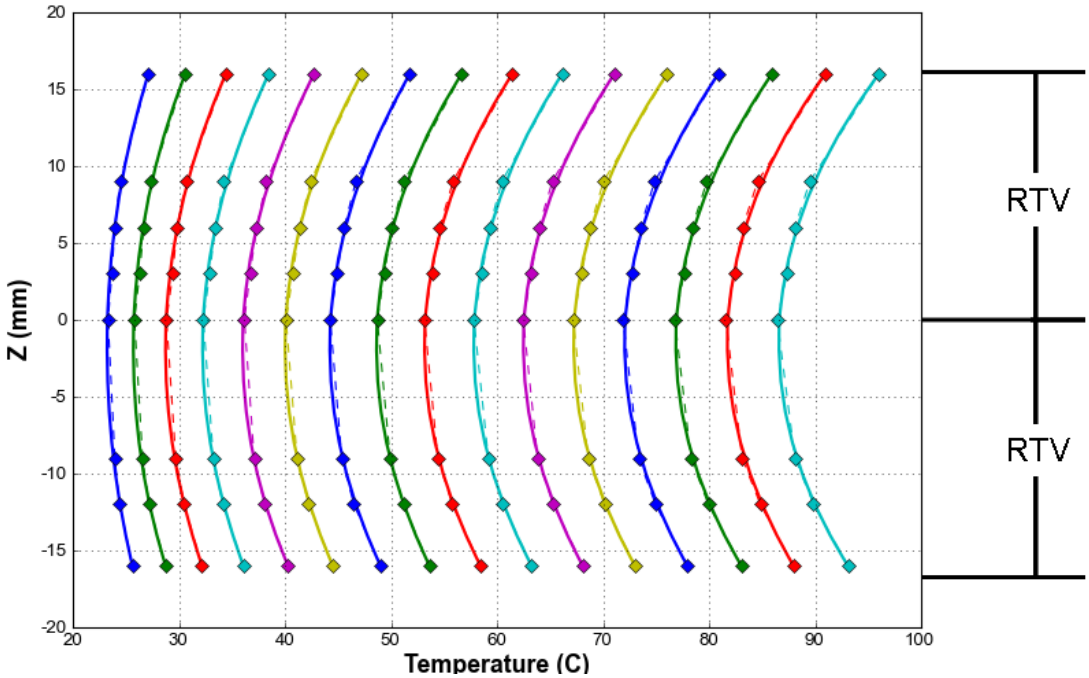

Figure 3-18: Experimental (diamond markers with dashed lines) and simulated (solid lines) through-thickness profiles for Pair 2 at 15 minute intervals.

With the rubber model validated, the through-thickness rubber profile was used to verify the response of the complete system in future tests. The profile through the rubber is affected by the thermal response of the material between the bricks, and if the non-rubber material model is

valid, the simulation results from the material between the bricks *and* the rubber will match the experimental data.

3.2.2.3 FEP and Peel-ply Models

Layers of fluorinated ethylene propylene (FEP) barrier film and peel-ply were tested to measure the thermal resistance and additional uncertainty that resulted from the consumable materials required for vacuum-bagging. Following the procedure of Appendix D, three material stacks were subjected to thermal cycles:

A. 50 layers of FEP

B. 50 layers of peel-ply

C. 2 layers of peel-ply between 2 layers of FEP (Figure 3-19)

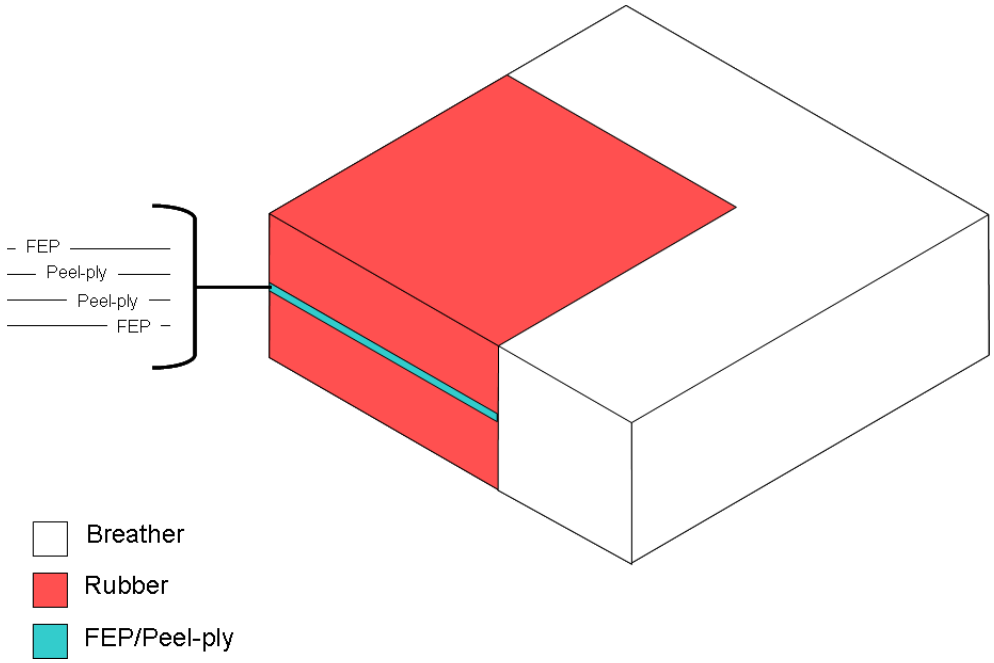

Figure 3-19: Material stack for conductivity test with FEP and peel-ply layers.

A and B used the same autoclave cycle as the two isolated bricks, in Section 3.2.2.1 above. For C, the cycle was:

- heat at 3.0 °C/minute to 180 °C
- cool at 3.0 °C/minute to 20 °C

Tests showed that the consumable materials had measureable effects on the thermal simulation results. The thermophysical properties for the FEP and peel-ply are in Table 3-4.

Table 3-4: Thermal properties of FEP film and peel-ply.

	Density[4] (kg/m^3)	Specific Heat[5] (J/kg K)	Linear Specific Heat Temperature Dependence[5] (J/kg K)/K	Conductivity[4] (W/m K)	Diffusivity[4] (m^2/s)
FEP	1720	775	20	0.5	3.75E-07
Peel-ply	1600	900	10	0.1	6.94E-08

3.2.2.3.1 FEP

The simulated FEP through-thickness profile did not agree with the experimental profile, Figure 3-20. A 1.4 °C gradient from the FEP surface to the midplane was seen in the experimental FEP profile, Figure 3-21. However, the simulated profile was a quadratic, asymmetric profile with a gradient less than 0.5 °C that went from the top to the bottom surface. Therefore, the general assumption of nominal conductive heat transfer through the FEP stack was incorrect. Inconsistent and wrinkled contact surfaces were created by the multiple FEP layers, which led to thermal contact resistances dominating the through-thickness heat transfer in the FEP. The resistance may have been one large resistance, or many smaller resistances that compounded over the thickness of the material stack, Figure 3-21. The exact shape of the profile could not be determined due to insufficient experimental resolution. The time vs. temperature profile had good agreement for the duration of the cycle, and the offset of the profiles resulted from the error in the FEP midplane temperatures, Figure 3-22.

[4] Experimental data from this work
[5] DSC data (Appendix C)

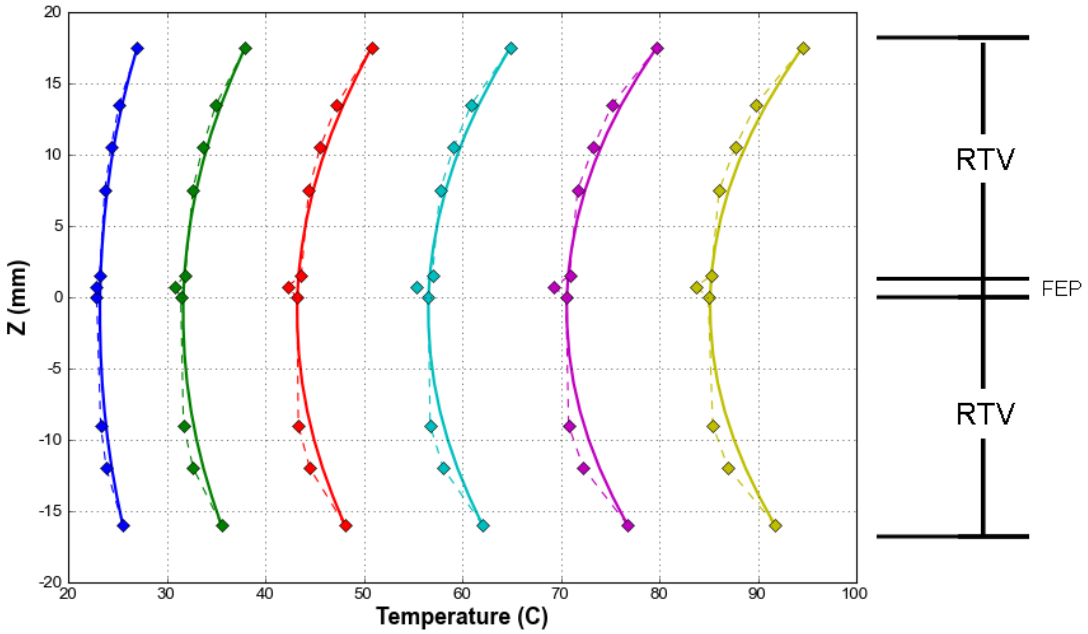

Figure 3-20: Through-thickness profiles for experimental rubber/FEP stack (dashed lines with diamond markers) and simulated rubber/FEP stack (solid lines) at 15 minute intervals.

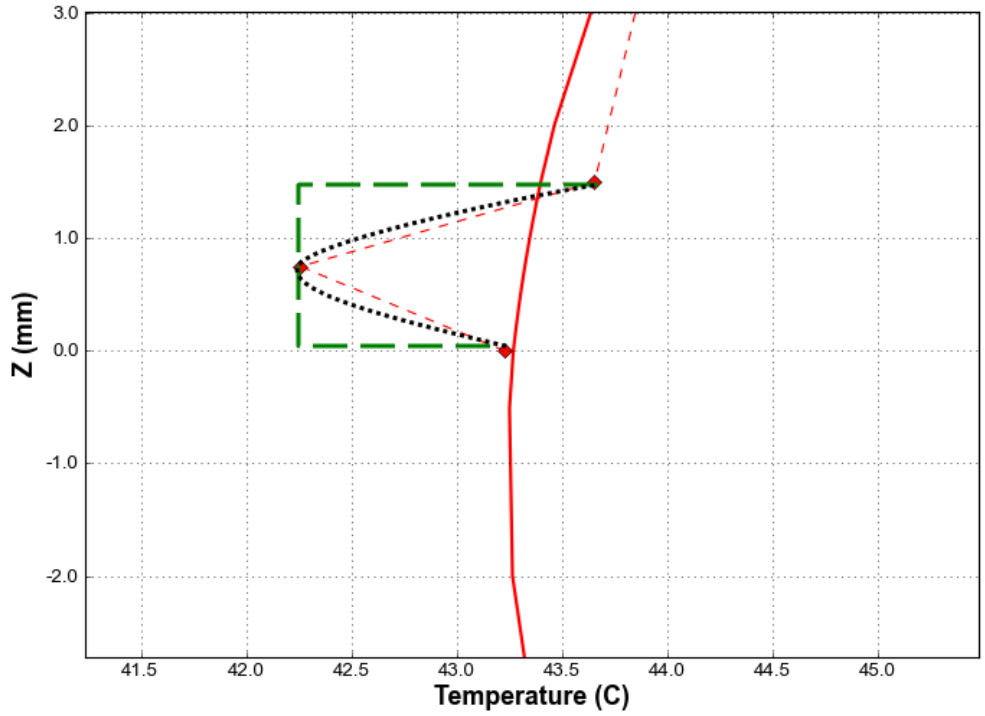

Figure 3-21: Detailed through-thickness profile of experimental FEP stack (dashed line with diamond markers) and simulated FEP stack (solid line). There are two potential profiles through the FEP: a large resistance (green line), or multiple small resistances compounding (black line). The true profile could not be determined due to insufficient experimental resolution.

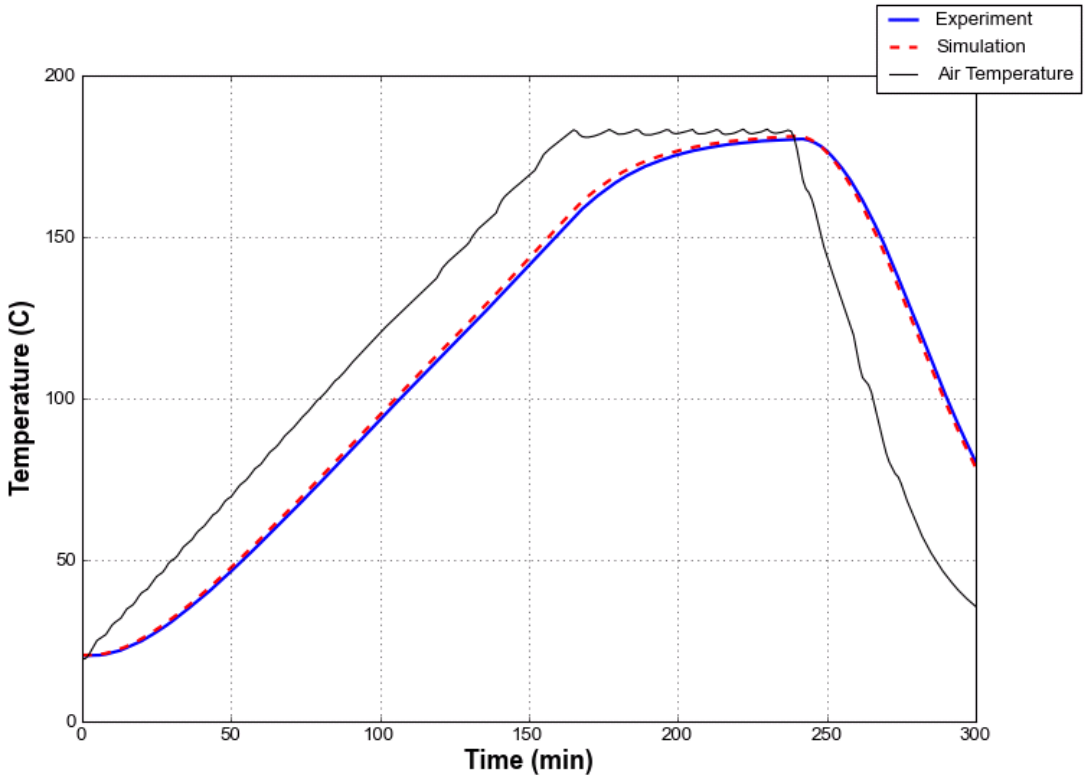

Figure 3-22: Experimental and simulated time vs. temperature profiles for mid-plane of FEP stack.

3.2.2.3.2 Peel-ply

Good agreement was obtained between experimental and simulated results of the peel-ply, Figure 3-23. The largest error, the TC at -12.0 mm, was less than 1.0 °C. Unlike the FEP film, the peel-ply developed a quadratic thermal gradient as one would expect from a poor thermal conductor. Excellent agreement between experimental and simulated midplane temperatures was obtained for the duration of the cycle, Figure 3-24. If peel-ply is modeled, it can therefore be simulated using nominal conduction. However, choosing to ignore two layers of peel-ply in a thermal model would not introduce measurable errors in a simulation, as 50 layers of peel-ply caused a gradient of less than 1.0 °C to develop.

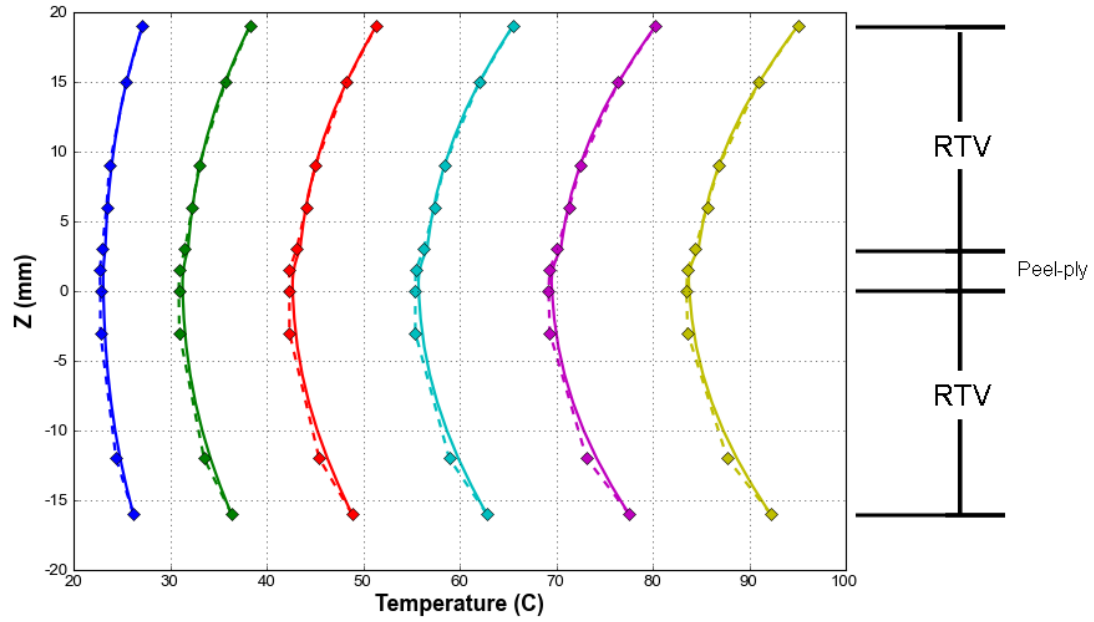

Figure 3-23: Through-thickness temperature profiles for peel-ply conductivity test. Simulation (solid lines) and experimental (diamond markers connected by dashed lines) profiles shown at 15 minute intervals.

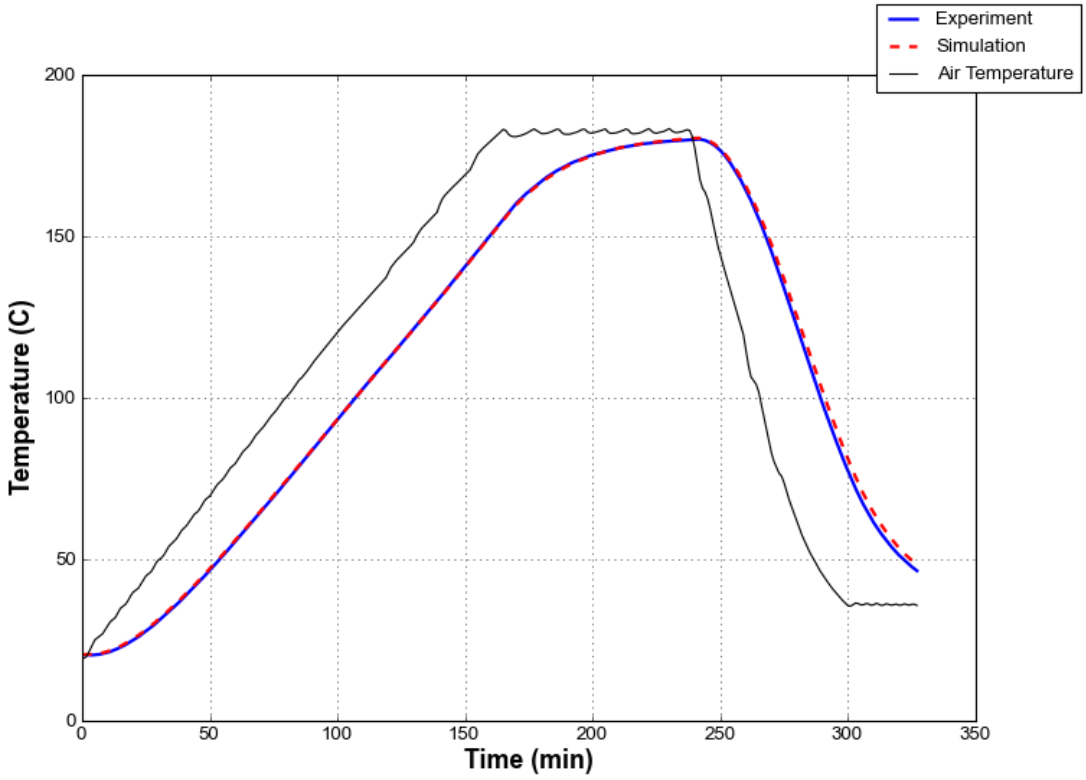

Figure 3-24: Time vs. temperature profiles for the midplane temperature of the peel-ply.

3.2.2.3.3 FEP and Peel-ply Stack

A vacuum-bagged cure assembly would have two layers of FEP and two layers of peel-ply. Testing a stack of the four layers, per Appendix D, showed the additional layers caused a measurable lag at the interface, Figure 3-25 and detailed in Figure 3-26. The adiabatic line for

the simulated stack was near z = -2.0 mm, which was due to the perfect contact in the model that allowed good conduction through the FEP/peel-ply stack. In the experimental stack, the adiabatic line was at z = 0.0 mm, because the contact resistances created by the FEP prevented heat transfer between the two rubber bricks. A consistently shaped gradient through the consumables was not seen since the material layers were thinner than the TC tips, leading to uncertainty about the TC tip z-coordinate. That said, a 0.5 - 0.8 °C discontinuity was visible at the interface. Averaging the interface temperatures gave good agreement in the time vs. temperature profile, Figure 3-27.

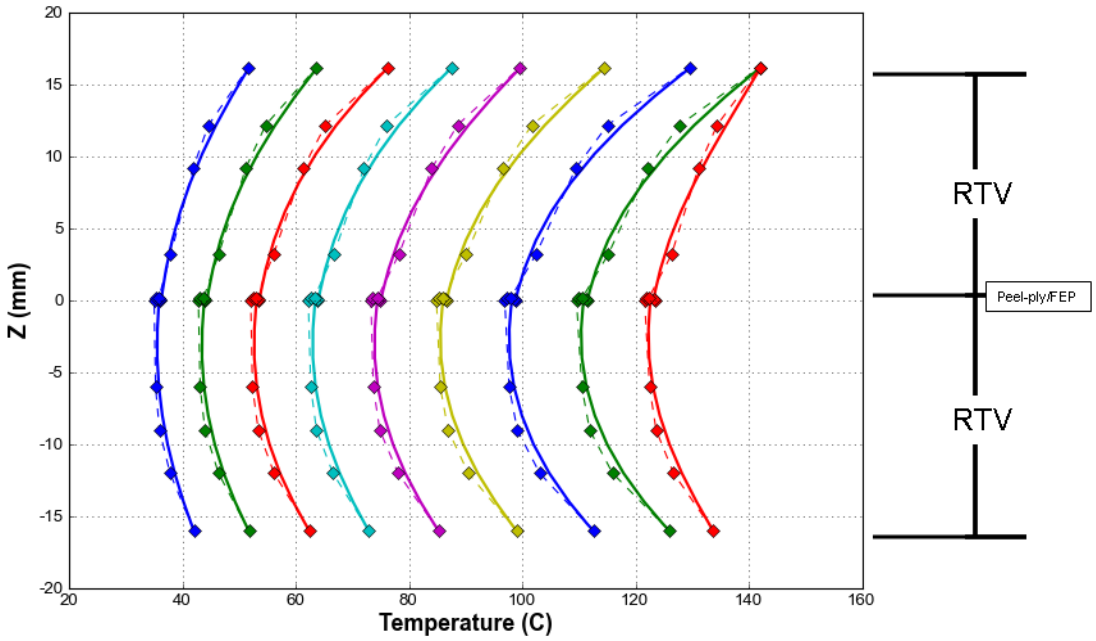

Figure 3-25: Through-thickness profile for KE1204 with FEP and peel-ply at the interface.

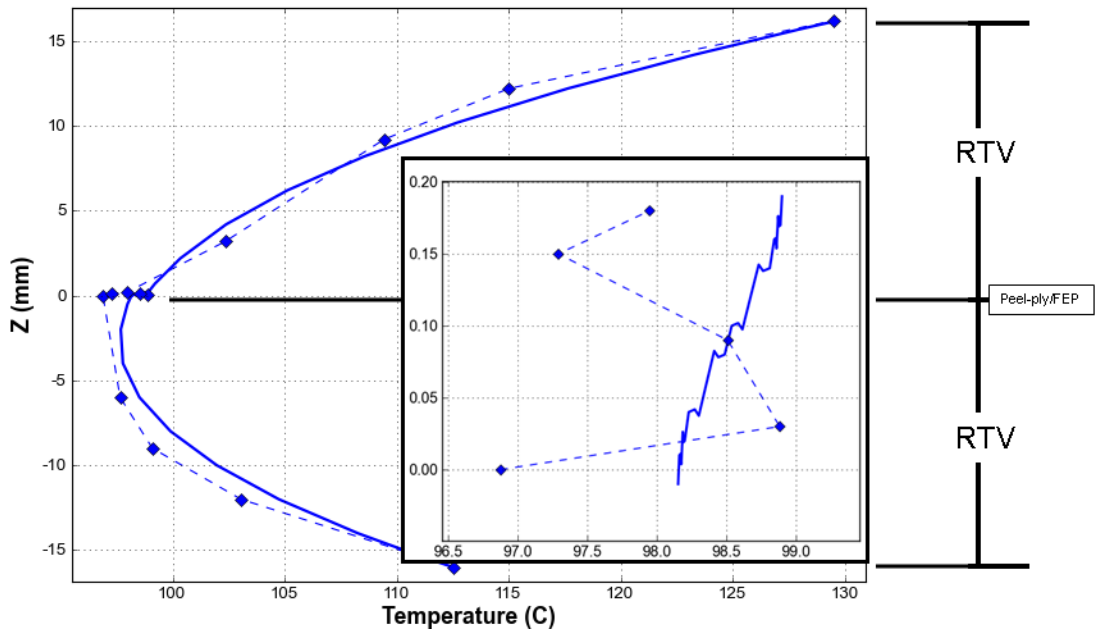

Figure 3-26: Detailed view of through-thickness profile. Note discontinuity that results at both simulated (solid line) and experimental (diamond markers connected by dashed line) profiles that is the result of the additional materials at the interface.

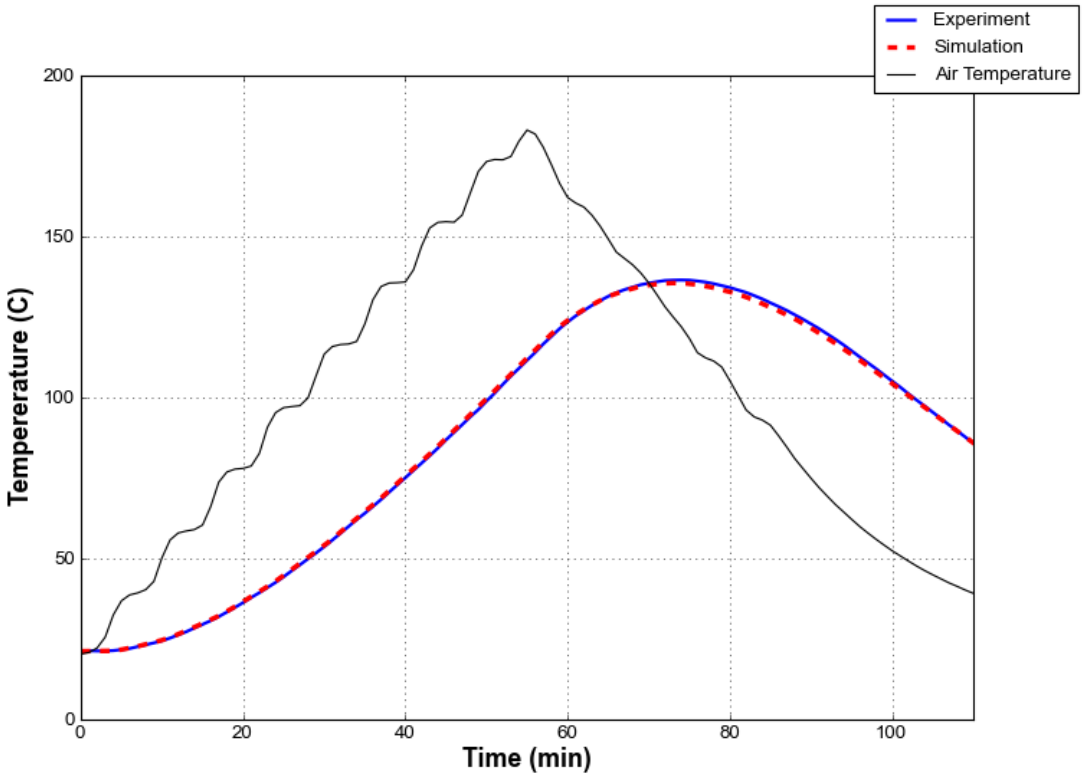

Figure 3-27: Time vs. temperature profile for KE1204 rubber with FEP and peel-ply

3.3 Summary

Several configurations of TCs surrounded by insulating and conducting materials were evaluated for their ability to accurately measure surface temperatures. A TC tip covered by a disc of aluminum foil carefully burnished over the tip was the optimum configuration. The foil

conducted the heat from the surface to the TC tip while isolating the TC from direct contact with the surrounding air.

A methodology was developed to isolate and validate the conductive response of a material. The heat flow through the test apparatus was confirmed to be 1-D. Using the developed validation methodology, the material model for Shin-Etsu KE1204 rubber was validated and showed consistent agreement to within 1.0 °C of experimental data.

The effect of the consumable FEP and peel-ply layers on heat conduction was also tested using the developed methodology. Peel-ply had a predictable thermal response, and can be modeled using nominal conductive heat transfer. However, the contact resistance from FEP wrinkles caused a measureable lag and significantly reduced the heat transfer across interfaces with FEP. If maximum simulation accuracy is desired, the resistance from the FEP layer should be taken into account.

4 Thermochemical Model Validation

In this chapter, the methodology of the 1-D thermal test demonstrated in the previous chapter is further developed to validate the thermochemical response of a composite laminate. Four prepreg materials are tested, and experimental results are compared to simulated results of their respective thermochemical models. Model agreement ranges from excellent, errors less than 1.0 °C, to poor, errors greater than 5.0 °C.

4.1 Thermochemical Model Validation - Methods

The method used in Section 3 is adapted to evaluate a thermochemical composite model. Three changes are required:

- The composite is wrapped in peel-ply and FEP film to control resin bleed.
- The composite mass is recorded before and after cure to calculate V_f.
- The thermal cycle is repeated on the cured composite to provide an inert reference to reduce the uncertainty of the model properties that are unaffected by the curing of the resin.
- The *measured, cured* thickness of the composite is used for both the cured and the uncured simulations.

Four prepreg material systems were evaluated using the methods outlined in Appendix E:

- Advanced Composites Group CF2426A/ MTM45-1
- Hexcel AS4/8552
- Toray T800S/3900-2
- Toray P707AG-15/2510

4.2 Results and Discussion

4.2.1 ACG CF2426A/MTM45-1

ACG CF2426A/MTM45-1 is an out-of-autoclave, tool free post-cure prepreg system. 30 and 50 ply laminates were constructed from ACG CF2426A/MTM45-1 5-harness-satin prepreg. Both laminates were wrapped in peel-ply, but not the layer of FEP film. The 120.0 °C cure cycle was:

- heat at 0.5 °C/minute to 120.0 °C
- hold for 240 minutes

- cool at 5.0 °C/minute to 20.0 °C

Cure was followed by a 180.0 °C post-cure cycle:

- heat at 5.0 °C/minute to 180.0 °C
- hold for 180 minutes
- cool at 5.0 °C/minute to 20.0 °C

Both cycles were repeated for the fully cured laminates.

V_f was higher than nominal due to resin bleed that occurred during cure, Table 4-1 and Table 4-2. The resin bled because peel-ply alone was not an adequate barrier to prevent the edge of the laminate from bleeding into the breather insulation. The peak temperatures and timing of the exotherms had excellent agreement; there was 0.2 °C difference for the 30 ply, and 1.1 °C difference for the 50 ply experiments and simulations.

Table 4-1: Cured and uncured properties of 30 and 50 ply CF2426A/MTM45-1 laminates.

	Uncured mass (g)	Cured mass (g)	Uncured Thickness (mm)	Cured Thickness (mm)	V_f	Nominal V_f
30 Ply	189.8	166.8	14.0	10.75	0.65	0.54
50 Ply	316.4	283.7	22.9	18.5	0.63	0.54

Table 4-2: Timing and peak temperatures of 30 and 50 experimental and simulated CF2426A/MTM45-1 laminates.

	Peak Temp (Experiment) °C	Peak Temp (Simulation) °C	Time of Peak (Experiment) min	Time of Peak (Simulation) min
30 Ply	129.0	129.2	324	324
50 Ply	134.2	135.3	330	336

Although there was significant resin bleed, a 1-D simulation at a nominal V_f was used to approximate the composite behavior. Further discussion of why a 1-D approximation is acceptable can be found in Appendix F, and the following results are for a 1-D simulation using nominal V_f.

4.2.1.1 Cured

First, the cured laminate results are analyzed. There was less than 2.0 °C difference between the experimental and simulated profiles of the fully cured 30 and 50 ply laminates, Figure 4-1 and Figure 4-2. The error is attributed to the high V_f, which raised the laminate's thermal conductivity. For example, the cured 50 ply laminate had a 1.3 °C gradient in the simulation with the nominal V_f, but a 0.0 °C gradient in the experiment, Figure 4-2.

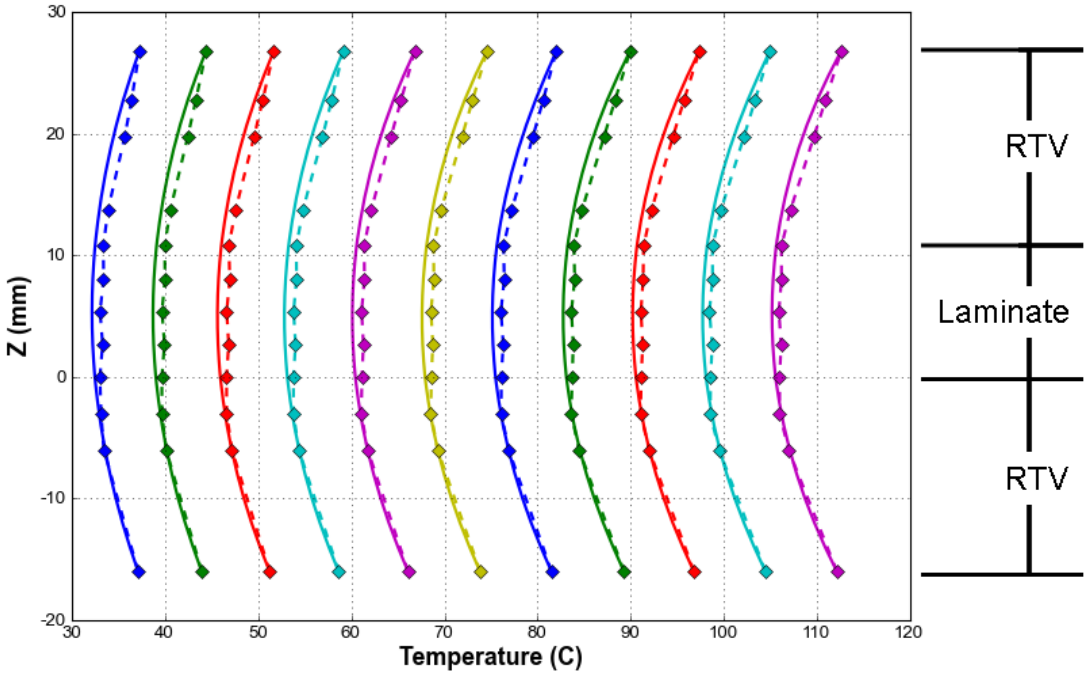

Figure 4-1: Through-thickness profiles of simulated (solid lines) and experimental (diamond markers with dashed lines) cured 30 ply CF2426A/MTM45-1 laminates at 15 minute intervals.

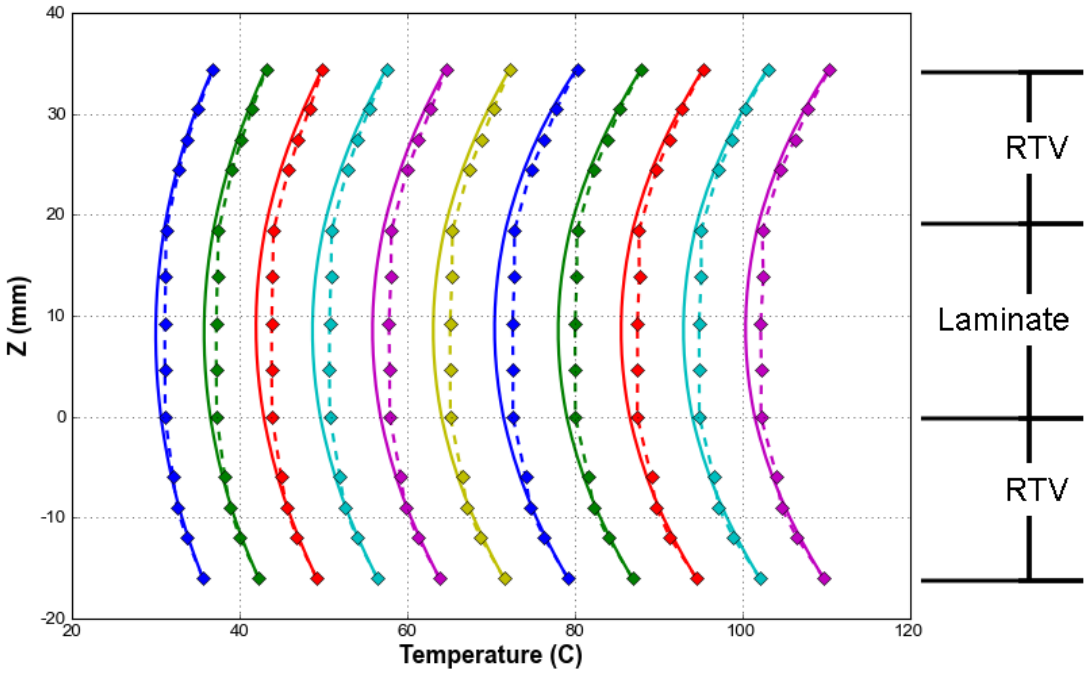

Figure 4-2: Through-thickness profiles of simulated (solid lines) and experimental (diamond markers with dashed lines) cured 50 ply CF2426A/MTM45-1 laminates at 15 minute intervals.

Time vs. temperature profiles had excellent agreement throughout the entire cycle, Figure 4-3 and Figure 4-4. There was a lag of less than 1.0 °C in the simulation.

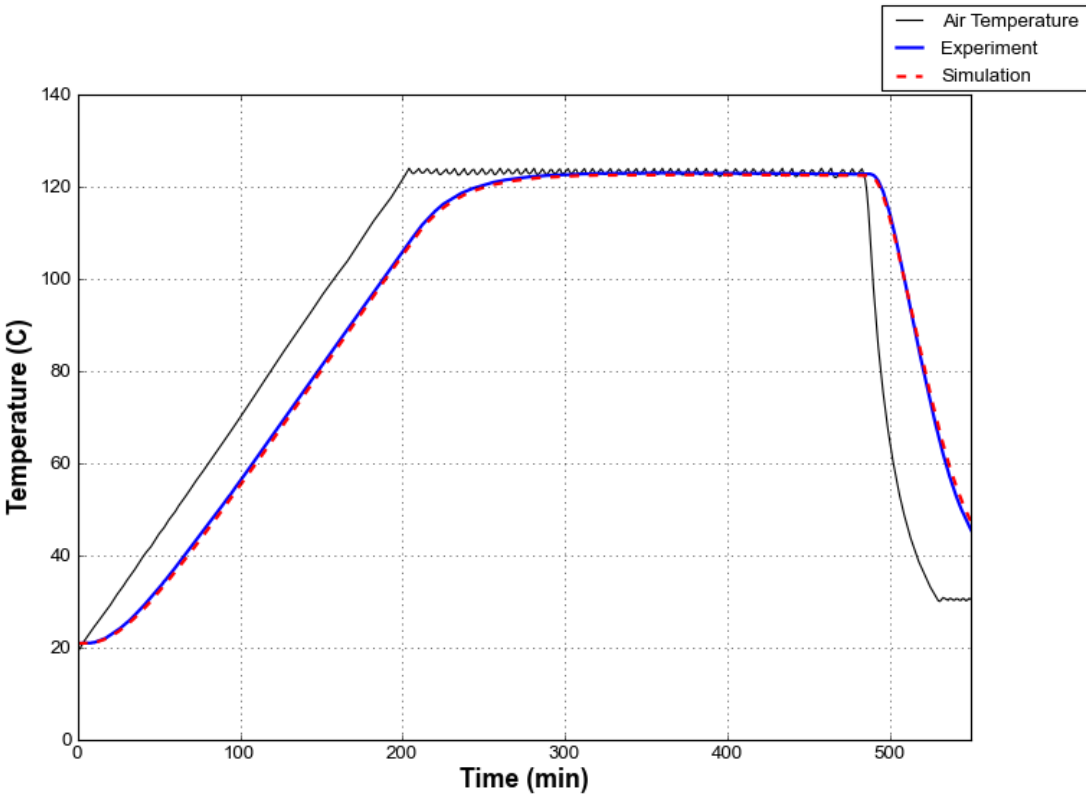

Figure 4-3: Time vs. temperature for cured 30 ply CF2426A/MTM45-1 laminate.

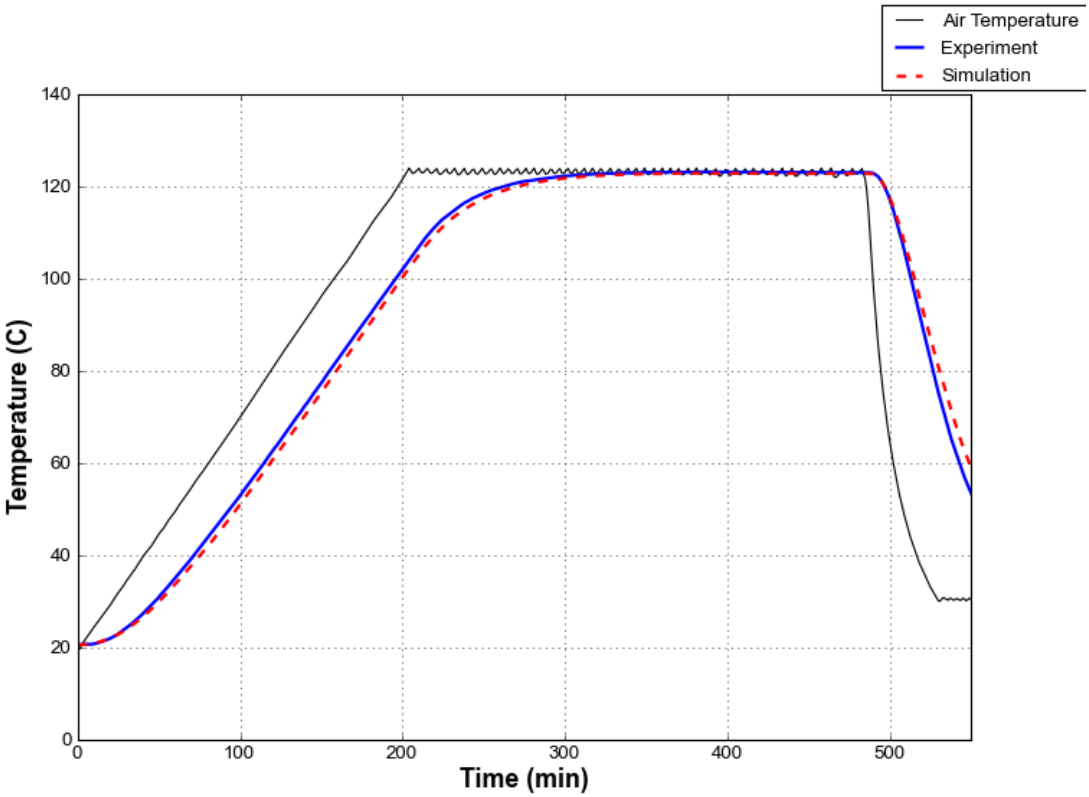

Figure 4-4: Time vs. temperature profile for cured 50 ply CF2426A/MTM45-1 laminate.

4.2.1.2 Uncured

At the start of the cycle, the experimental and model conductivities were similar and the through-thickness thermal gradients matched, Figure 4-5. Resin flow was not modeled, so when the laminate gradient decreased from the increasing V_f, the simulation gradient remained constant. Equation (2-5) can be solved for k to calculate the change in thermal conductivity required for the through-thickness gradient to go from 2.2 °C to 0.0 °C, and conductivity had to increase by 2100% to eliminate the gradient over the 18.5 mm thick laminate, Table 4-3. 11.22 W/m K, although not possible to calculate using the Springer-Tsai formula and published k_{22} values for AS4 fibers, was reasonable when compared to the through-thickness conductivities in work that accounted for fiber-fiber contact and high V_fs (1 – 17 W/m K by G. Zhang et al. (2010)).

Table 4-3: Change in the 50 ply laminate conductivity needed to reduce the through-thickness thermal gradient to zero. Nominal conductivity was calculated with the Springer-Tsai formula (Springer & Tsai, 1967)**.**

	Gradient °C	Conductivity W/m K	V_f
Nominal/simulation	2.2	0.51	0.54
Experimental	0.1	11.22	0.63
% Difference		+2100.0%	-16.7%

The curing through-thickness profile showed the cure reaction started near 110 °C. At 110 °C, the laminate temperature began to lead the rubber brick interface temperature because of the internal heat generation of the cure reaction. Since the previously discussed conductivity differences caused the experiment temperatures to lead the simulation, the simulation reaction started 15 minutes later than the experiment. After 30 minutes, the simulation reaction caught up with and matched the experimental temperatures for the remaining 200 minutes of the hold.

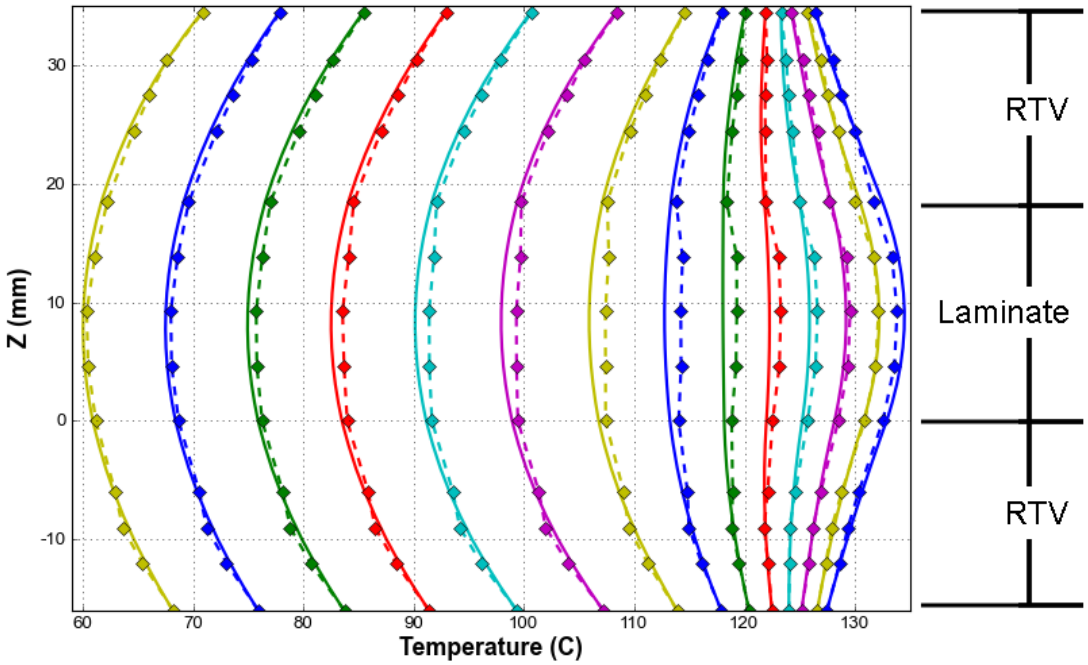

Figure 4-5: Through-thickness profiles of simulated (solid lines) and experimental (diamond markers connected by dashed lines) uncured 50 ply CF2426A/MTM45-1 laminates at 15 minute intervals. Note increase in thermal conductivity of laminate as temperature increases.

The post exotherm cooling profile was not perfectly captured by the simulation because the model did not account for the change in specific heat capacity that resulted from the increased volume fraction, Figure 4-6 and Figure 4-7. At nominal V_f, the simulated laminate had a marginally higher heat capacity (886 J/kg K) than the experiment (850 J/kg K), and therefore took longer to cool down. The effect was less noticeable in the 30 ply laminate because the laminate was less thermally massive.

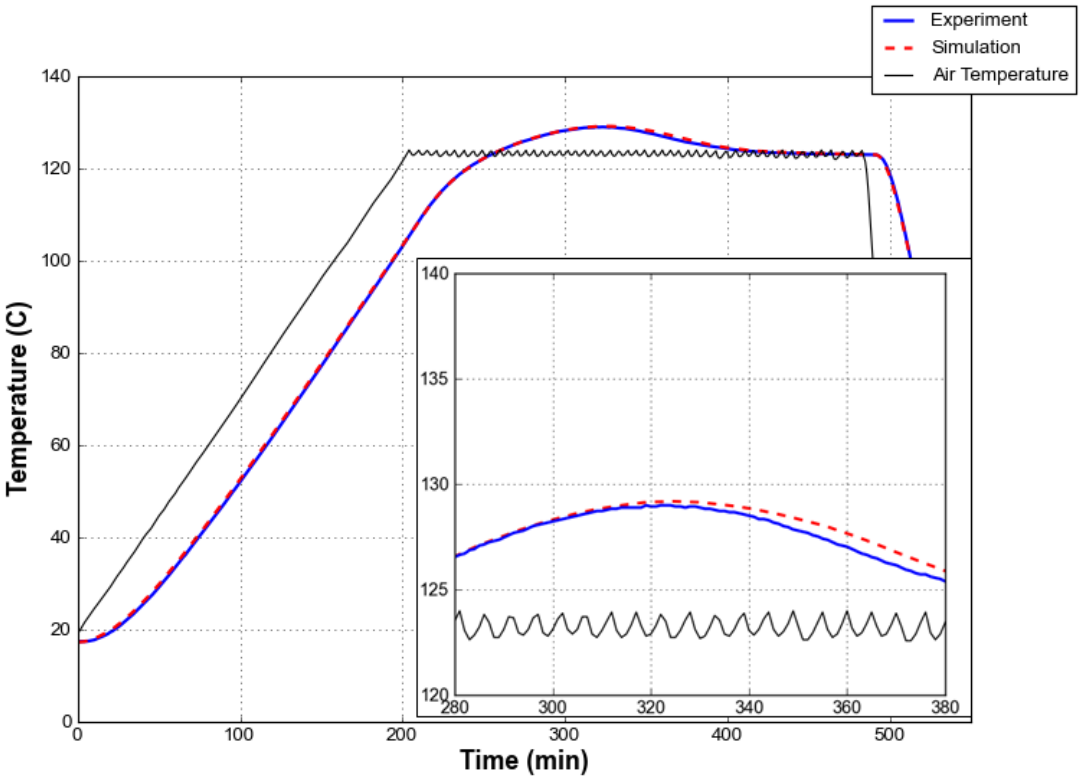

Figure 4-6: Time vs. temperature for uncured 30 ply CF2426A/MTM45-1 laminate

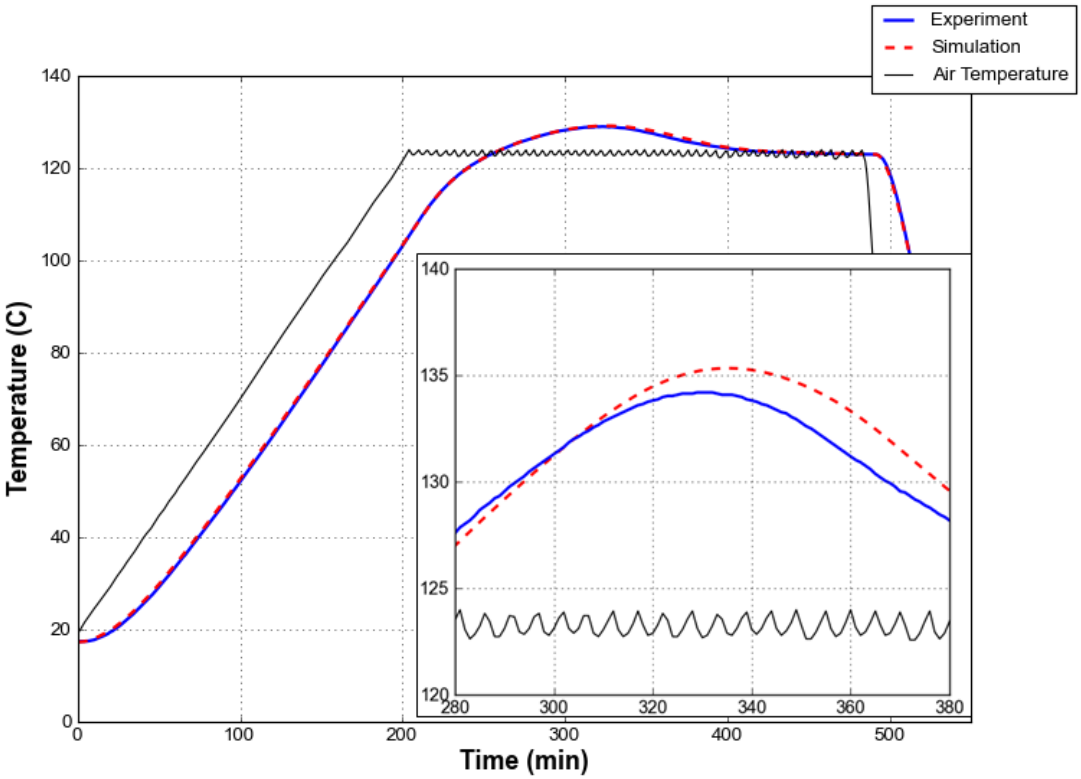

Figure 4-7: Time vs. temperature for uncured 50 ply CF2426A/MTM45-1 laminate

4.2.1.3 Post-Cure

The developed test methodology was sensitive enough to measure the small amount of heat generated during the post-cure exotherm. The final degree of cure (DoC) from the curing simulations was used as the initial DoC for the post-cure simulations. Good agreement occurred between the experiment and the simulation, Figure 4-8 and Figure 4-9. The simulation accurately captured the small amount of heat generated during the post-cure. The 50 ply, fully cured, laminate was off by up to 3.0 °C as a result of the error in thermal conductivity. The differences were more pronounced during the post-cure cycle because the ramp rate was higher, 5.0 °C/minute vs. 0.5 °C/minute, and the 50 ply laminate was 7.75 mm thicker than the 30 ply laminate. The area between the post-curing and cured curves was the total heat generation from the post-cure process.

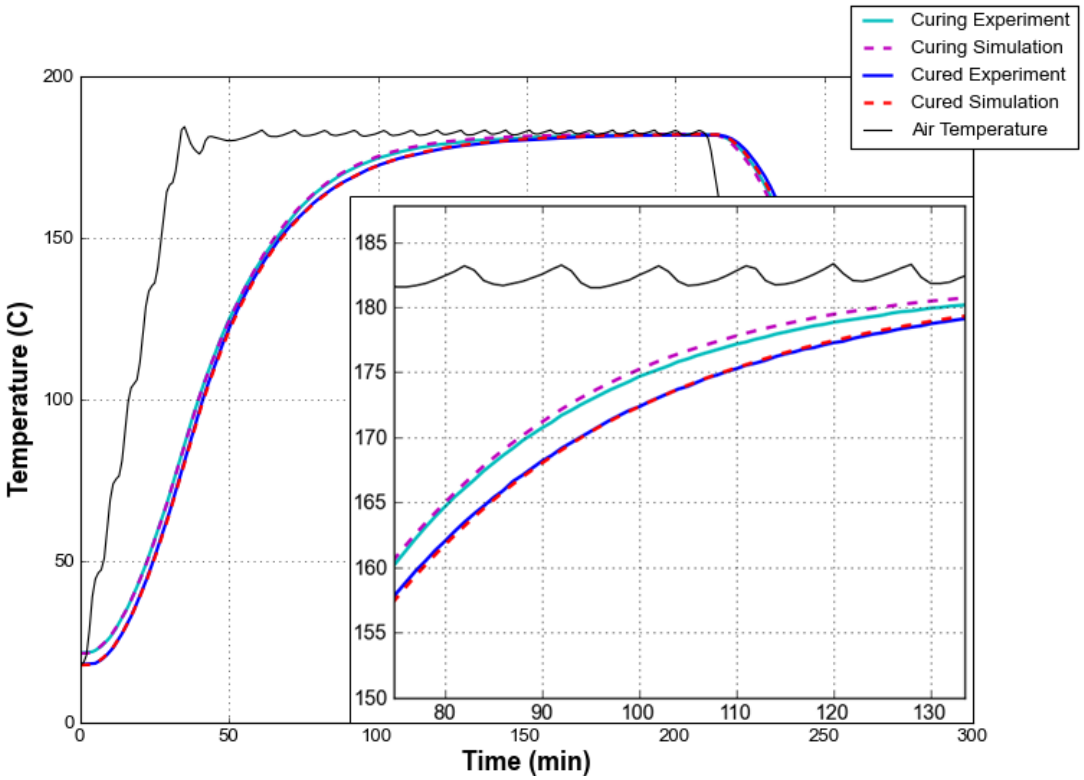

Figure 4-8: Post-curing and fully cured time vs. temperature profiles for 30 ply CF2426A/MTM45-1 laminate.

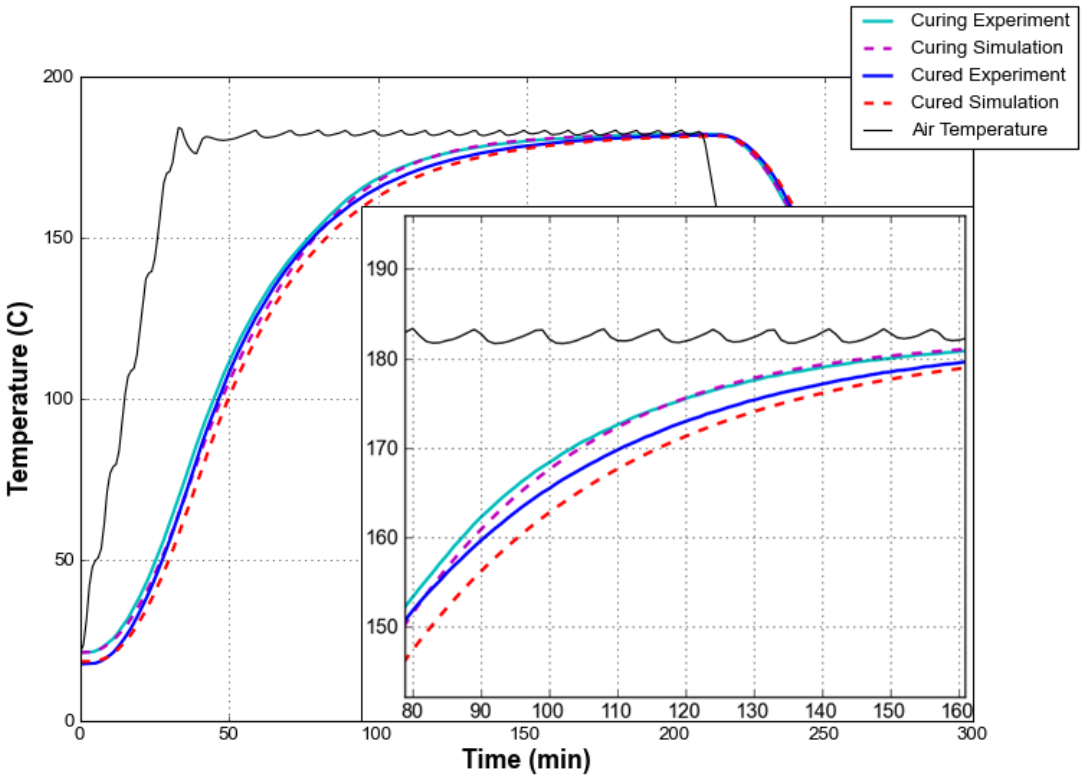

Figure 4-9: Post-curing and fully cured time vs. temperature profiles for 50 ply CF2426A/MTM45-1 laminate.

4.2.2 Hexcel AS4/8552

AS4/8552 is a widely used autoclave cure material system. 60 and 80 ply $[0/90]_s$ laminates were made from unidirectional Hexcel AS4/8552 tape and tested per the procedures in Appendix E. The 180.0 °C cure cycle was:

- heat at 1.25 °C/minute to 180.0 °C
- hold for 180 minutes
- cool at 5.0 °C/min to 20.0 °C

Both experimental laminates were at nominal V_f, but they also had exotherms that exceeded the temperature limit of 190.0 °C for the material models, Table 4-4 and Table 4-5. Two AS4/8552 material models were available for comparison to the experimental data. One model was from the NCAMP database and the other was a model compiled from open literature data (Hubert, Johnston, Poursartip, & Nelson, 2001).

Table 4-4: Cured and uncured properties of 60 and 80 ply AS4/8552 laminates.

	Uncured mass (g)	Cured mass (g)	Uncured Thickness (mm)	Cured Thickness (mm)	V_f	Nominal V_f
60 Ply	184.0	182.0	12.31	11.66	0.58	0.57
80 Ply	244.3	241.2	16.25	14.65	0.58	0.57

Table 4-5: Timing and peak temperatures of experimental and simulated 60 and 80 ply AS4/8552 laminates.

	Peak Temperature (°C)			Time of peak (minutes)		
	Exp	Open Lit.	NCAMP	Exp	Open Lit	NCAMP
60 Ply	196.5	190.7	192.8	160	173	152
80 Ply	202.0	193.9	197.1	160	175	158

4.2.2.1 Cured

The 60 ply simulation led the experiment, but the 80 ply simulation lagged the experiment, Figure 4-10 and Figure 4-11. Uncertainties introduced into the system by the FEP layer, not the different laminate thicknesses, caused the different behaviors. One layer of FEP film and one layer of peel-ply were modeled at the rubber/composite interfaces. Both laminate's through-thickness profiles showed good agreement through the outer half of the rubber, but deviated as they neared the rubber/composite interface. The 60 ply experimental profile showed lag at the interfaces similar to the contact resistance induced lag in the FEP/Peel-ply stack from Section 3.2.2.3.3. The 80 ply experimental profile lacked the discontinuity at the interfaces; the experimental profile was like the continuous MTM45-1 profile in 4.2.1.1, which lacked the layers of FEP. However, uncertainties introduced by the FEP layer did not prevent simulation predictions from being within the 2.0 °C target.

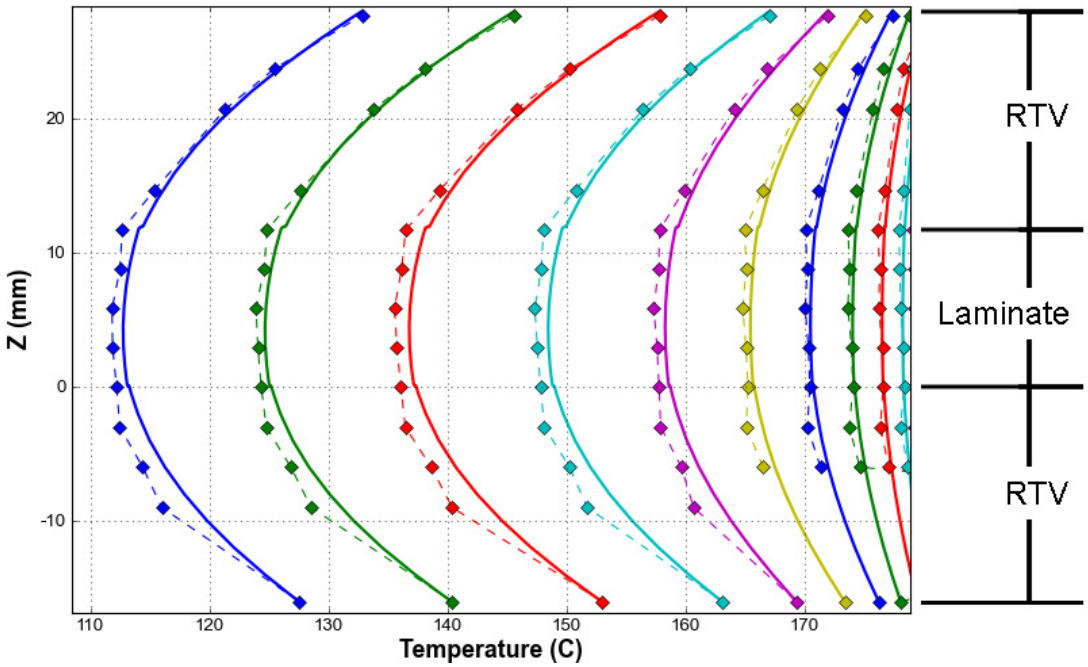

Figure 4-10: Through-thickness profile of cured 60 ply AS4/8552 laminate and NCAMP material model.

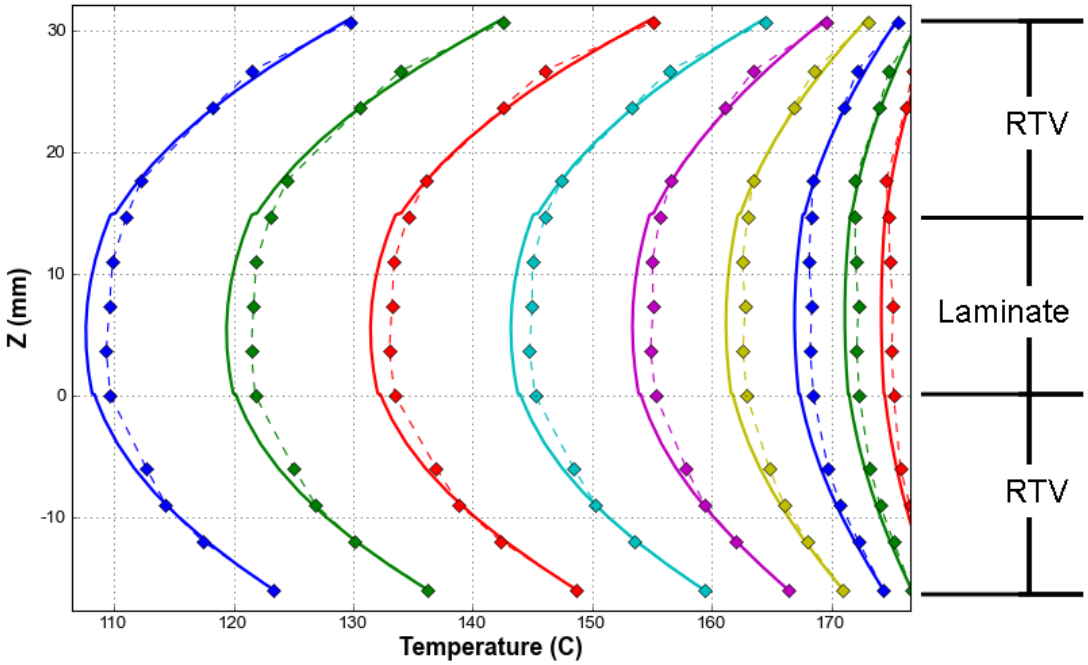

Figure 4-11: Through-thickness profile of cured 80 ply AS4/8552 laminate and NCAMP material model

Agreement at the midplane of the cured laminates was within 2.0 °C for both laminates and both models, Figure 4-12 and Figure 4-13. The cured simulations had similar behaviors, and both captured the heating and cooling rates of the experimental laminates.

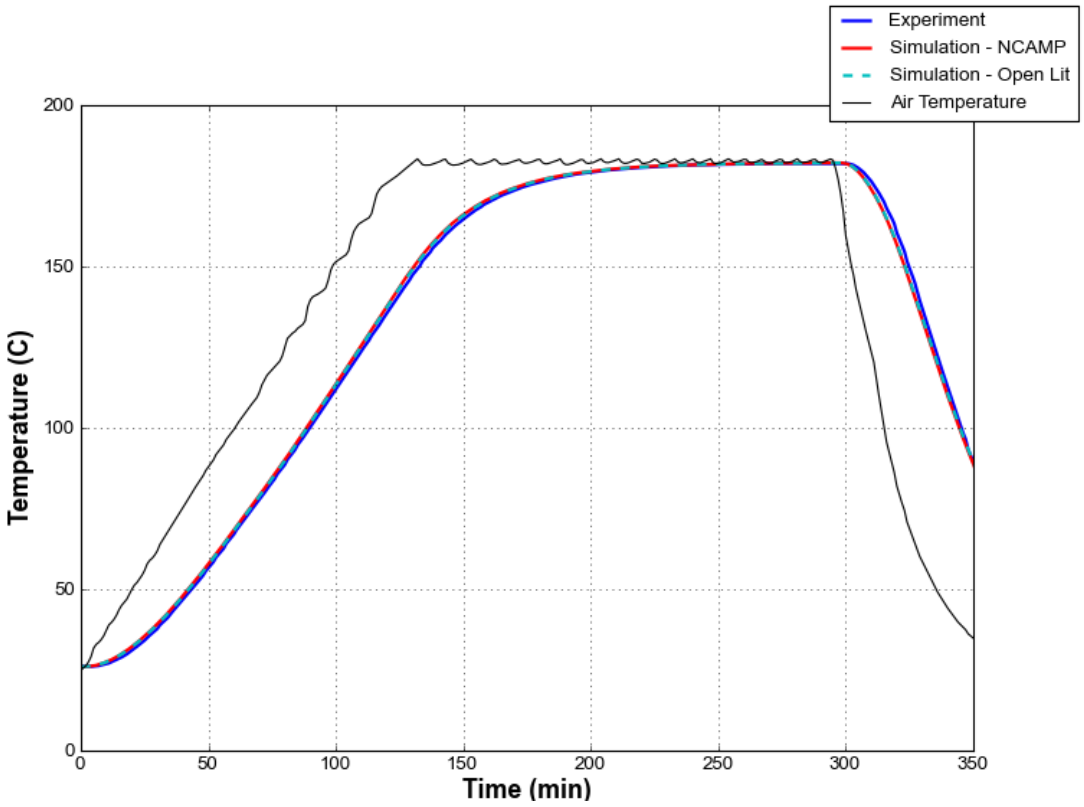

Figure 4-12: Comparison of cured 60 ply AS4/8552 laminate and two material models

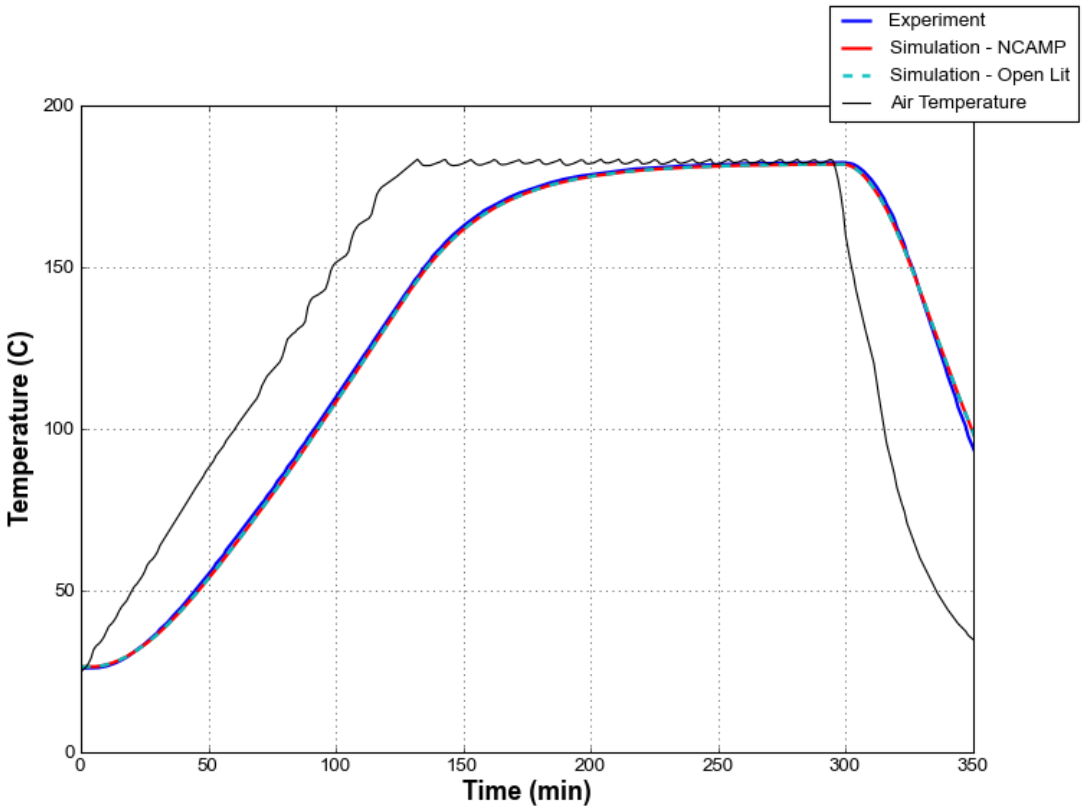

Figure 4-13: Comparison of cured 80 ply AS4/8552 laminate and two material models

4.2.2.2 Uncured

During cure, both laminates had large peak exotherms. The models under-predicted the peak temperatures, but they were outside of their validated envelope of 190.0 °C. Although the peak prediction was wrong, the NCAMP model had excellent agreement up to the 190.0 °C model limit. However, the Open Literature model consistently under-predicted the reaction rate and peak temperatures, Figure 4-14 and Figure 4-15.

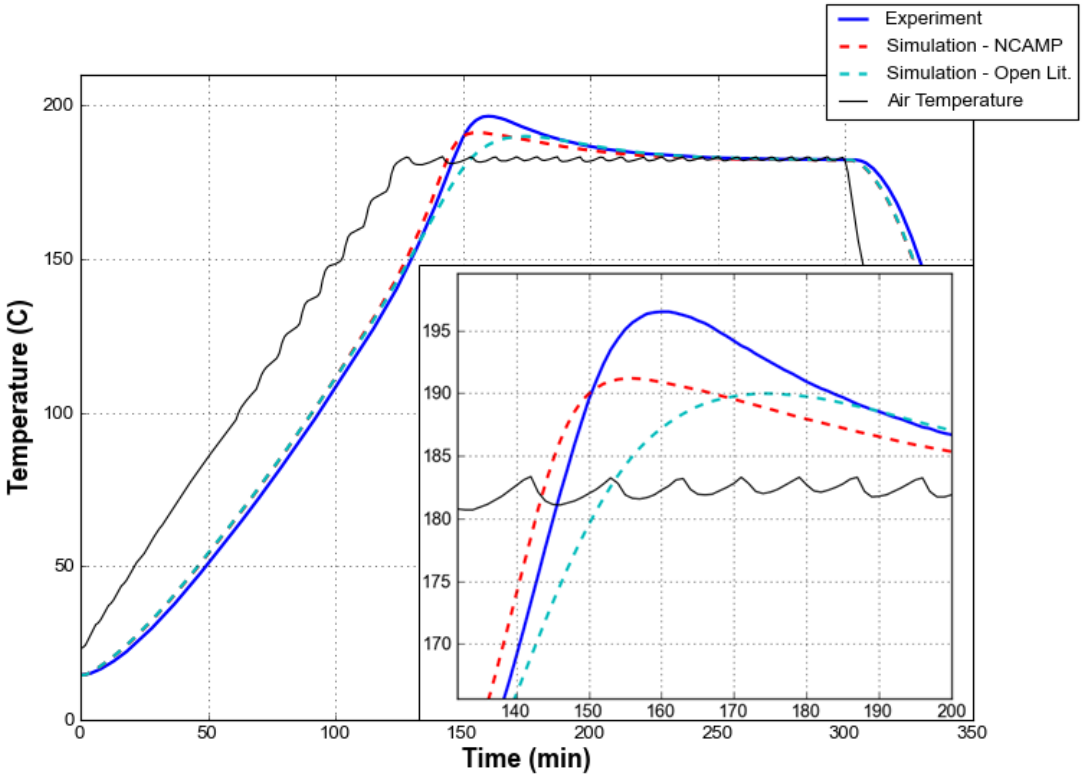

Figure 4-14: Comparison of uncured 60 ply AS4/8552 with NCAMP and Open Lit. material models

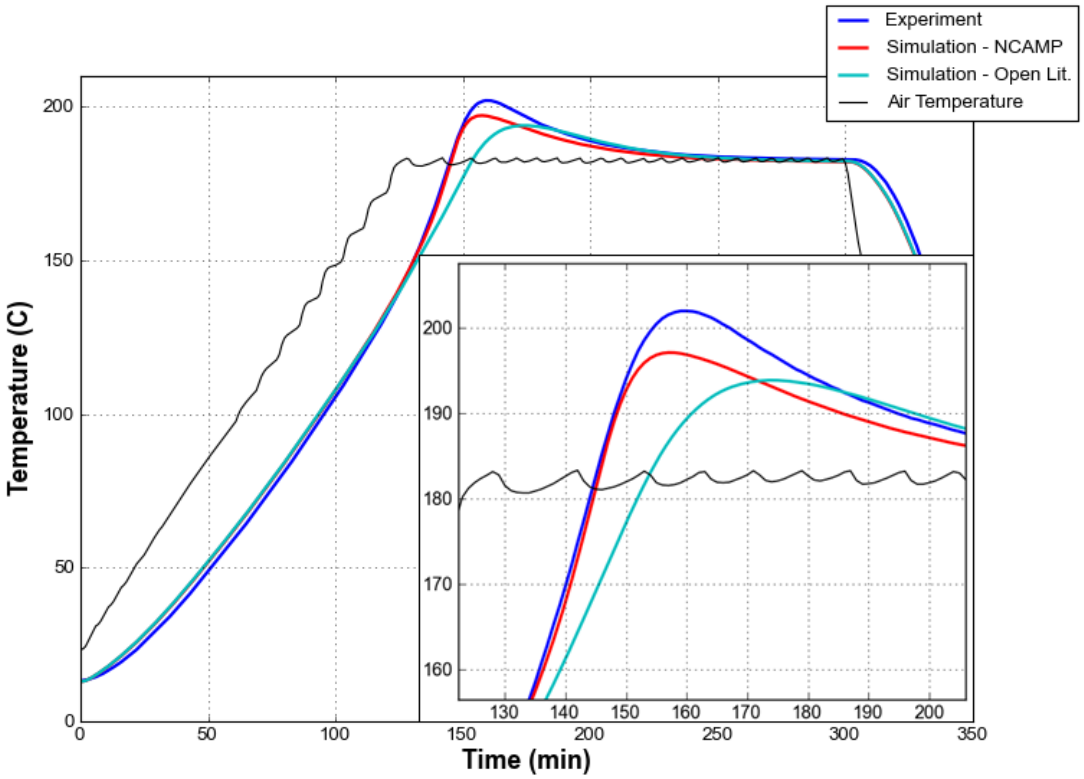

Figure 4-15: Comparison of uncured 80 ply AS4/8552 with NCAMP and Open Lit. material models

The through-thickness profiles showed the NCAMP reaction started within 5 minutes of the experiment, and the reaction developed at similar rates in the simulation and experiment, Figure 4-16. The development of the reaction in the NCAMP simulation closely matched the experiment up to the 190.0 °C limit of the model validation. Comparing the reactions of the different models showed the delay in the start of the Open Literature reaction, and its slower reaction rate, Figure 4-17. The NCAMP model led the Open Literature model before the reaction started because heat capacity is modeled differently; it is a function of temperature in the Open Literature model, but it is a more detailed function of temperature and degree of cure in the NCAMP model. Conductivity, however, is the same in both models and thus the simulations had similar through-thickness thermal gradients.

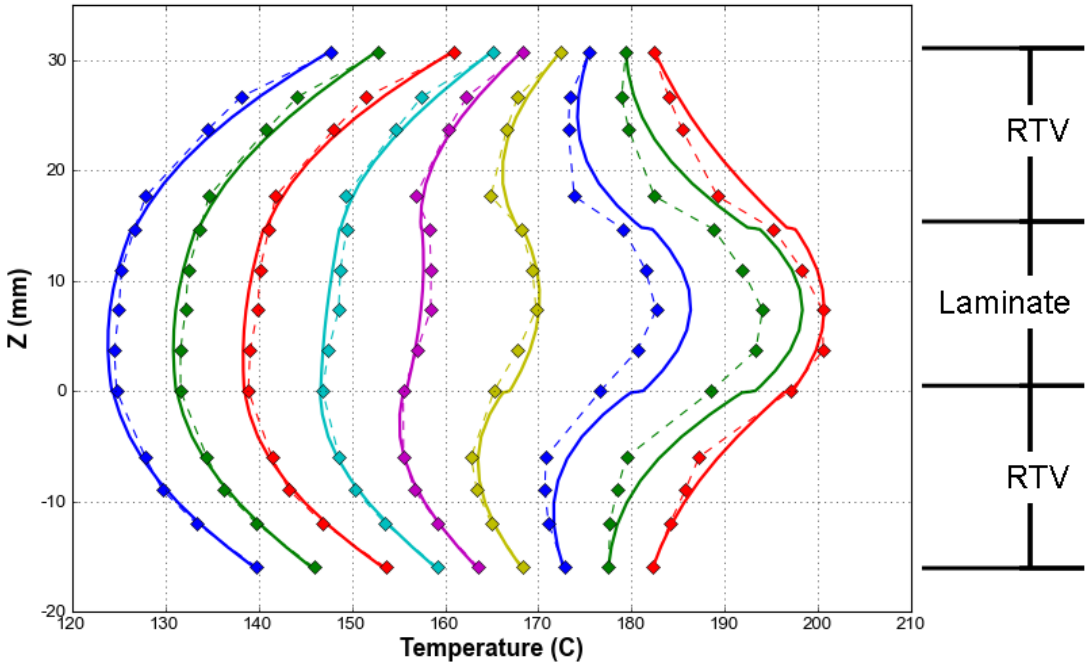

Figure 4-16: Comparison of cure reactions in AS4/8552 NCAMP (solid lines) and experimental (dashed lines) profiles at five minute intervals.

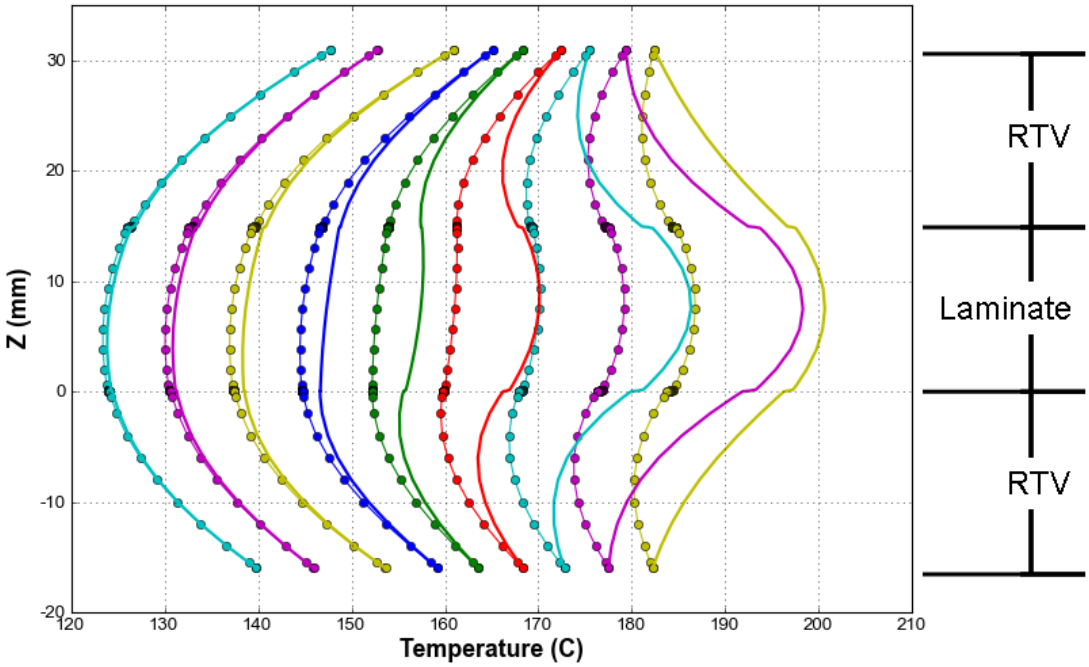

Figure 4-17: Comparison of cure reactions in AS4/8552 NCAMP (solid lines) and Open Lit. (solid lines with markers) models at five minute intervals.

In summary, two models designed to simulate the same material had significant variation in their thermal responses during cure. The developed validation methodology showed that the NCAMP model captured the onset and development of the cure reaction best. In practice, the failure to predict temperatures to within 2.0 °C above the 190.0 °C validation limit should not be

considered a reason to dismiss the validity of the model. The goal of processing is to maintain temperatures within the processing window of ± 5.0 °C, and the model was within the 2.0 °C target in this region of interest.

4.2.3 Toray T800H/3900-2

T800H/3900-2 is another widely used autoclave cure prepreg material system. Two 40 ply $[0/90]_s$ laminates of T800H/3900-2 were cured. One laminate was allowed to bleed freely by removing the FEP and peel-ply layers, and the other laminate was constructed with the standard procedure outlined in Appendix E. The cure cycle was:

- Pressurize to 90 psig
- Heat at 5.0 °C/minute to 180.0 °C
- Hold for 120 minutes
- Pressurize to 0 psig
- Cool at 5.0 °C/minute to 20.0 °C

The freely bled laminate had a higher V_f, lower thickness, and smaller exotherm, Table 4-6 and Table 4-7. Resin bleed was quantified by the mass loss, and was visible during post-cure inspection, Figure 4-18. For simulation, a model developed in Dykeman (2008) and provided to the author by Convergent Manufacturing Technologies Inc. was used.

Table 4-6: Cured and uncured properties of nominal and high V_f, 40 ply T800H/3900-2 laminates.

	Uncured mass (g)	Cured mass (g)	Uncured Thickness (mm)	Cured Thickness (mm)	V_f	Nominal V_f
40 Ply V_f = 0.58	123.44	121.29	8.69	7.54	0.58	0.572
40 Ply V_f = 0.68	126.0	110.0	-	6.25	0.68	0.572

Table 4-7: Timing and peak temperatures of experimental and simulated nominal and high V_f, 40 ply T800H/3900-2 laminates.

Peak Temperature (°C)			Time of Peak (minutes)		
Experiment V_f = 0.58	Experiment V_f = 0.68	Simulation V_f = 0.57	Experiment V_f = 0.58	Experiment V_f = 0.68	Simulation V_f = 0.57
189.5	186.3	188.9	145	142	151

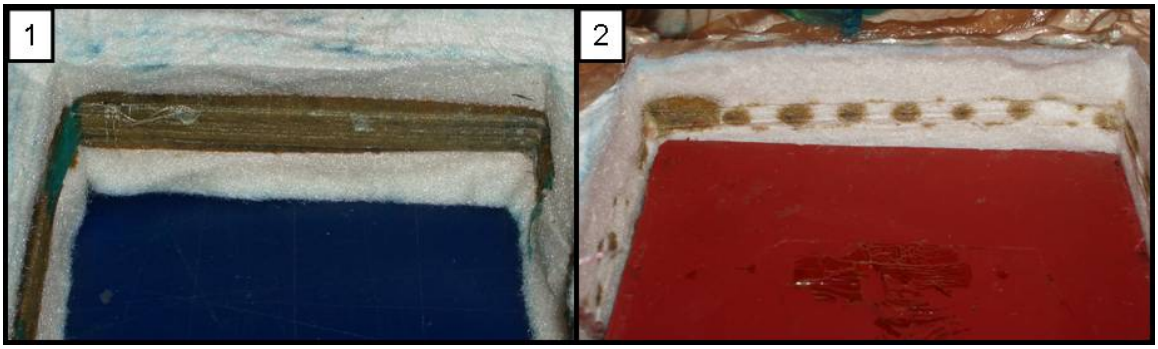

Figure 4-18: Breather insulation from the laminate allowed to bleed freely, Frame 1, and the laminate wrapped in perforated FEP, Frame 2.

4.2.3.1 Cured

The thermal histories of the bled and nominal laminates varied as a result of resin loss, Figure 4-19. As with MTM45-1 in 4.2.1.1, the volume of fraction of fibers increased with resin bleed, which increased the conductivity of the laminate. The through-thickness gradient of the bled laminate was 0.0 °C compared to 1.6 °C for the nominal laminate.

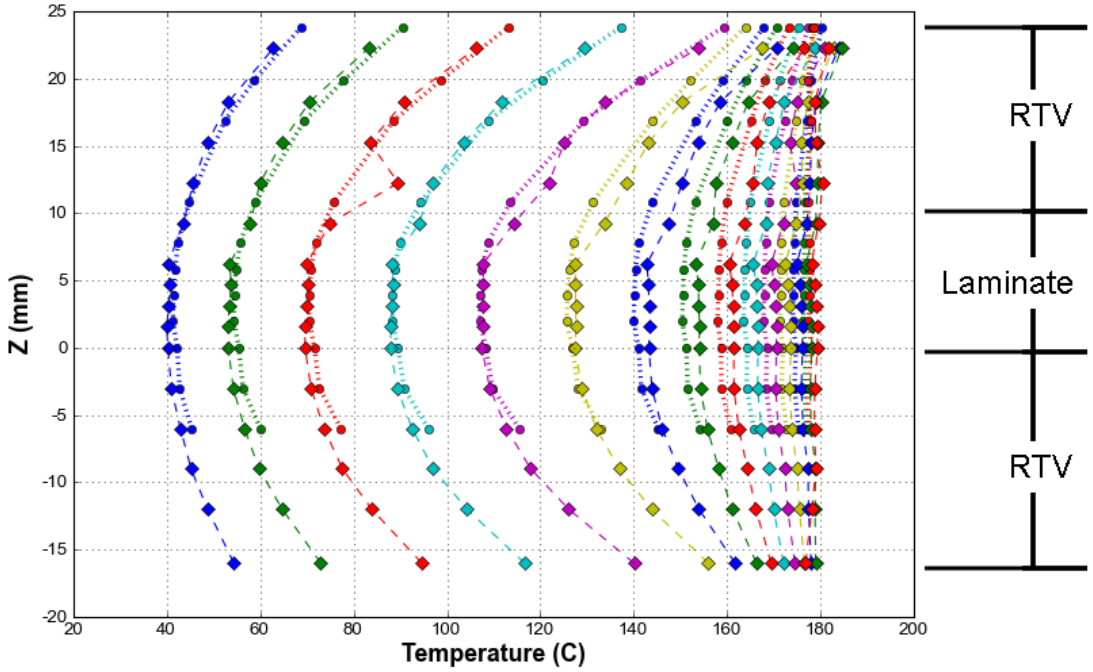

Figure 4-19: Through-thickness profiles of fully cured T800H/3900-2 nominal V_f (0.58) laminate (dotted lines with circle markers) and high V_f, 0.68, laminate (dashed lines with diamond markers) at 5 minute intervals. (A complete profile for the nominal laminate was prevented by TC failures)

The nominal laminate and *top* rubber brick had excellent agreement with the cured experiment, Figure 4-20. Errors up to 7.0 °C were recorded from the bottom brick. The lag in the bottom brick was caused by the pressure from the cycle collapsing the breather such that it became 'T'

shaped instead of rectangular, Figure 4-21. The non-uniform shape of the breather created a local heat sink from z = 0.0 to z = -6.0 mm.

Results from the top brick remained valid above the adiabatic line since heat transfer through the top brick remained 1-D. The pleats in the bagging material disrupted the airflow around the areas of thinned breather and continued to insulate the edges of the brick. The stagnant air had poor heat transfer, so there was still good agreement between the experimental and simulated rubber profiles and interface temperatures for the top brick. The midplane temperatures of the nominal V_f experiment and simulation had excellent agreement for the duration of the cycle, Figure 4-22. The high V_f laminate led the nominal laminate and nominal simulation by as much as 2.8 °C during the hold. The increased diffusivity of the high V_f laminate caused it to heat faster since temperature changes are primarily driven by thermal diffusivity at the hold.

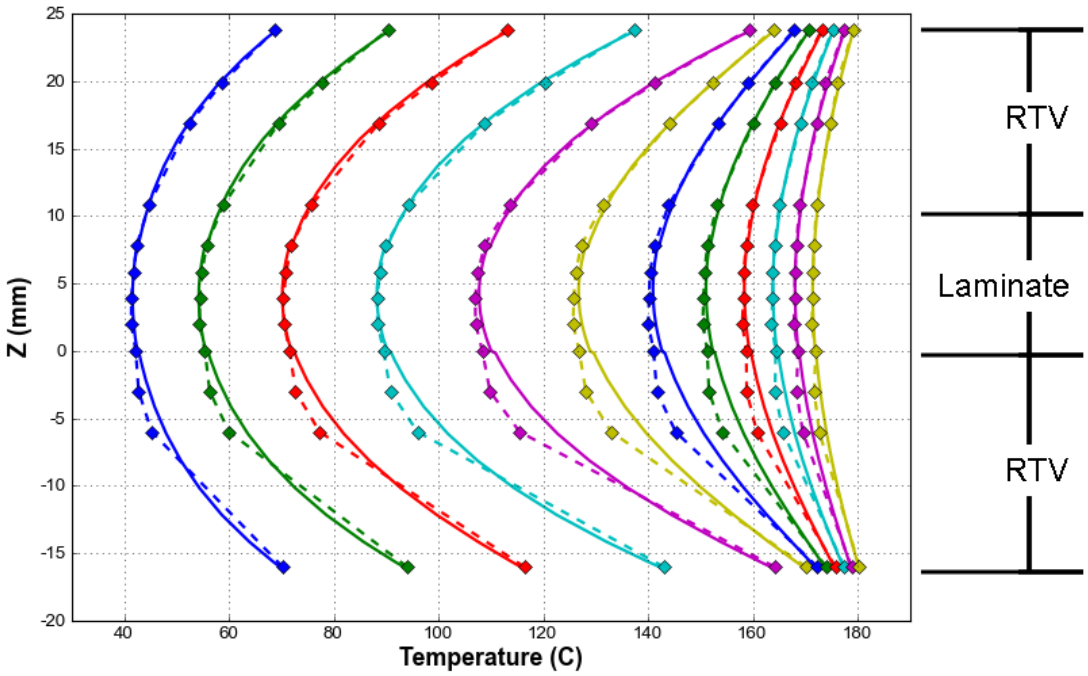

Figure 4-20: Through-thickness profiles of cured T800H/3900-2 nominal Vf (0.58) laminate (dashed lines with diamond markers) and 1-D simulation (solid line) at 5 minute intervals.

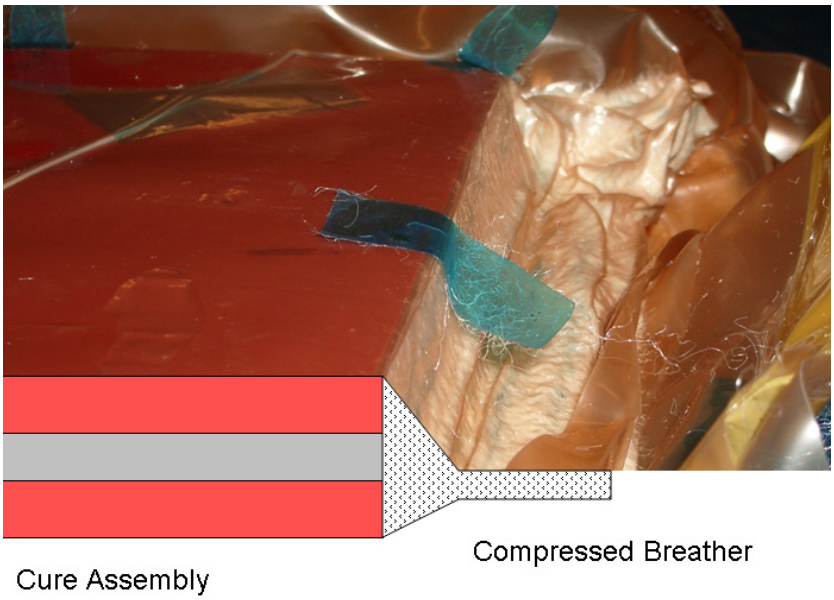

Figure 4-21: Improperly compressed breather that acted as a heat sink on the lower rubber brick.

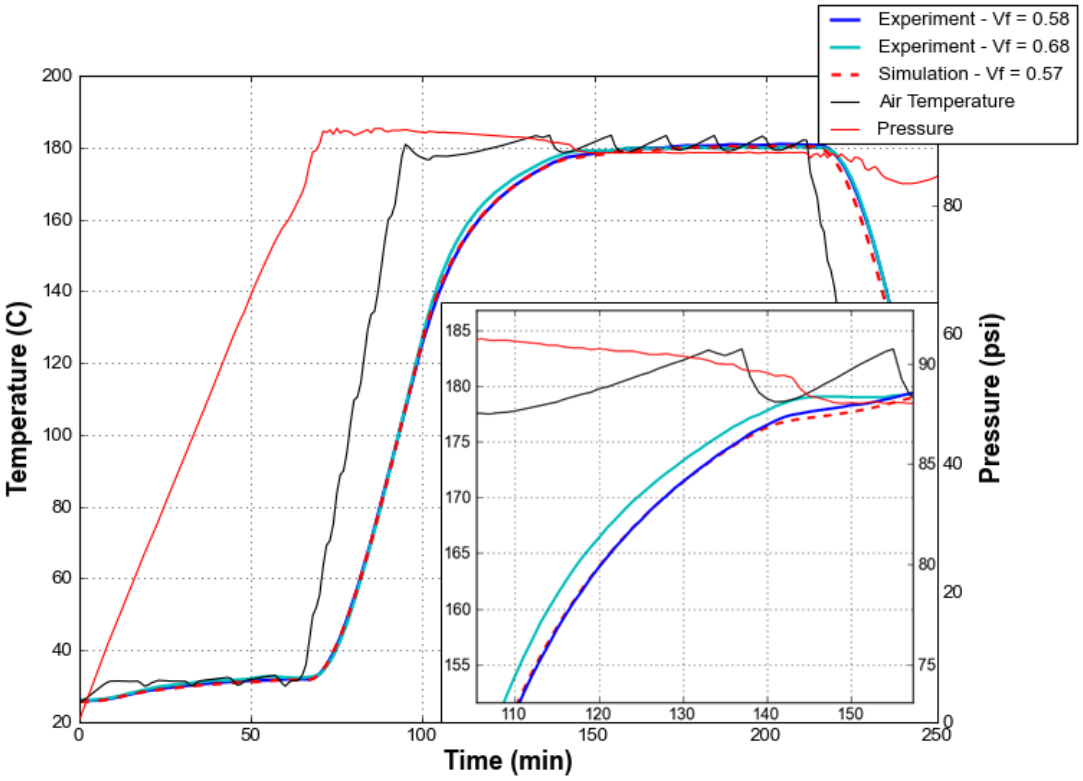

Figure 4-22: Time vs. temperature profiles of cured T800H/3900-2 nominal V_f (0.58) laminate, cured high V_f (0.68) laminate, and simulated nominal V_f (0.57) laminate.

4.2.3.2 Uncured

Since there was no change to the experimental stack in-between cycles, the bottom brick of the uncured experiment also had a poor fit between z = 0.0 and z = -6.0 mm for the nominal V_f laminate. The gradient in the high V_f laminate went to zero near 120.0 °C, due to resin bleed,

and the laminate had a lower peak temperature, Figure 4-23. The experimental profiles matched until the reactions peaked, where the bled laminate peaked 3.2 °C lower and 3 minutes earlier than the nominal V_f laminate because of the resin loss. The simulation missed the start of the reaction by 5 minutes and the reaction developed more slowly, Figure 4-24. Time vs. temperature profiles confirmed the slow reaction development, Figure 4-25. The simulation lagged both experiments by more than 8.0 °C at 130 minutes, even though the peak temperature was with 0.6 °C of the experiment. For the model to fully capture the cure reaction, reevaluating the rate of reaction in 3900-2 kinetics model is needed, but that was beyond the scope of this work. Matching peak temperatures and exotherm timing did not mean the model has been validated. The complete profile must be analyzed, as it is the complete thermal history that shows the validity of a model.

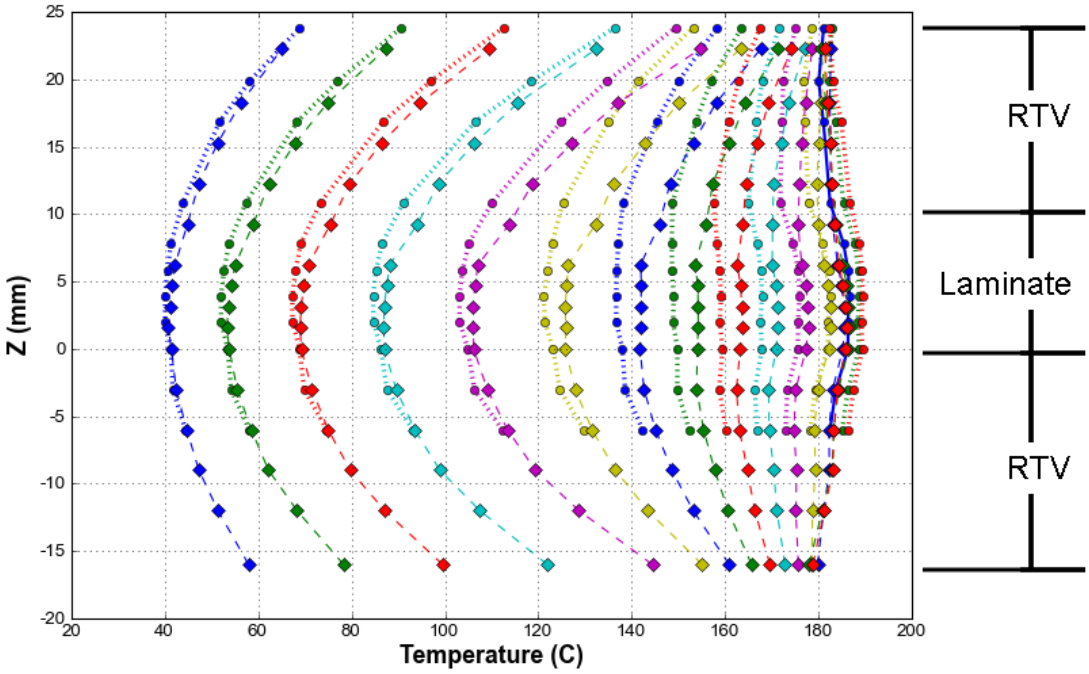

Figure 4-23: Through-thickness profiles of uncured T800H/3900-2 nominal V_f (0.58) laminate (dotted line with circle markers) and high V_f, 0.68, laminate (dashed lines with diamond markers) at 5 minute intervals.

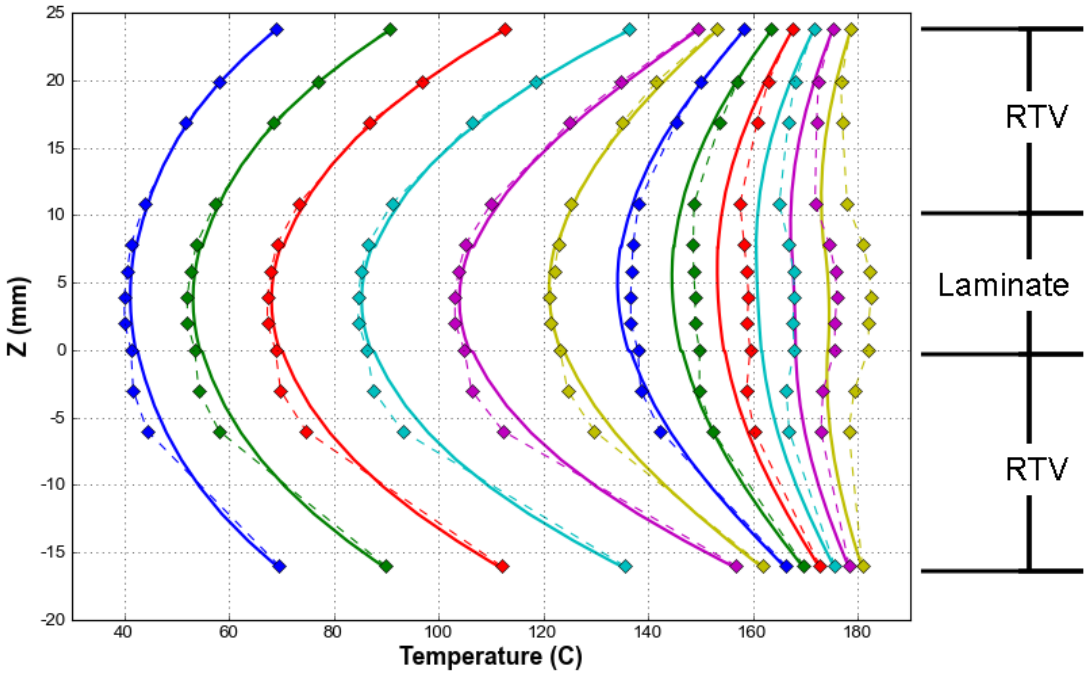

Figure 4-24: Through-thickness profiles of uncured T800H/3900-2 nominal V_f (0.58) laminate (dashed lines with diamond markers) and 1-D simulation (solid line) at 5 minute intervals.

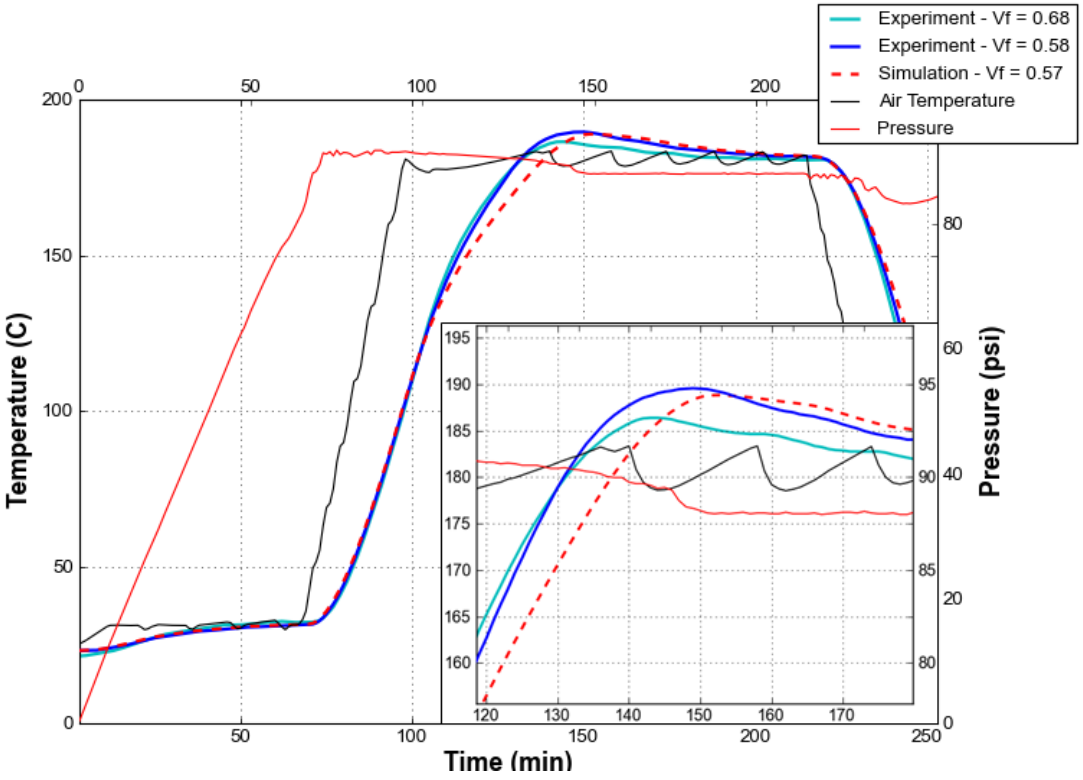

Figure 4-25: Time vs. temperature profiles of uncured T800H/3900-2 nominal V_f (0.58) laminate, uncured high V_f (0.68) laminate, and simulated nominal V_f (0.57) laminate. Inset shows detail view of exotherm peak.

4.2.4 Toray T700/2510

Two laminates were made from prepregs using the Toray 2510 resin system. One prepreg was 60 plies of uni-directional tape from T700G fibers. The second prepreg was 40 plies of plain-weave fabric from T700S fibers. The laminates were equivalent thicknesses and cured using the same cycle. The autoclave cycle was:

- heat at 1.0 °C/minute to 130.0 °C
- hold for 120 minutes
- cool at 5.0 °C/minute to 20.0 °C

The tape and fabric forms have different V_fs, but both laminates were highly reactive. The different resin content of the tape vs. fabric prepregs resulted in significant variation in peak temperatures, Table 4-8 and Table 4-9. The thicknesses of the two panels were within 0.5 mm, as were the times of the peak exotherms, but a 15.2 °C difference in peak temperatures resulted from the 0.06 difference in the V_fs.

Table 4-8: Cured and uncured properties of 60 ply tape and 40 ply fabric P700T/2510 laminates

	Uncured Mass (g)	Cured Mass (g)	Uncured Thickness (mm)	Cured Thickness (mm)	Vf	Nominal Vf
60 Ply Tape	146.0	142.9	9.3	8.9	0.59	0.57
40 Ply Fabric	138.7	131.5	9.8	8.4	0.53	0.50

Table 4-9: Exotherm timing and peak temperature of 60 ply tape and 40 ply fabric P700T/2510 laminates.

	Peak Temperature (°C)		Time of Peak (minutes)	
	Experiment	Simulation	Experiment	Simulation
60 Ply Tape	165.4	152.6	126	125
40 Ply Fabric	180.2	168.6	126	123

4.2.4.1 Cured

Thermal histories of the cured tape and fabric were nearly identical, Figure 4-26 and Figure 4-27. The material model used for the simulations was specifically for the tape, but there was excellent agreement between both experiments and the tape simulation, Figure 4-27 and Figure 4-28. The simulation was within 1.0 °C of both experiments for the duration of the cycle.

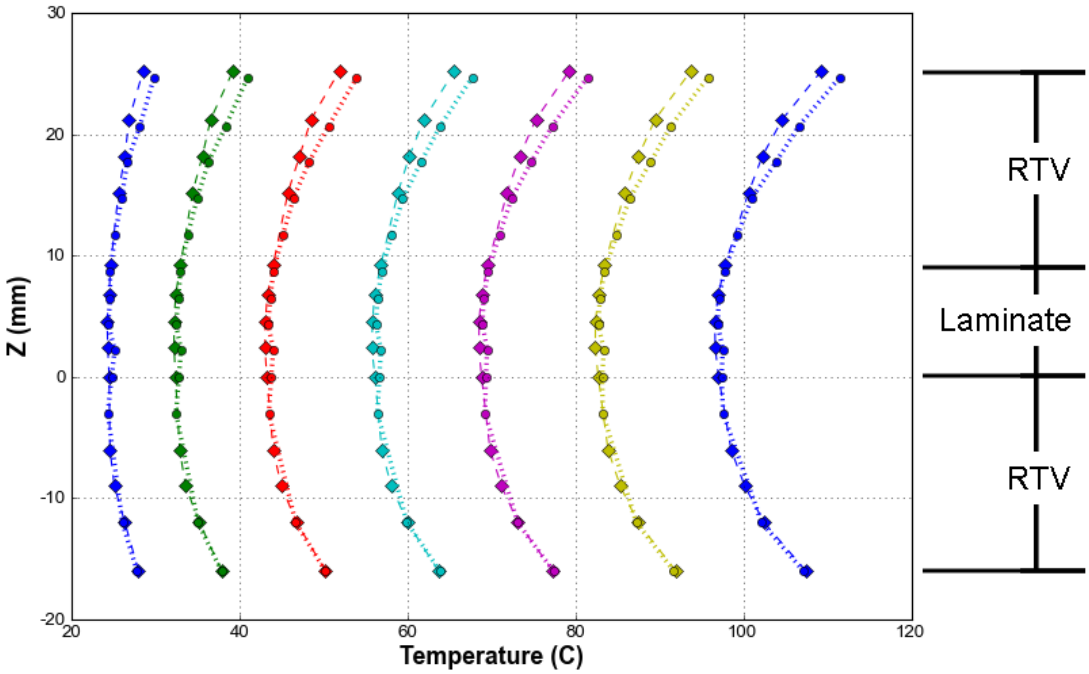

Figure 4-26: Through-thickness profile for P700T/2510 tape (dashed line with diamond markers) and fabric (dotted line with circle markers) at 15 minute intervals

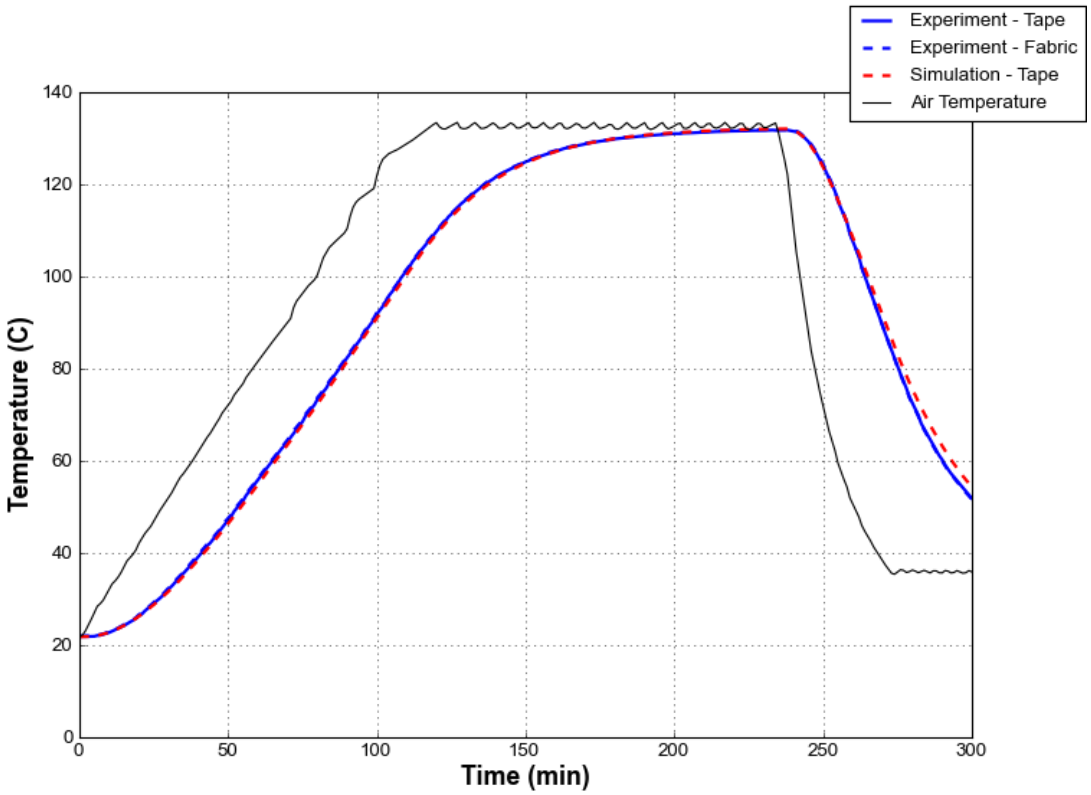

Figure 4-27: Time vs. temperature profile for fully cured tape, fabric, and simulated P700T/2510 laminates.

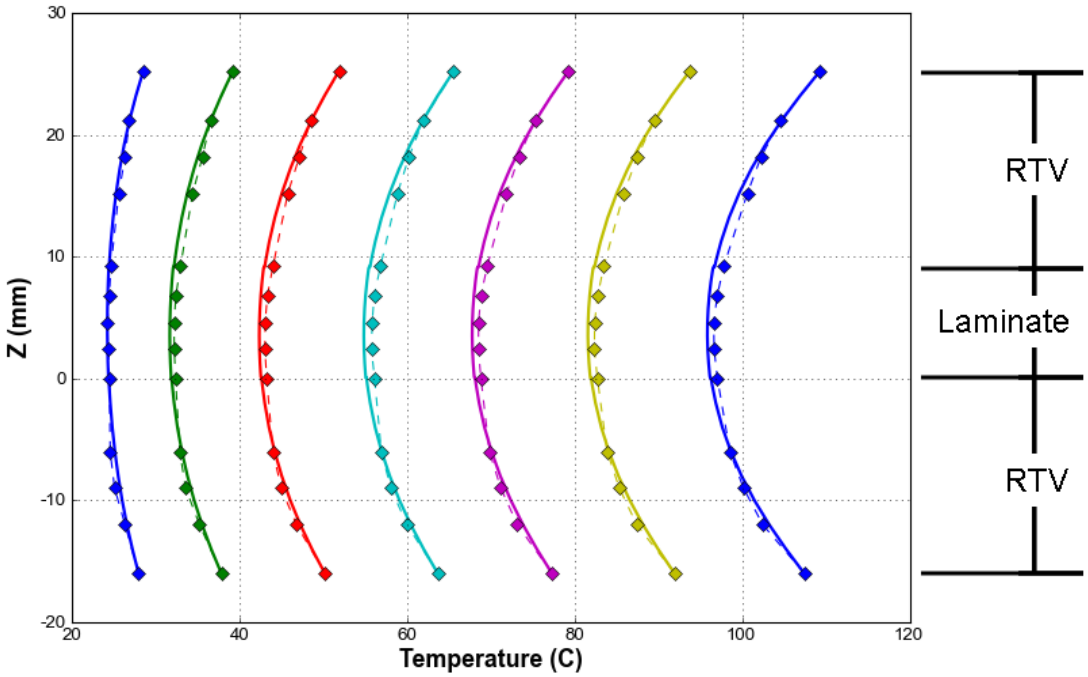

Figure 4-28: Through-thickness profiles for P700T/2510 tape (dashed line with diamond markers) and 1-D simulation (solid line).

4.2.4.2 Uncured

Both T700/2510 laminates were highly reactive; the peak temperature exceeded the hold temperature by 35.0 °C for the tape and 50.0 °C for the fabric. Through-thickness profiles at the peak of the reaction showed 7.7 °C and 13.3 °C gradients in the tape and fabric laminates, respectively, Figure 4-29. The gradients were over a distance of only 4.0 mm, and developed because the rate of internal heat generation was much higher than the rate at which heat can diffuse through the laminate. Such a large variation in temperature meant that the quality of the cure, and therefore the laminate properties, were also variable through the thickness.

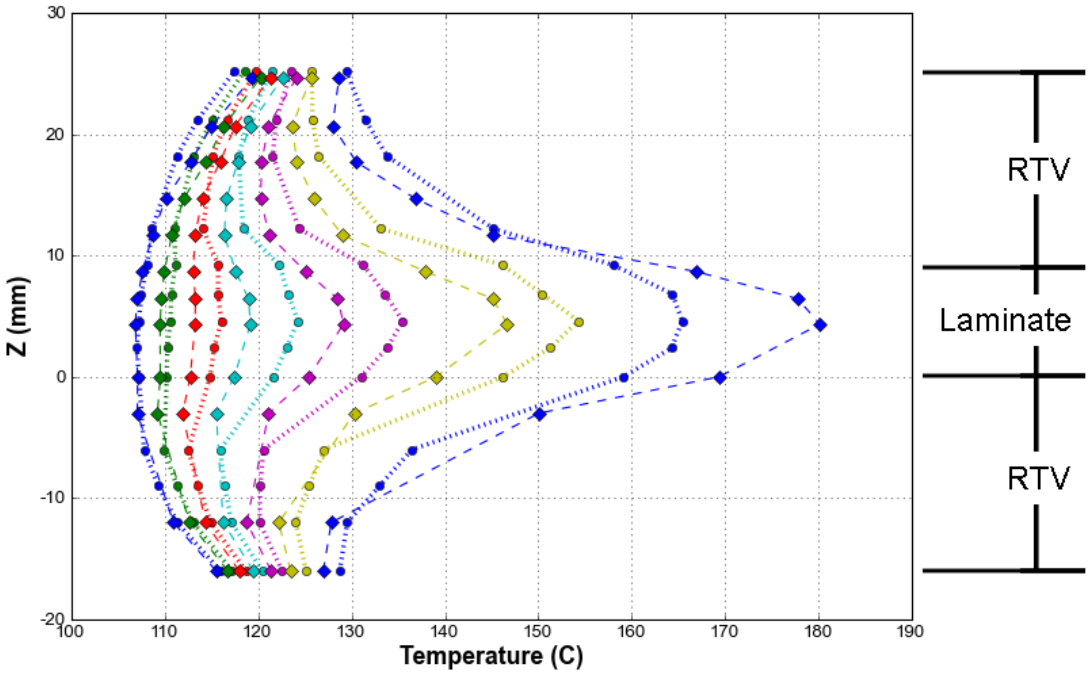

Figure 4-29: Cure reaction of P700T/2510 tape (dotted line with circle markers) and fabric (dashed lines with diamonds) at 2 minute intervals. The green contours show the reaction in the tape starting before the fabric, the gradient in the tape decreases while the fabric stays the same.

As discussed, the material model was generated using the tape form of the prepreg (Convergent Manufacturing Technologies Inc., 2010). Through-thickness profiles of the curing experimental and simulated tape showed excellent agreement until the peak of the reaction, Figure 4-30. The predicted timing of the start of the reaction, and the development of the reaction prediction was accurate for the tape model, Figure 4-31. Although the predicted peak temperature was off by 13.0 °C, the error would not be of concern in practical applications. As with the AS4/8552 laminates in Section 4.2.2.2, temperature excursions more than 5.0 °C above the hold temperature are unacceptable and the simulated prediction was accurate to that point.

A fabric model was created by changing the V_f of the tape model to the calculated V_f of the experimental fabric laminate. The cure reaction of the modified model started 5 minutes earlier than the experiment, but developed at the same rate, Figure 4-31. A new material cannot, therefore, be created by changing V_fs. The thermal response of the woven fabric differs enough from the thermal response of [0/90]s unidirectional laminate that the fabric requires its own material model. A composite's thermochemical response is more than the sum of the fiber and matrix properties; coupling from the micromechanics of different fiber sizing, bundling of the fiber tows, weave architecture, or resin chemistry can also affect the thermal response of the laminate. The tests with MTM45-1 in Section 4.2.1 were conducted with a 5-harness-satin fabric, and showed excellent agreement because the model was generated from the fabric

prepreg. The P700T/2510 model was generated from the tape, and had good agreement with the experimental tape laminate, but not the fabric laminate. To prevent a model from being improperly adapted to multiple material forms, proper model validation is key.

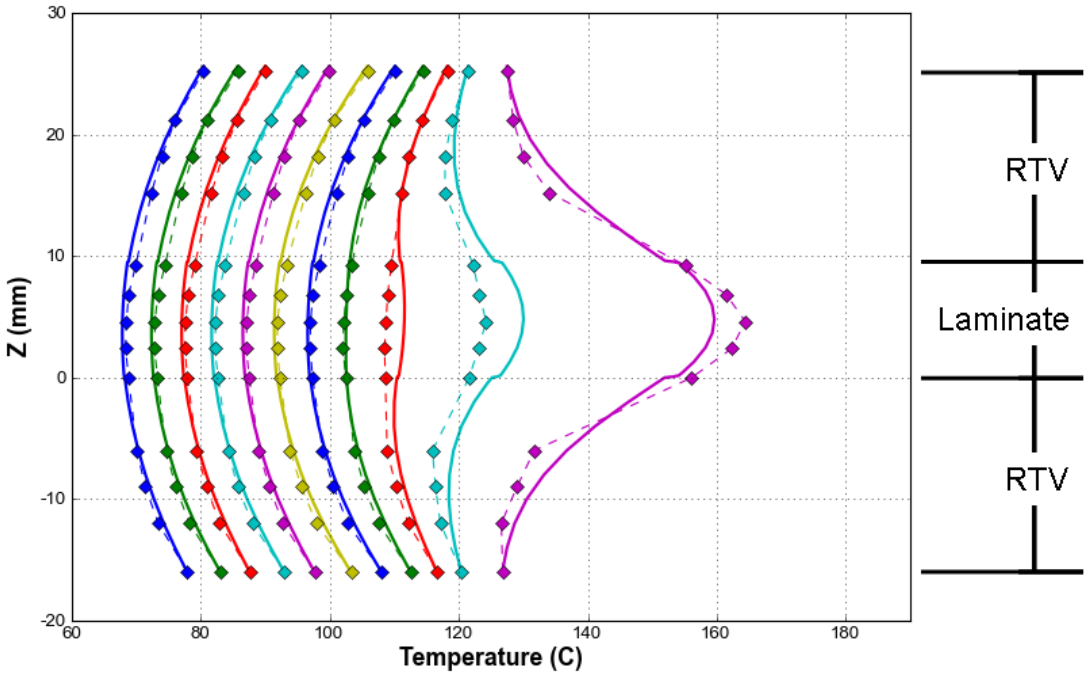

Figure 4-30: Through-thickness profiles for P700T/2510 tape (dashed lines with diamonds) and 1-D simulation (solid lines) at 2 minute intervals. The simulation reaction starts 2 minutes earlier than the experiment at 115 °C.

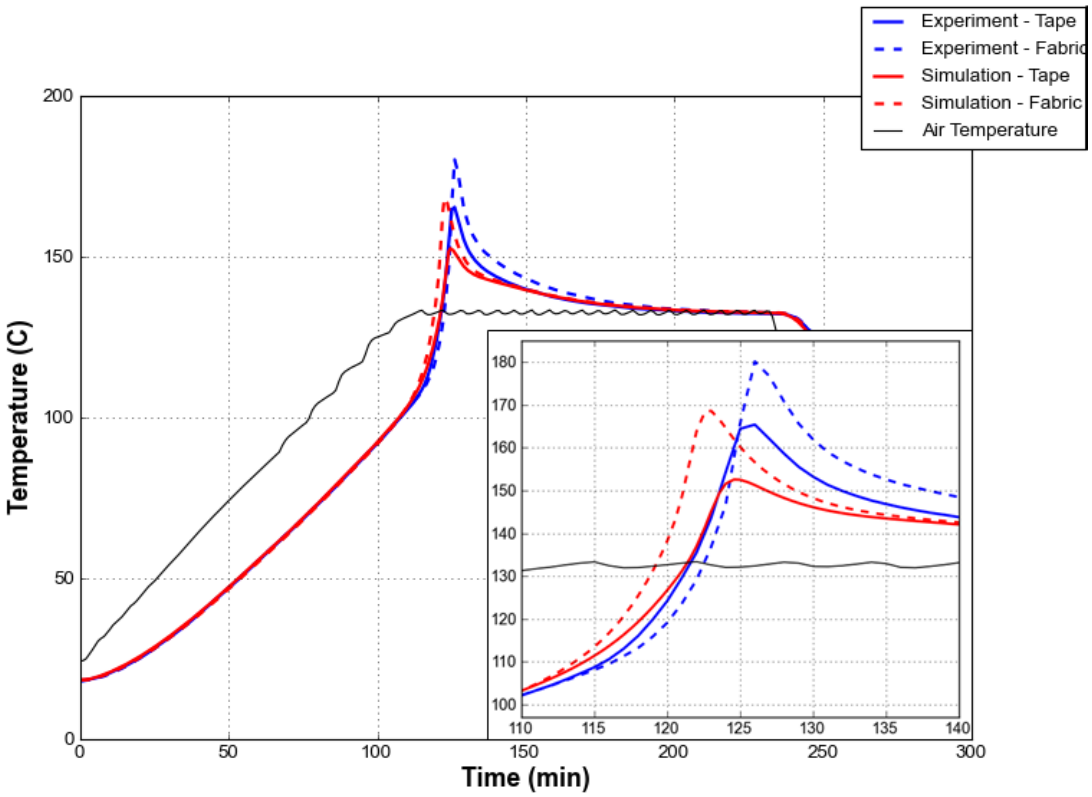

Figure 4-31: Time vs. temperature profiles for P700T/2510 laminates. The simulation reaction can be seen starting earlier than the experiment, and the simulation missed the exotherm peak temperature. Modeling the fabric by changing V_f increased the peak exotherm, but also causes the reaction start earlier and lead the experimental laminate.

4.3 Summary

The developed methodology provided a DSC *independent* method to validate thermochemical models. Five models covering four prepreg systems were tested. The use of instrumented rubber bricks provided a robust method to confirm that the boundary conditions were properly modeled, and that heat transfer in the material stack was 1-D. Without the calibrated thermal gradient in the bricks, it would not have been possible to trace the lag at the bottom of the laminate in Section 4.2.3 to the improperly compacted breather. Uncertainty in the simulation was further reduced by confirming the inert properties of the composite independently of the curing properties by repeating the thermal cycle on the fully cured laminate.

It was possible to obtain consistent agreement of 2.0 °C or better with the better thermochemical models.

At a minimum, through-thickness and time vs. temperature profiles of the cured and uncured laminates should be generated from experimental data.

- Through-thickness profiles for:

    - accuracy of modeled thermal boundaries
    - through-thickness thermal conductivities
    - the start and development of the cure reaction
    - resin flow and evolution of V_f
- Time vs. temperature plots for:
    - timing and magnitude of the exotherm
    - the start and development of the cure reaction
    - temperature and pressure dependencies of thermal properties
    - specific heat and thermal conductivity induced lead and lag

The developed methodology has been demonstrated to work for:

- fabric and tape fiber architectures
- out-of-autoclave prepregs requiring a post-cure
- pressurized and unpressurized cure cycles
- slow (0.5 °C/min) and fast (5.0 °C/min) ramp rates
- medium (120.0 °C) and high (180.0 °C) temperature cures
- thin (<4.0 mm) and thick (>18.0 mm) laminates

Additional points for the developed thermochemical model validation methodology:

- Thermal histories are highly sensitive to V_f. However, a 1-D simulation can be an accurate approximation up to V_fs 10% above nominal if the resin bleed was at the edges of the laminates in this work. The actual V_f cannot be treated as an indicator of the total amount of resin generating heat, as a significant amount of the heat generated by the bled resin can be transferred to the laminate due to high in-plane thermal conductivities.
- Matching the peak temperature and exotherm timing does not constitute complete model validation. The entire time vs. temperature profile needs to be checked for agreement with the experimental data.
- Properly insulating the edges of the material stack is critical because the high in-plane thermal conductivity magnifies the effects of 2-D heat flow.

- A poor model fit beyond 5.0 °C above the hold temperature does not necessarily mean that the model is unusable. As long as the model is accurate in the range of the processing window, it can be of value since a goal of the model is to prevent temperature excursions during processing.

5 Autoclave Characterization and Heat Transfer Coefficient Measurement

Understanding the capabilities and limitations of a specific autoclave is critical to effectively process large and complicated parts. In this chapter, two related autoclave performance parameters are observed and measured: the airflow patterns, and the associated convective heat transfer coefficients. Airflow is observed with cameras for visual monitoring and CFD for simulation. HTC is quantified using simple calorimeters. The UBC autoclave environment is highly turbulent, has poorly oriented airflow, and unevenly distributed HTCs.

5.1 Visual Monitoring

5.1.1 Methods

Video recording of the activity inside the autoclave has little to no uncertainty and provides instantaneous feedback regarding relative directions and magnitudes of airflow. A video camera system that functions at ambient temperatures and pressures was assembled from readily available, inexpensive, off-the-shelf components. Autoclave strain gauge wiring was used as a USB extension for a USB camera, and a wireless network was set up for a second camera, Figure 5-1 and Figure 5-2.

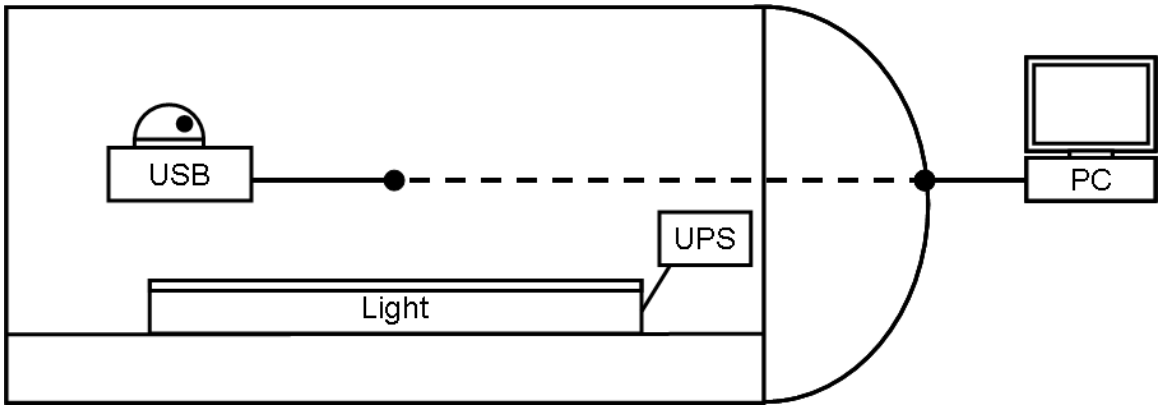

Figure 5-1: USB camera configuration showing the USB cabling routed through the autoclave wiring. Note the power supply does not power the camera because the camera is powered over the USB cable.

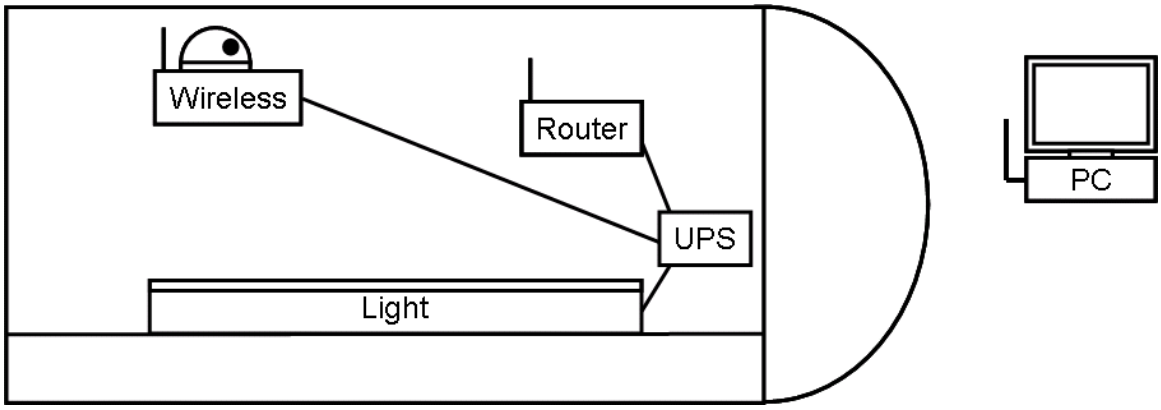

Figure 5-2: Wireless camera configuration showing the power and network connections required inside the autoclave. The computer must be able to receive wireless signals.

Tufts of yarn were used to study the airflow pattern of the free-stream airflow and the airflow pattern on and around a tool surface. For free-stream airflow, the tufts were tied to another length of yarn pulled taut across the open space. The angle of displacement of each tuft was compared to other tufts to estimate the relative magnitude of airflow around a specific tuft. As Figure 5-3 shows, the tuft was vertical when there was no flow and then displaced a specific amount under flow. Only estimates of the velocity were made because the airflow was not normal to the tuft at every location, and if the flow was at a high velocity in a different direction it displaced the same amount as if it were a lower flow in the normal direction. Arranging the tufts in a grid on the tool surface, while moving the tool to different locations in the autoclave, showed how positioning changes affect the airflow on the tool.

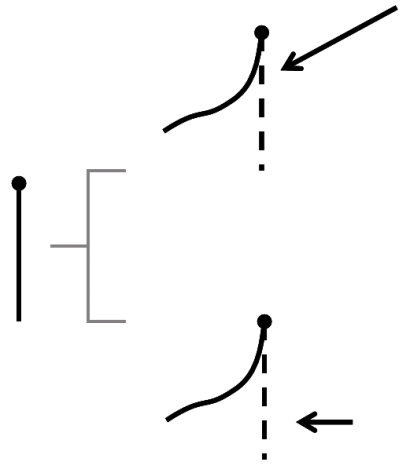

Figure 5-3. Comparison of tuft displacements under flow. Tufts are useful for qualitative observations, but note how the same tuft response can be seen with different flow conditions.

For this work, the following components were used:

Light: 48 Super Bright LED Under-Hood Worklight - Product Number 37-9434

Cameras: Logitech QuickCam Orbit AF USB Camera (Logitech, 2010)

TRENDnet TV-IP410W SecurView Wireless Camera (TRENDnet, 2010)

Network: D-Link WBR-2310 Wireless Router

Power: APC Back-UPS ES USB 650VA Uninterrupted Power Supply (UPS) (American Power Conversion Corp., 2010)

Manual autoclave controls were used to turn on the circulation fan. Temperatures did not exceed 35.0 °C and pressure remained at one atmosphere in order to prevent damage to the equipment (TRENDnet, 2010). The activity inside the autoclave chamber was monitored and recorded to a PC outside of the autoclave.

5.1.2 Results and Discussion

5.1.2.1 Empty Autoclave

Multiple images from video recordings of the tufts under flow were stitched together, Figure 5-4. Maximum velocity was at the top, where the angle of deflection of the tuft was highest. Velocity decreased as the distance from the top of the chamber increased. Near the floor of the autoclave, the tufts at the bottom showed reversed airflow in the 0.5 m nearest the door, where it then transitioned to flow to the back of the autoclave. Airflow in the autoclave was poorly oriented and highly turbulent, nothing like the highly oriented plug-flow assumed to be present during cure.

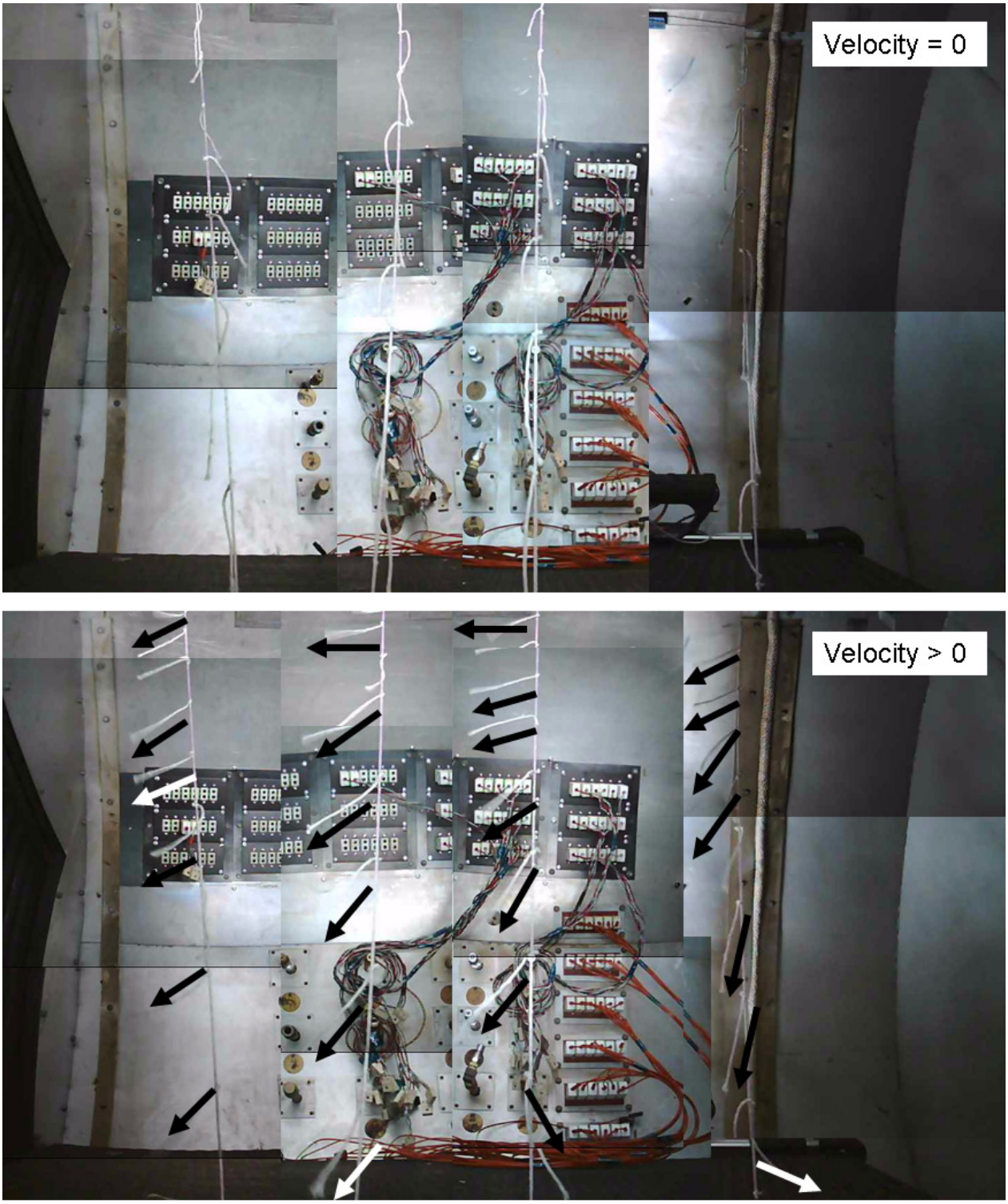

Figure 5-4: Response of tufts in the empty autoclave before and during flow. The autoclave door is to the right.

5.1.2.2 Tool Surface

A grid of tufts was used on the surface of a tool to monitor the airflow over the tool, Figure 5-5. The tool was monitored in four different positions inside the autoclave, Figure 5-6. Video was

recorded with the tool centered in the autoclave, aligned with the flow (1), offset toward the wall (2), angled in the flow (3), and perpendicular to the flow (4).

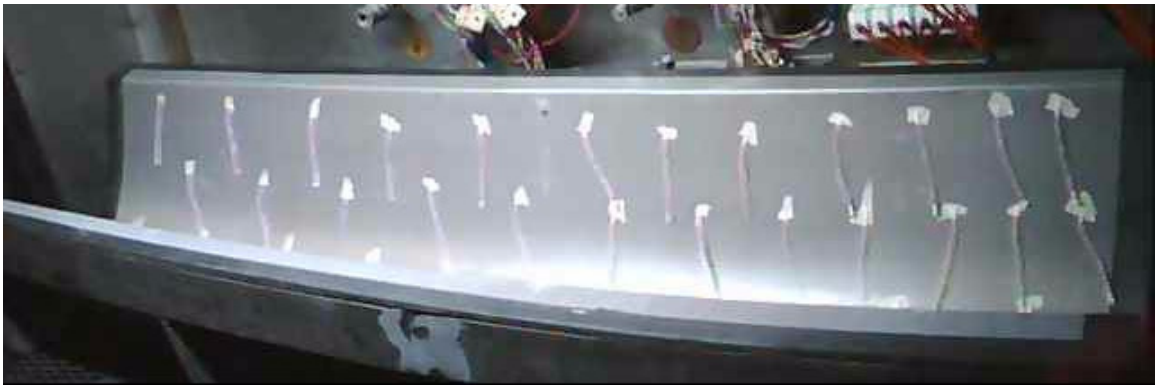

Figure 5-5: Tool with grid of tufts used to monitor airflow over the surface under different positions in the autoclave.

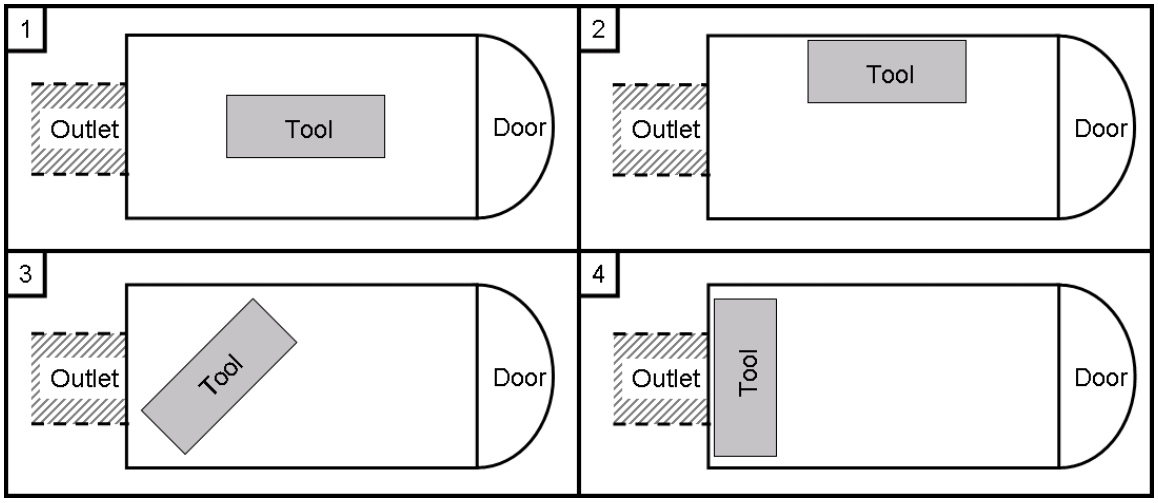

Figure 5-6: Top-down view of tool placement. Centered and aligned with flow (1); offset toward the wall (2); angled in the flow (3); perpendicular flow (4)

Video results from the tool surface qualitatively showed the effects of the poorly oriented and turbulent airflow on a tool. Although the tool was aligned with the airflow and centered in the autoclave, airflow over the tool was not uniform, Figure 5-7. 0.15 m from the front of the tool, the air flowed from the top and split into flow towards the font and the back of the autoclave. Airflow was stagnant where the flow diverged, but the displacement angle of the other tufts increased with increasing distance from the diverging airflow. The magnitude of the air velocity increased as the air was funneled through the tool.

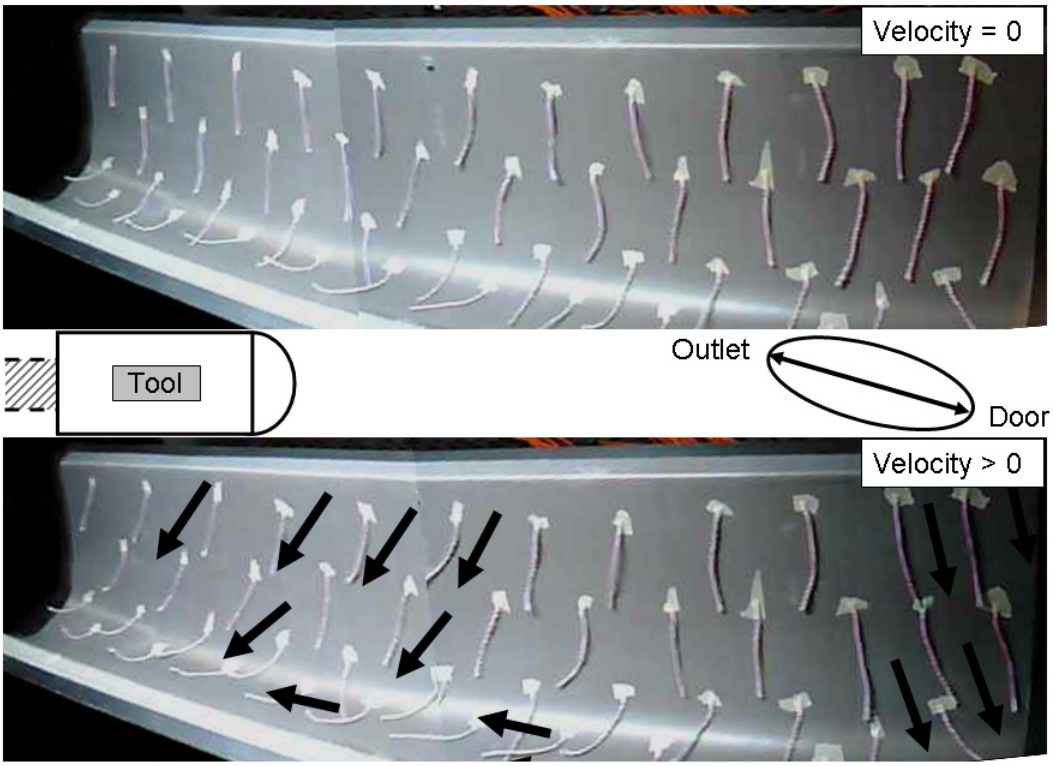

Figure 5-7. Response of tufts on centered tool. Airflow splits and reverses in the area near the door.

Shifting the tool 0.25m completely changed the airflow over the tool, Figure 5-8. The tufts closest to the back of the autoclave showed that the airflow was reversed on the entire tool surface. At the sides of the autoclave chamber, the airflow bounced off of the back wall and reversed direction. The areas of stagnant air at the front of the tool near the door were due to the presence of wiring and vacuum ports.

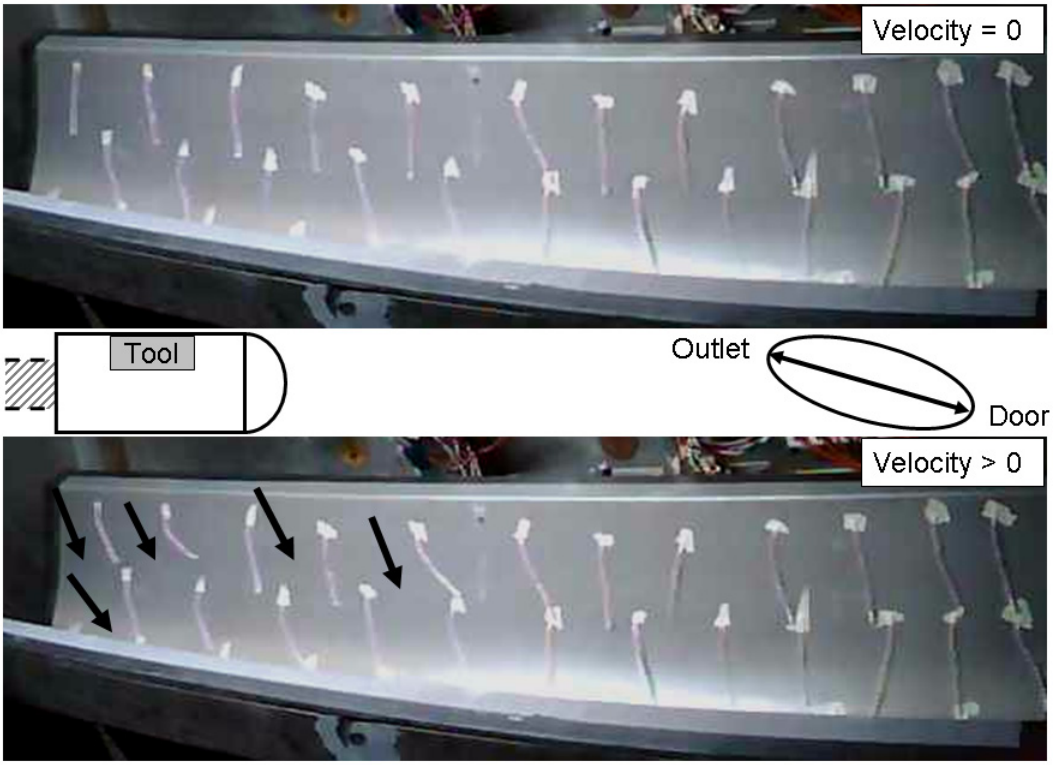

Figure 5-8. Response of tufts on offset tool

Angling the tool at 45 degrees caused inconsistent and increasingly turbulent airflow over the tool surface, Figure 5-9. Airflow over the middle of the tool, in line with the center of the autoclave, was the highest and most turbulent. Airflow on the end of the tool nearest the outlet was reversed, likely caused by the airflow that bounced off the back wall being channeled by the tool geometry. The airflow on the tool diverged to the right of center and converged to the left of center.

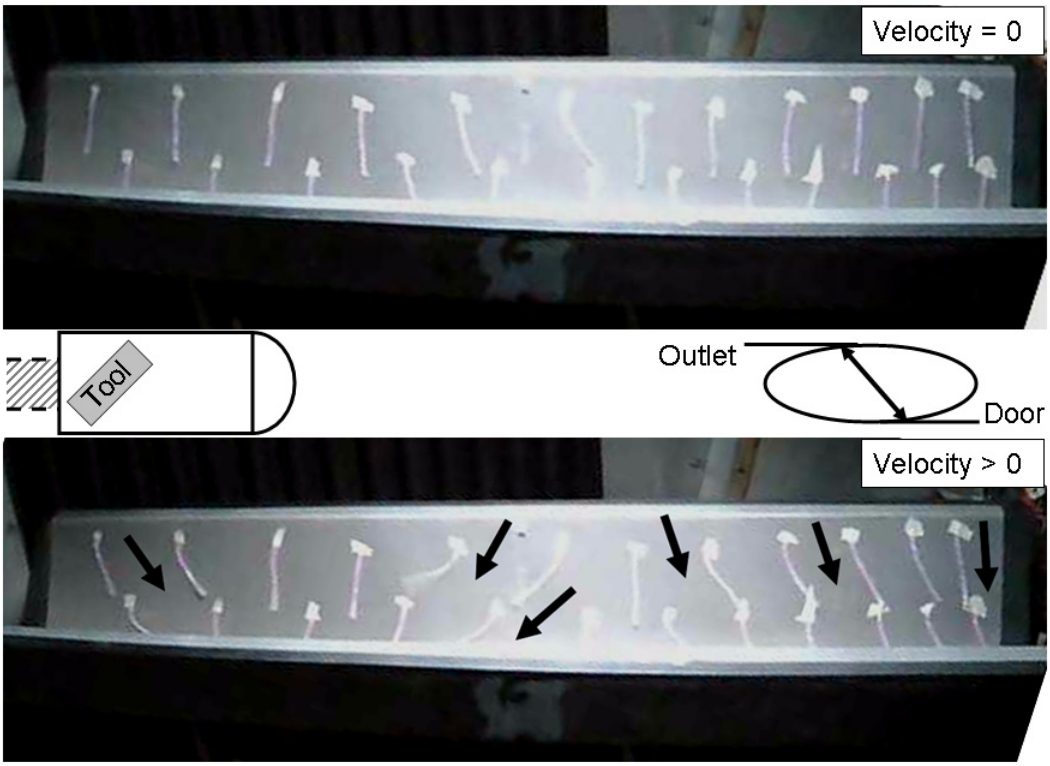

Figure 5-9: Response of tufts on angled tool

When perpendicular to the airflow the tool showed highly turbulent flow that diverged along the center of the tool. The airflow converged again on the left half of the tool, but the airflow on both outer edges of the tool was nearly stagnant in Figure 5-10.

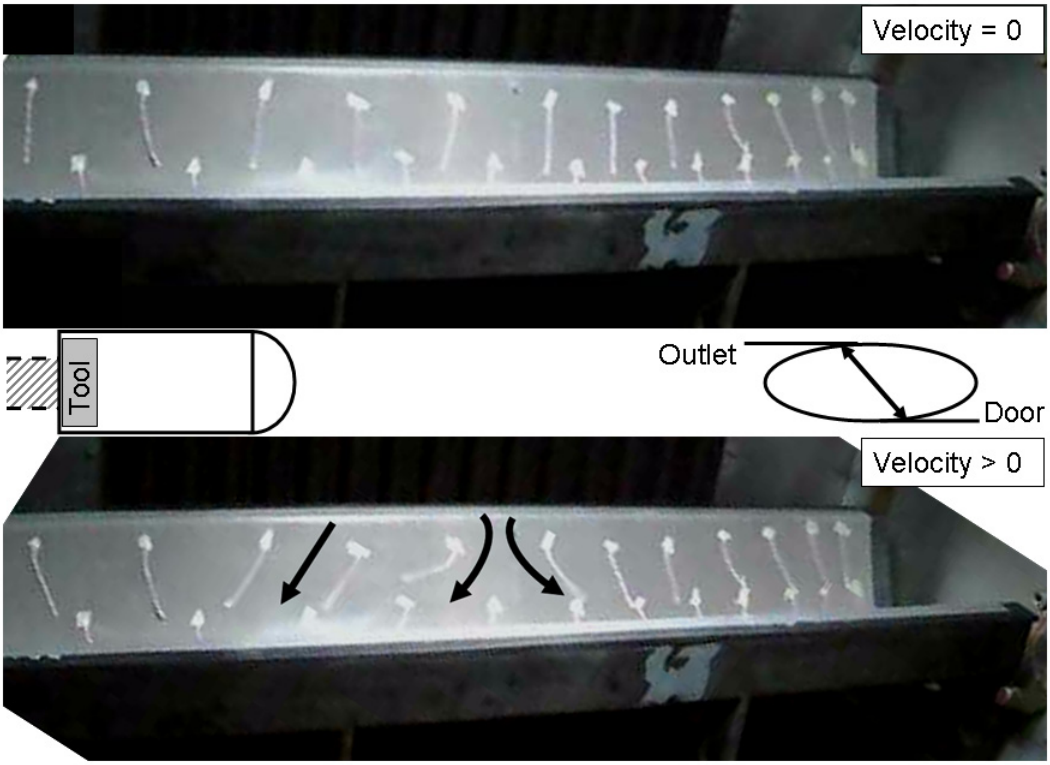

Figure 5-10: Response of tufts on perpendicular tool

5.2 Simulation

CFD simulations were conducted using the ANSYS FLUENT software package. Analysis of the empty autoclave was performed by members of the Department of Materials Engineering at The University of British Columbia (Maijer & Poursartip, 2005).

5.2.1 Simulation

CFD results for the empty autoclave showed the same airflow pattern as the visual monitoring, Figure 5-11. Air velocities decreased as the distance from the top of the chamber increased, and there was reversed airflow along the bottom floor of the autoclave. A low velocity, or nearly stagnant, vortex developed 0.25m from the door, which corresponded with the stagnant response of the tufts near the door. The recorded images and their corresponding location on the CFD result agree, Figure 5-12. Visual analysis was a quick and intuitive substitute and/or qualitative validation of CFD results.

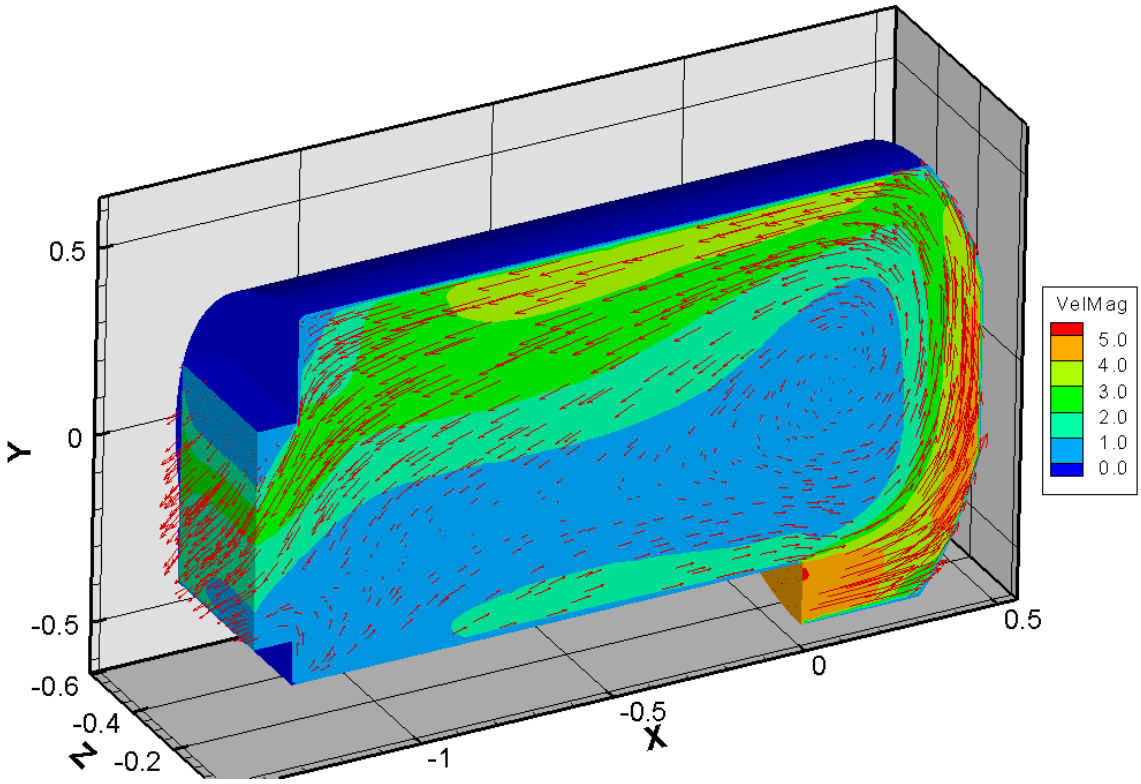

Figure 5-11: CFD results for the empty autoclave (Maijer & Poursartip, 2005)**.**

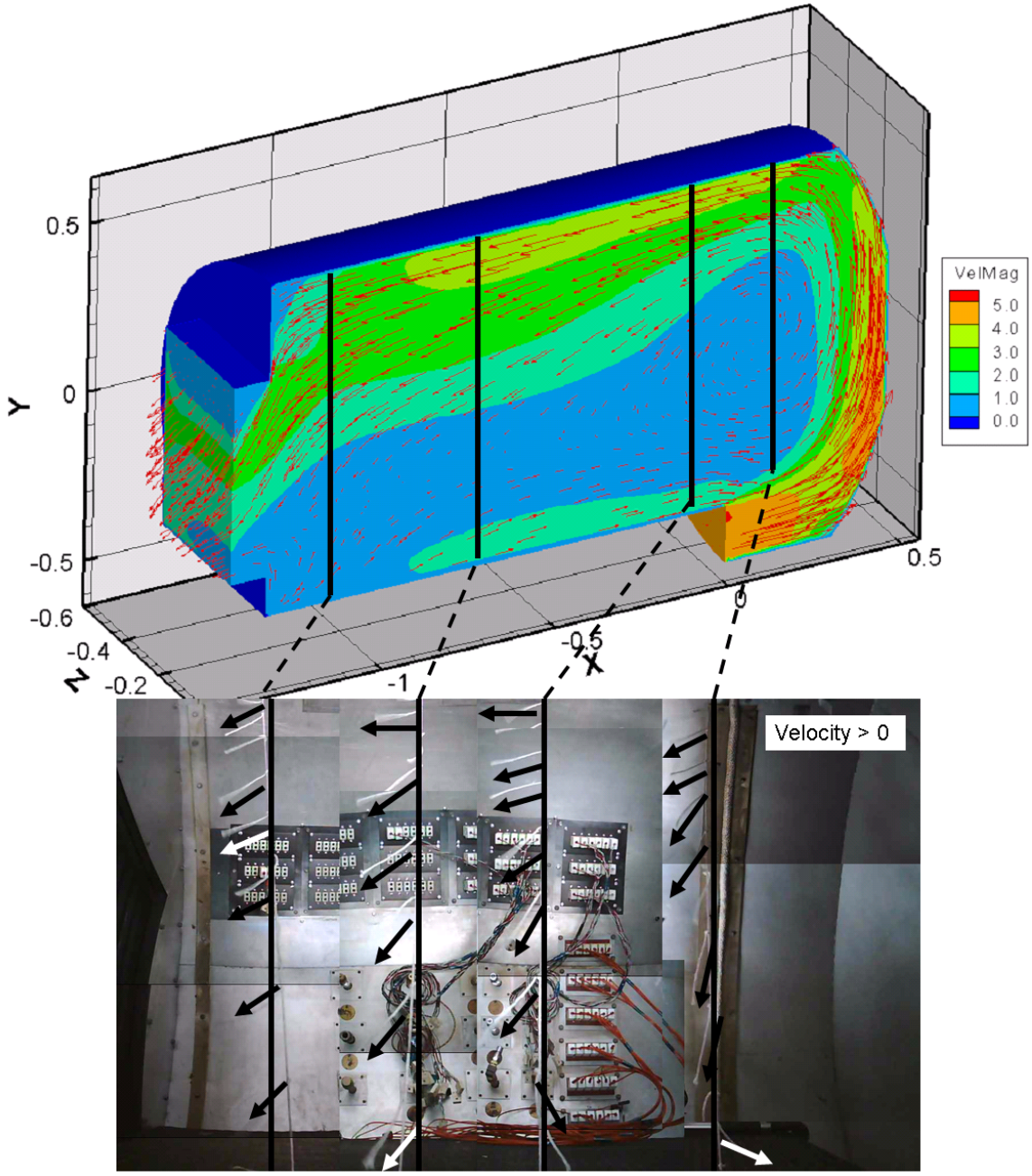

Figure 5-12: Response of tufts compared to CFD results for empty autoclave

5.3 Heat Transfer Coefficient Measurement

HTCs increase with increasing air velocities and vice-versa; HTCs can therefore be used to map out relative air velocities in the autoclave. Two types of calorimeters were used to measure HTCs at various locations throughout the autoclave: lumped-mass, and thermal gradient calorimeters.

5.3.1.1 Lumped-mass Calorimeter

The lumped-mass calorimeter was the same steel rod supported and capped by a piece of low thermal conductivity material such as wood or ceramic as used in 3.1.1, Figure 5-13. The

thermal mass, 3.65 MJ/m^{3}K, ensured a measurable lag between the sample surface and the fluid temperatures.

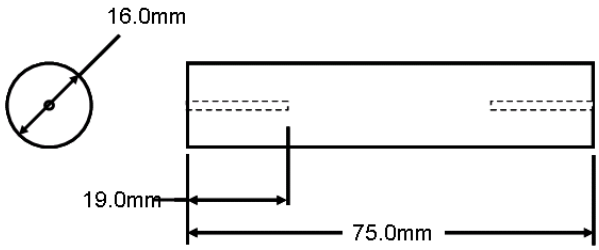

Figure 5-13: Dimensions of the steel rod calorimeter. Thermocouples are placed in the 19.0 mm deep holes.

An additional TC was placed near the calorimeter during the cycle to measure the local air temperature. Temperature data from the rod after a thermal cycle was used to back-calculate HTCs using Equation (2-15):

$$h = \frac{\rho C_p V \Delta T}{A \Delta T_s \Delta t}$$

5.3.1.1.1 Methods

Lumped-mass calorimeters were placed throughout the empty autoclave to measure the local HTCs, Figure 5-14. The locations were based on the CFD results and engineering judgment. Three air pressures, 0, 50, and 100 psig, were used to provide three distinct HTC values at each location. The cure cycle was:

- pressurize to 50 psig
- heat at 5.0 °C/minute to 100.0 °C
- hold for 35 minutes
- pressurize to 100 psig
- heat at 5.0 °C/minute to 180.0 °C
- hold for 60 minutes
- pressurize to 0 psig
- cool at 5.0 °C/minute to 20.0 °C

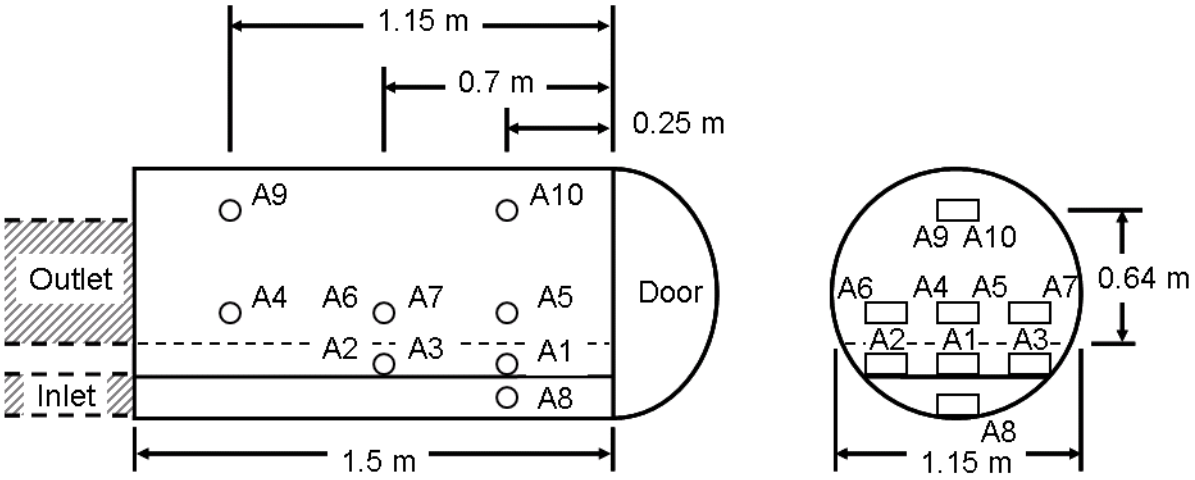

Figure 5-14: Calorimeter locations distributed through out the empty autoclave.

HTCs from the lumped-mass calorimeters were back-calculated using temperature data and Equation (2-15). The UBC autoclave temperature history oscillated during linear ramps and holds, especially at high ramp rates, Figure 5-15. A discrete, objective value for the air temperature was needed for consistent calculations, and was calculated by fitting lines to the air temperature and rod temperature at a steady-state temperature ramp, Figure 5-16. The offset of the two lines was the constant ΔT_s for Equation (2-15), and the back-calculated value was the HTC at that location during that portion of the cycle.

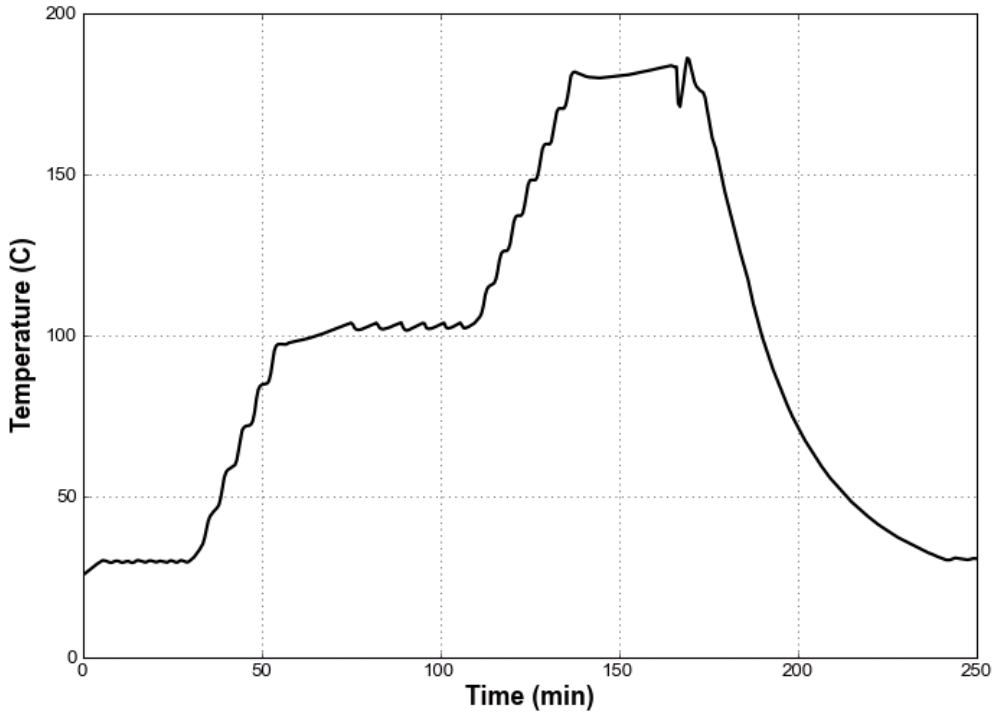

Figure 5-15: Oscillating air temperature typical of a UBC autoclave cycle.

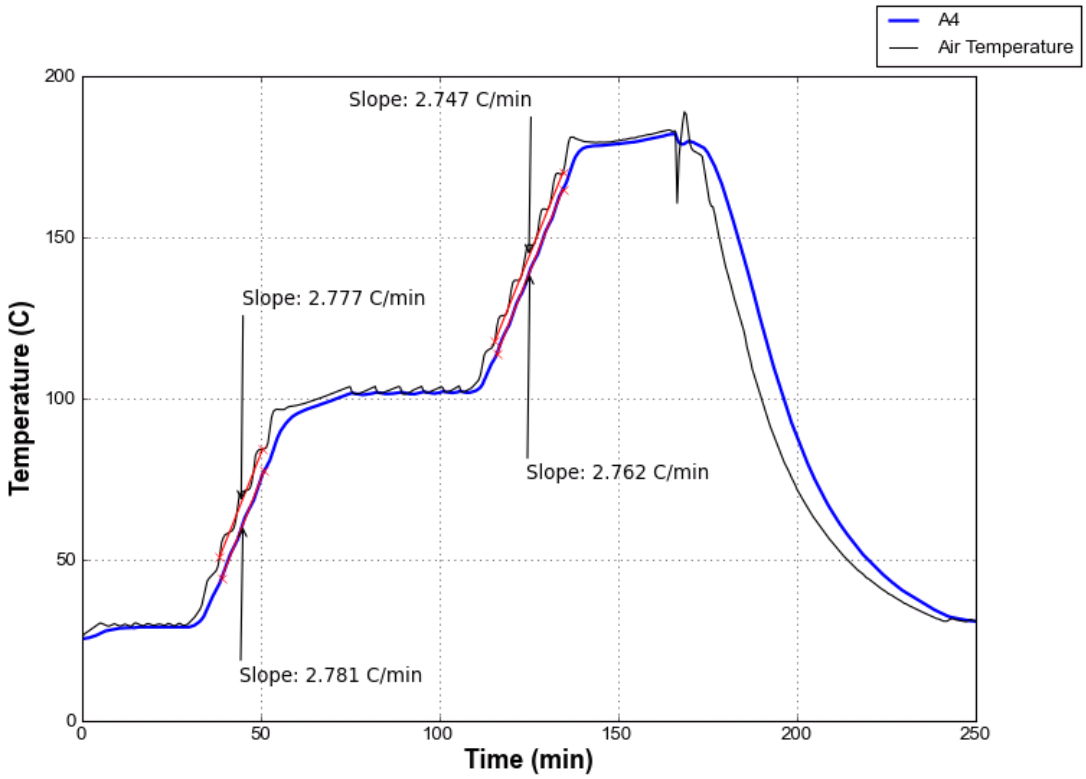

Figure 5-16: Steady-state slopes for air and calorimeter temperatures

5.3.1.1.2 Results and Discussion

Table 5-1 is the back-calculated HTCs from each calorimeter at the locations shown in Figure 5-17. The CFD and visual monitoring showed that airflow, and therefore heat transfer, were highest at the air inlet and top of the chamber. The corresponding HTCs from Calorimeters A8, A9 and A10, were the highest as well, Figure 5-18. Airflow below the support screen was shown by the visual monitoring and CFD to be much lower, and this was again confirmed by the lower HTCs of Calorimeters A1, A2, and A3. Variations of 30-60 W/m^2K occur over distances of less than 0.5 m, and the variation was not limited to the high velocity, highly turbulent areas around A8, A9, and A10. A4 and A5 were in low velocity and stable airflows and differed from each other by 37 W/m^2K. Thus, even small and simple parts can experience significant variation in heat transfer over their surfaces.

Table 5-1: Back-calculated HTCs from lumped-mass calorimeters in empty autoclave

	HTC (W/m^2K)		
Calorimeter	0 psig 40C	50 psig 60 C	90 psig 140C
A1	70	123	149
A2	89	163	186
A3	89	163	177
A4	92	157	185
A5	78	120	168
A6	100	174	234
A7	92	167	202
A8	97	208	323
A9	125	184	288
A10	127	186	265

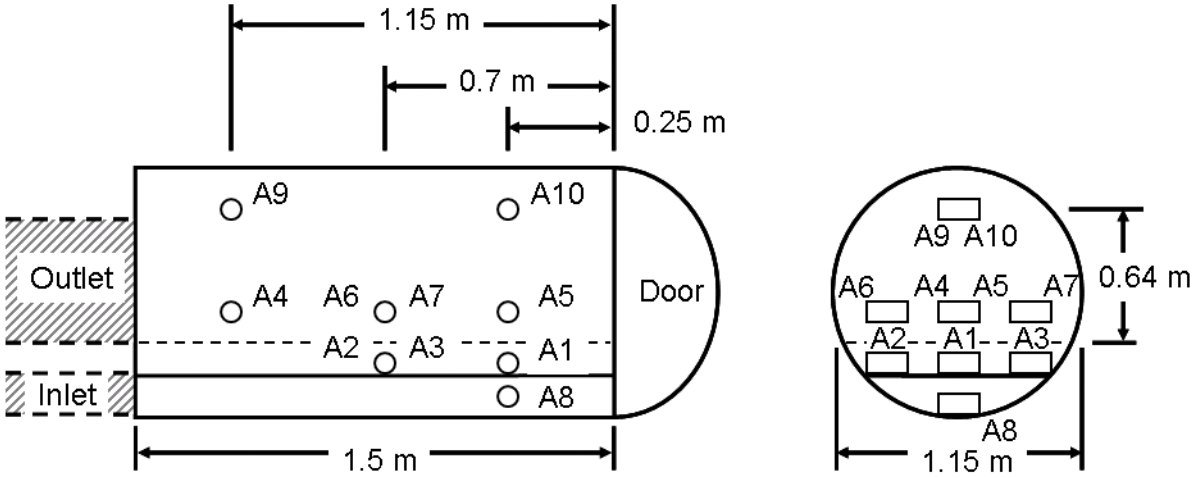

Figure 5-17: Calorimeter locations for autoclave HTC analysis.

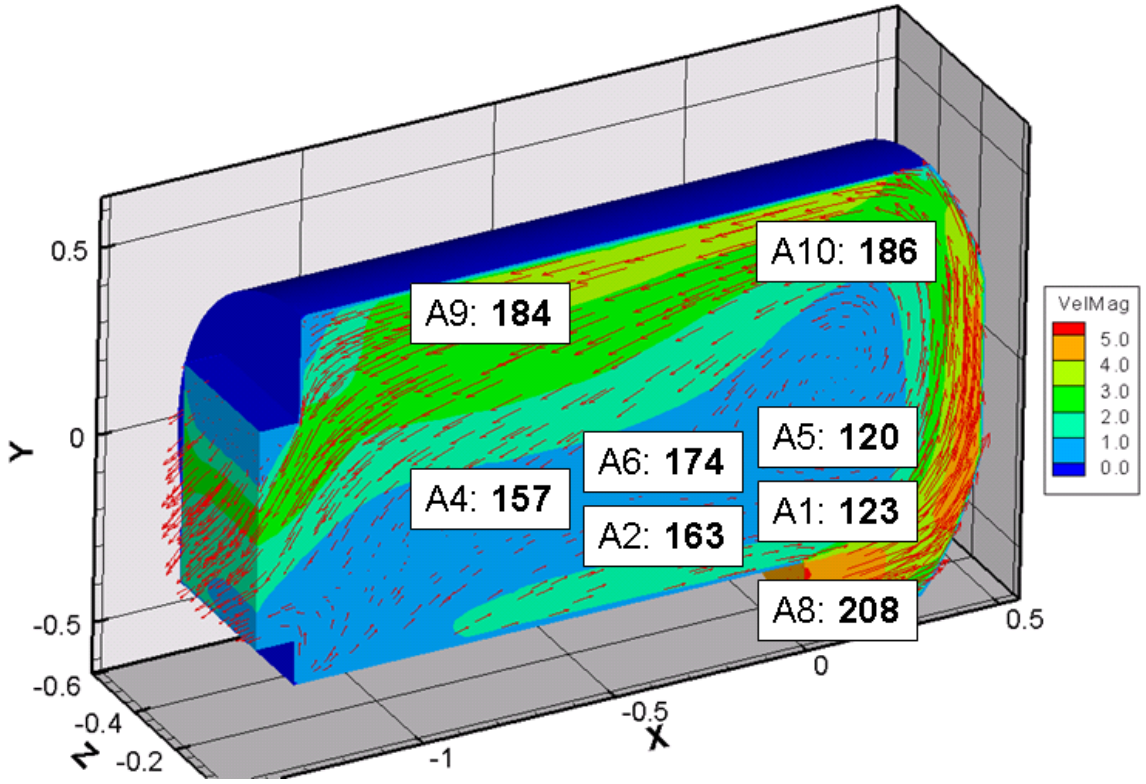

Figure 5-18: HTC distribution at 60 °C and 50 psig overlaid on CFD results

5.3.1.1.2.1 Temperature and Pressure Scaling

The temperature and pressure scaling correlation from Equation (2-13) was used for the ratios of the initial and instantaneous temperatures and pressures to create the theoretical HTC scaling profile, Figure 5-19, using Equation (5-1):

$$\frac{\left(\frac{P}{T}\right)^{\frac{4}{5}}}{\left(\frac{P_0}{T_0}\right)^{\frac{4}{5}}} \tag{5-1}$$

The experimental HTC scaling profile was created by normalizing the initial HTC to 1.0 and evaluating the ratios of the initial and instantaneous back-calculated HTCs using Equation (5-2):

$$\frac{h}{h_0} \tag{5-2}$$

Figure 5-19 shows that the autoclave HTC did not scale with the theoretical pressure/temperature relationship. When the autoclave was pressurized the actual HTC was below the theoretical scaling, but when it was not pressurized the actual HTC was above the theoretical scaling.

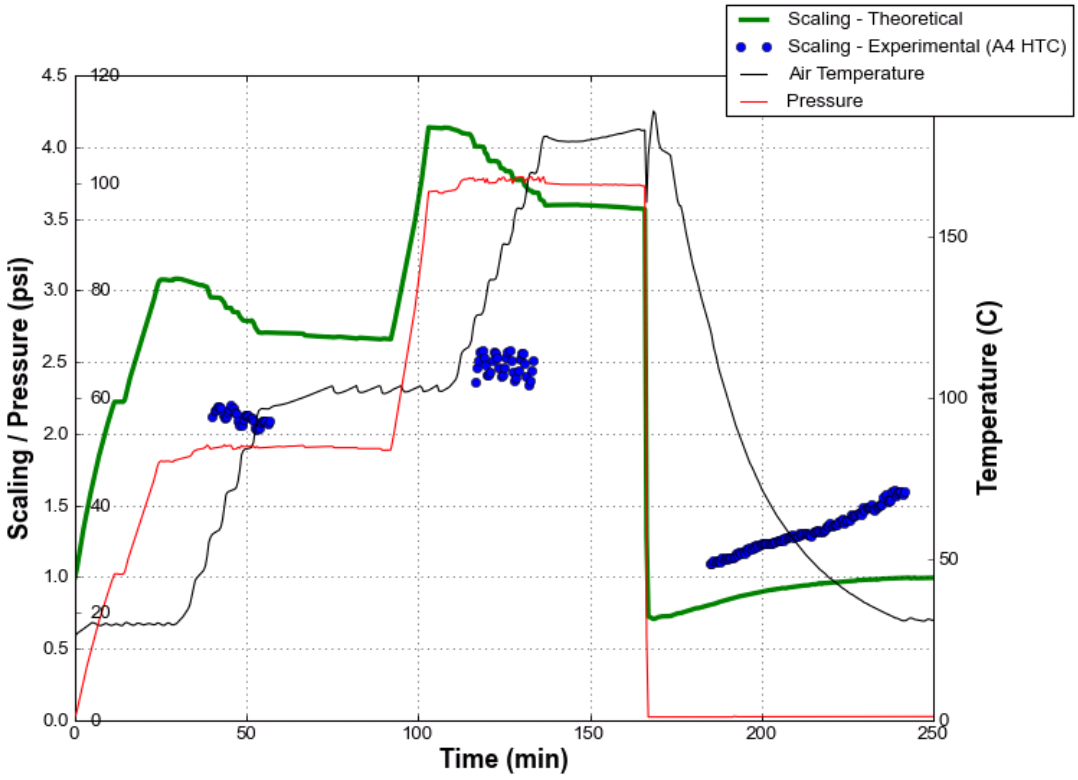

Figure 5-19: Theoretical and actual HTC scaling with temperature and pressure. At t = 0, HTC is normalized to 1. Data during temperature holds is omitted for clarity due to the high variable that results from a small ΔTs.

The source of the scaling error was likely the mechanical limitations of the autoclave. Using the Ideal Gas Law, the ambient air density increased ~ 6 times at 100 psig and 180 °C. If a mass-flow limit of the circulation fan was reached, the volume flow would decrease as the fluid density continued to increase. For example, the first pressurization cycle doubled the HTC, but the second pressurization cycle increased the HTC by less than 15%. Constant air velocity is assumed in the correlation of Equation (2-13), so the decreased volume flow, which decreased the air velocity, lowered the HTC below the theoretical value.

5.3.1.2 Thermal Gradient Calorimeter

5.3.1.2.1 Methods

An instrumented steel plate was used as a thermal gradient calorimeter, Figure 5-20. Equation (2-16), repeated below, was used to back-calculate the HTC from the through-thickness thermal gradients that developed in the plate::

$$h = \frac{\sum_{i=1}^{n} \rho C_p L \Delta T_i \Delta \zeta_i}{\Delta T_s \Delta t}$$

where i is the measurement location through the thickness of the material; ρ is the density of the calorimeter material; C_p is the specific heat of the calorimeter material; L is the half-thickness of the plate; ΔT_i is the change in calorimeter temperature; ζ is a non-dimensional thickness coordinate where ζ = -1.0 at the bottom surface, ζ = 0 at the adiabatic line, and ζ = 1.0 at the top surface; ΔT_s is the temperature difference between the calorimeter surface and surrounding fluid; and Δt is the time interval. Asymmetry in the thermal gradient of the plate was used to calculate the different top and bottom HTCs of the plate.

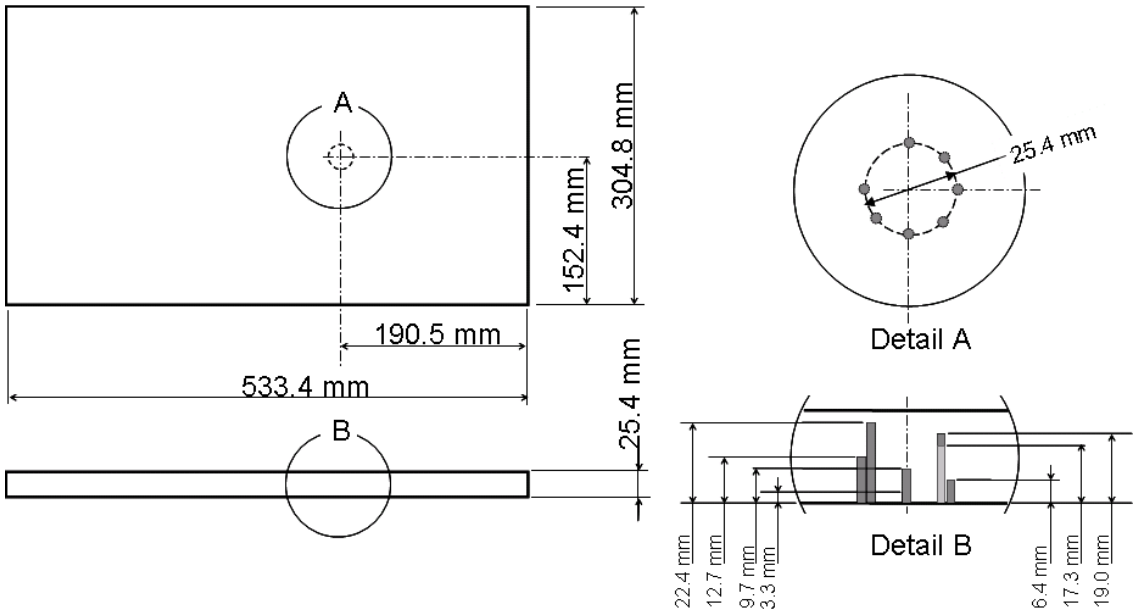

Figure 5-20: Thermal gradient calorimeter dimensions. Thermocouples are located in the group of holes shown in details A and B.

For test A, the plate was tested with its surface unobstructed. The unobstructed plate was located in the center of the autoclave and followed the same cycle as 5.3.1.1.1, Figure 5-21. The cure cycle was:

- pressurize to 50 psig
- heat at 5.0 °C/minute to 100.0 °C
- hold for 35 minutes
- pressurize to 100 psig
- heat at 5.0 °C/minute to 180.0 °C
- hold for 60 minutes

- pressurize to 0 psig
- cool at 5.0 °C/minute to 20.0 °C

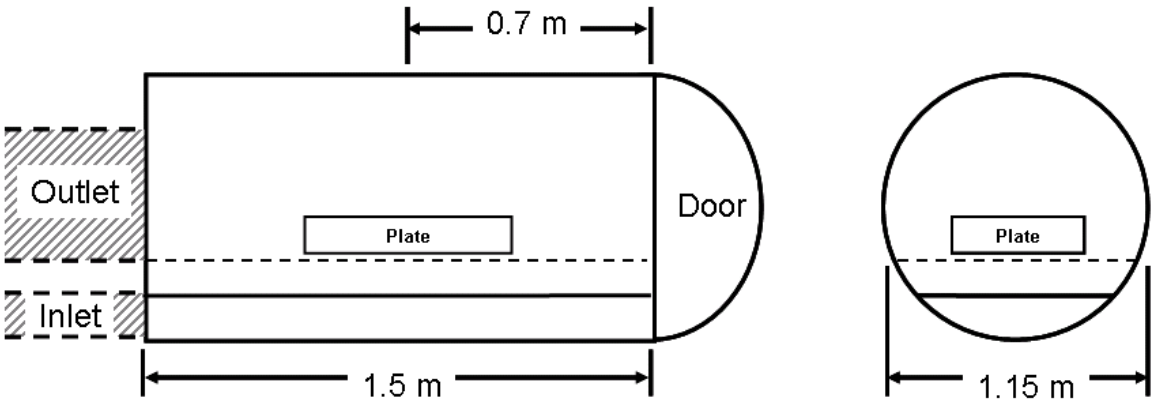

Figure 5-21: Location of steel plate used as a thermal gradient calorimeter.

For test B, three calorimeters were placed on top of the plate and three were placed below the plate to measure local effects around the plate, Figure 5-22. The cure cycle was:

- pressurize to 100 psig
- heat at 5.0 °C/minute to 180.0 °C
- hold for 30 minutes
- cool at 5.0 °C/minute to 20.0 °C
- pressurize to 0 psig

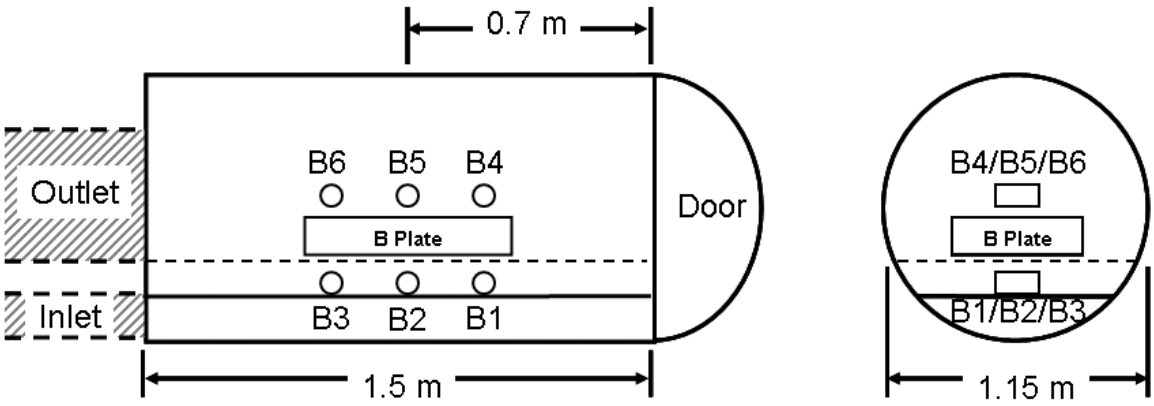

Figure 5-22: Calorimeter locations for testing local HTCs around the thermal gradient calorimeter.

Test B was repeated with a pressure of 0 psig instead of 100 psig. The new cycle was:

- heat at 5.0 °C/minute to 180.0 °C
- hold for 30 minutes

- cool at 5.0 °C/minute to 20.0 °C

5.3.1.2.2 Results and Discussion

Adding the steel plate had a significant effect on local HTCs by changing the local airflow. Table 5-2 shows the HTC values for the steel plate and surrounding calorimeters. The previous airflow observations showed B4 to be an area of low velocity or stagnant airflow, and the HTC of B4 was the lowest of the lumped-mass calorimeters. The HTC on the top of the plate was higher than the HTC on the bottom of the plate, but the calorimeters did not show the same trend. The calorimeters showed a lower HTC above the plate and a higher HTC below the plate. The difference was due to the calorimeters on the top of the plate being within 5.0 mm of the plate surface, whereas the calorimeters below the plate were 100.0mm below the surface. The positioning of the bottom calorimeters was such that they did not experience the same airflow as the bottom of the plate.

Table 5-2: Running average back-calculated HTCs for steel plate and surrounding calorimeters

	HTC (W/m^2K)			
Location	0 psi Heat Up	0 psi Cool Down	100 psi Heat Up	100 psi Cool Down
B Plate Top	33	36	106	145
B Plate Bottom	20	20	60	60
B1	55	66	177	182
B2	54	62	175	165
B3	62	64	173	171
B4	38	34	108	113
B5	43	42	158	162
B6	44	42	167	176

Below the plate, the HTC from the calorimeter closest to the outlet, B3, was much higher than the others. B1 and B2 were shadowed by B3, which reconfirmed the reversed airflow predicted by the CFD and visual observation, Figure 5-23.

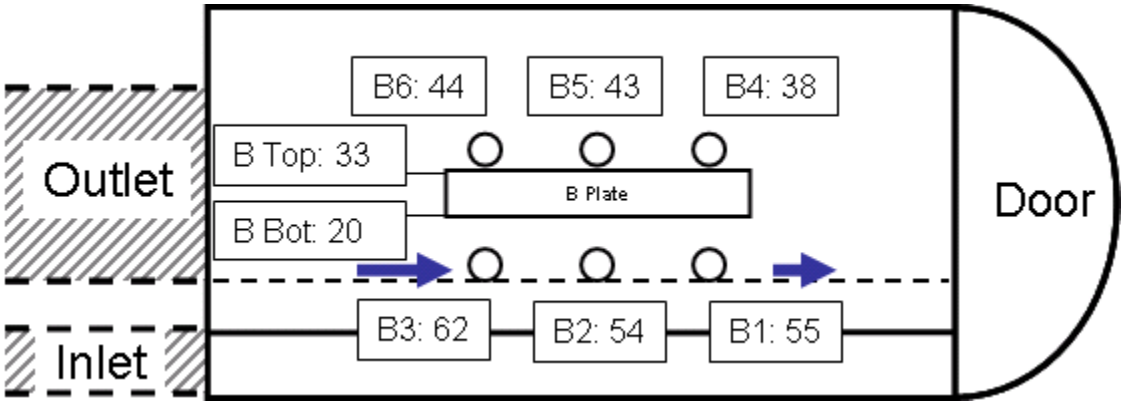

Figure 5-23: HTCs and airflow on, and around, the steel plate. Note top HTC is higher for the plate and lower for the lumped-mass calorimeters.

5.3.1.2.3 Length Scaling

The HTCs calculated from the steel plate were lower than the HTCs of the lumped-mass calorimeters, which are expected due to the difference in sizes of the two calorimeters. A length scaling correlation was developed by modifying the Petukhov correlation for fully developed turbulent flow in Table 2-2, repeated below:

$$h = \frac{0.037\,\mathrm{Re}^{0.8}\,\mathrm{Pr}}{1 + 2.443\,\mathrm{Re}^{-0.1}\left(\mathrm{Pr}^{2/3} - 1\right)} \cdot \frac{k_{fluid}}{L} \tag{5-3}$$

for constant μ_∞ and v, $Re \propto L$ (Equation (2-10)). Pr is length independent because it is a fluid property (Equation (2-11)), and $2.443\,\mathrm{Re}^{-0.1}\left(\mathrm{Pr}^{2/3} - 1\right) << 1$ so Equation (5-3) can be simplified to:

$$h \propto \frac{L^{0.8}}{1} \cdot \frac{1}{L} \tag{5-4}$$

which simplifies to

$$h \propto \frac{1}{L^{0.2}} \tag{5-5}$$

where L is the characteristic length. The top of the plate followed the correlation, but the bottom of the plate did not, Table 5-3. If the calorimeter on top of the plate had an HTC of 44 W/m^{2}K, the 0.5 m plate HTC should have been 28 W/m^2 K. The measured HTC was 18% higher, 33 W/m^2 K, than predicted. The bottom plate HTCs were 40% lower than predicted because the airflow was not parallel to the surface; it was already poorly oriented and was further disrupted by the geometry of the plate. As with the temperature and pressure scaling, the length scaling correlation did not apply in the autoclave due to the inconsistent airflow. If a precise HTC is

needed for a large part, it is better to instrument the part as a thermal-gradient calorimeter and back-calculate the effective HTC from that temperature data, rather than scale up the results from differently sized calorimeters.

Table 5-3: Length scaling for steel plate

	HTC ($W/m^2 K$)		
	Calorimeter	Plate Expected	Plate Measured
Top	44	28	33
Bottom	55	34	20

5.4 Temperature Field

A uniform temperature field is the goal of autoclave manufacturers, and the UBC autoclave maintained a 2.0 °C temperature distribution through most stages of the autoclave cycle. Using the autoclave air TC as the reference TC, the temperature differences between the autoclave air TC and the local air TC attached to the calorimetes were compared. Temperature data was from the calorimeters in Section 5.3.1.1, arranged as in Figure 5-24. Figure 5-25 shows the ΔT distribution for the local air temperature at Calorimeters A1, A6, and A8 in the empty autoclave.

A1 had the most stable response, within 1.0 °C during most of the cycle, and the response was typical of the variation shown by A2-A7. A6 was the location with the largest lag, but its variation was only 2.0 °C, like A1-A7, except during the pressure drop. The stability of all locations except for A8, the temperature in the inlet duct, indicated blasts of hot and cool air entered the autoclave through the ducting. Mixing occurred in the main chamber instead of entering the autoclave premixed at a uniform temperature. The peaks and valleys of the ΔT response showed when the electric heating element cycled on and off by the rapid heating of the autoclave air and a corresponding peak with an increased ΔT, Figure 5-26. The cool down did not have the same peaks because the autoclave was water cooled, and the water was not cycled on and off. Detailed air temperature histories showed that the actions of the autoclave components affect the temperature history, even though the temperature field was nearly uniform in the autoclave chamber.

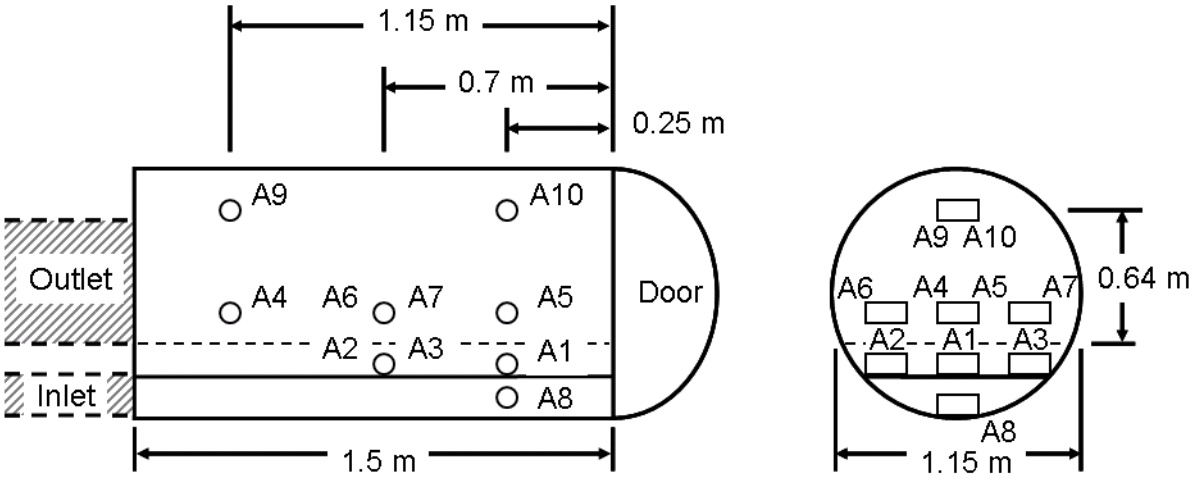

Figure 5-24: Thermocouple locations for temperature field measurements.

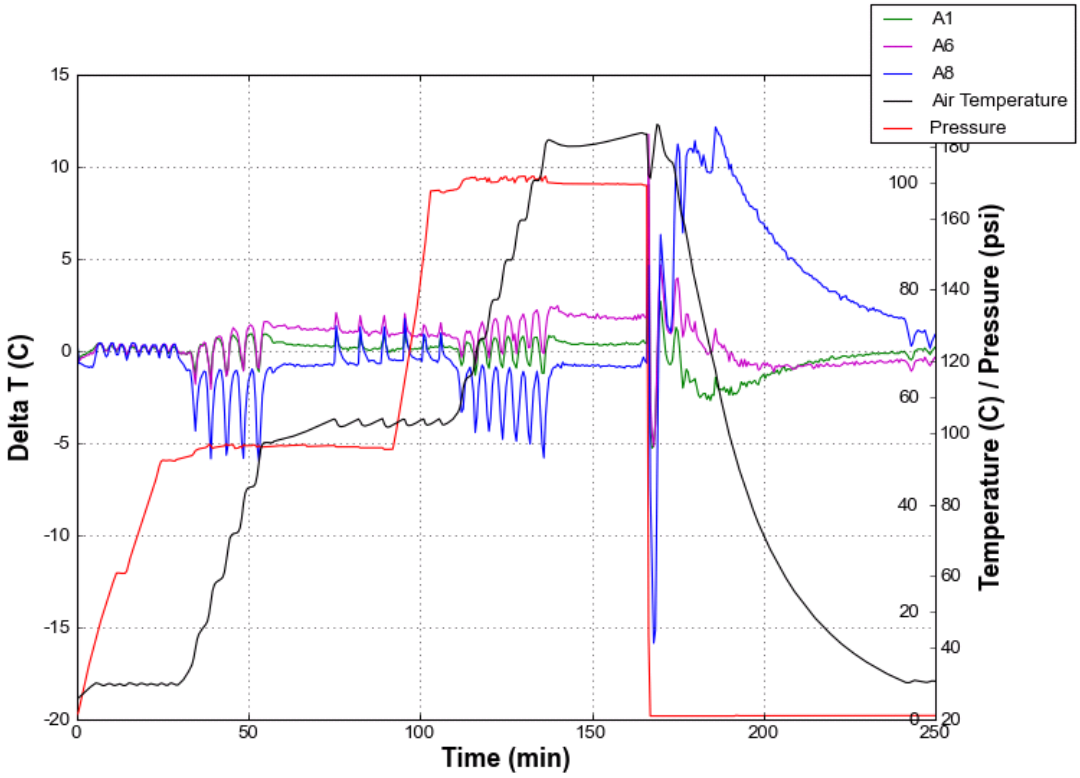

Figure 5-25: ΔT distribution throughout the autoclave cycle at locations A1, A6, and A8 (other locations omitted for clarity).

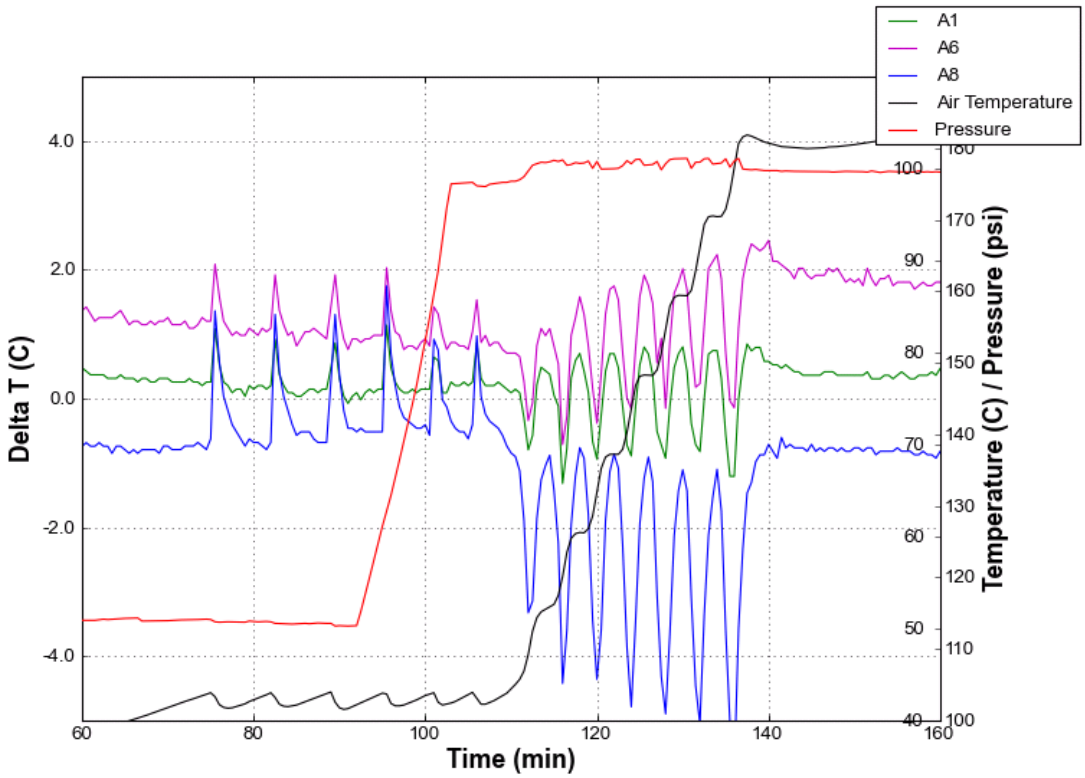

Figure 5-26: Close-up view of ΔT at locations A1, A6, and A8 during pressurization from 50 psig to 100 psig and ramp from 100 °C to 180 °C (other locations omitted for clarity).

5.5 Summary

Airflow inside the UBC autoclave was highly turbulent and poorly oriented, which creates uncertainty when processing parts. Four methods of characterizing the autoclave performance were used, and each method had advantages and disadvantages, Table 5-4. Understanding the airflow with visual monitoring and CFD reduced the uncertainty of the global and local convective heat transfer conditions inside the autoclave. HTC measurements further reduced the uncertainty by quantifying the observed airflow variation as a measured HTC variation. Further reinforcing the need to measure HTCs, the mechanical limitations of the autoclave made it such that scaling correlations could not be consistently applied. A strong argument can be made that an autoclave should be characterized by HTC and not by temperature uniformity or air velocities, as in no way did a uniform temperature distribution indicate uniform heat transfer.

Table 5-4: Summary of autoclave airflow and HTC characterization techniques

	Advantages	Disadvantages
Video	• Inexpensive • Instantaneous feedback • Intuitive • Large areas can easily be monitored	• Qualitative • Limited to ambient temperature and pressure
CFD	• Shows velocity magnitude and direction • All areas can be evaluated • Parametric evaluation	• Model may lack realistic detail • Time consuming, expensive • Requires skilled personnel • Must be validated experimentally
Lumped-mass Calorimeters	• Inexpensive • Provides representative HTC values • Small footprint allows many sensors to be used simultaneously	• Time consuming data reduction for non-steady state thermal histories • Non-directional • Length scale dependency (real HTC may be different) • Local
Thermal-gradient Calorimeters	• Inexpensive • Wide variety of material choices • Provides top and bottom HTC • Composite can be used	• Accuracy limited by number of TCs • Time consuming data reduction • Non-directional • Length scale dependency (real HTC may be different) • Local

A simple workflow is proposed to efficiently characterize an autoclave using the developed visual monitoring and calorimetry methods, Figure 5-27. Visual monitoring or CFD is first used to determine the airflow patterns in the empty autoclave. HTC is measured in the highest and lowest airflow areas, as well as the areas where parts will be cured, using lumped-mass or thermal gradient calorimeters. The process can be repeated as needed at different pressures or with different autoclave loads. Parts and tools can also be used as thermal gradient calorimeters to determine the exact heat transfer conditions on the part.

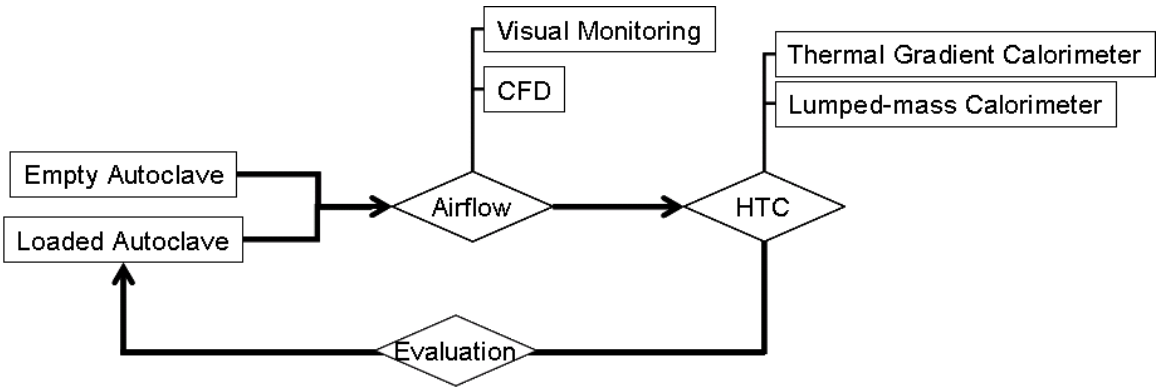

Figure 5-27: Workflow for characterizing an autoclave

6 Summary, Conclusions and Future Work

6.1 Conclusions

A systematic approach to validating conductive heat transfer, thermochemical, and convective heat transfer sub-models for thermosetting composite materials has been developed and demonstrated. By separately validating the sub-models, the uncertainty associated with the complete thermal simulation was significantly reduced. Evaluation of the conductive sub-models showed that predictions within 1.0 °C can be made for rubber, peel-ply, and composite material models. However, the FEP barrier film is not accurately modeled using only its density, specific heat, and thermal conductivity parameters due to interfacial contact resistances.

The developed methodology was used to validate and compare available material models; it was DSC independent and used full-sized laminates. The set-temperature model boundaries have less uncertainty than the HTC boundaries, and the gradient through the bricks verifies the accuracy of the composite model boundary without forcing agreement at said boundary. Measureable differences between experiments and simulations, as well as between models for the same material, were observed. Fully cured composite thermochemical simulations showed excellent agreement for all four materials tested, thus reducing the uncertainty of errors observed with the curing simulations because the inert model properties were correct. Agreement during the curing process was not as good, with predictions varying from better than 1.0 °C (CF2426A/MTM45-1) to errors greater than 5.0 °C (Hexcel AS4/8552 Open Literature). However, having regularly achieved the proposed 2.0 °C target for model agreement showed that it is reasonable to expect current and future thermochemical models to make predictions within a 2.0 °C window.

The uncertainty of a thermal simulation was further reduced by understanding the airflow patterns inside the autoclave and measuring the autoclave HTCs. Simple visual observation and calorimetry methods were used to characterize the UBC autoclave. HTCs varied by more than a factor of two, although the temperature field varied by only 2.0 °C. Length, pressure, and temperature correlations could not be applied due to the highly turbulent and poorly oriented airflow observed in the autoclave, coupled with the mechanical limitations of the autoclave components. Experimental measurements were the only way to reduce the uncertainty of the autoclave environment. The methods developed by the author, which were demonstrated on the autoclave, are equally applicable to convection oven environments.

Using this work as a foundation, a standardized methodology can be developed for validating thermochemical models and characterizing autoclave performance.

6.2 Future Work

Improvements can be made in the methods developed to validate the thermal sub-models. The uncertainty of the cure assembly thermal model could be further reduced by:

- Improving the understanding of the effects and magnitudes of the interfacial thermal contact resistances. There was clearly a discontinuity in the through-thickness temperature profiles which resulted from the resistance of the FEP film layer required by the thermochemical validation test.
- Incorporating the ability to vary HTCs during a thermal simulation. Cure cycles with multiple pressures and the mechanical limitations of the equipment can be modeled more realistically by varying the HTC boundary during the cycle.
- Improving the repeatability of the thermochemical validation tests can be achieved by using larger laminates and by developing a rigid and reusable insulator. Larger laminates will be less sensitive to resin bleed and 2-D heat transfer. The breather cloth did not compress evenly during the testing and was time-consuming to fabricate for each test. A different low conductivity, low thermal mass material could be used for a more stable and permanent insulation method.
- The mapping of the airflow patterns inside an autoclave or oven can be improved with an indicating device that provides a calibrated response to airflow direction and magnitude.

References

Advanced Thermal Solutions. (2007). *Understanding heat transfer coefficient*. Norwood, MA: QATS.com.

American Power Conversion Corp. (2010). *Back-UPS ES USB 650VA w/TEL & COAX 120V*. Retrieved January 11, 2010, from http://www.apc.com/products/resource/include/techspec_index.cfm?base_sku=BE650BB&tab=models

Antonucci, V., Giordano, M., Inserraimparato, S., & Nicolais, L. (2001). Analysis of heat transfer in autoclave technology. *Polymer Composites, 22*(5), 613.

Antonucci, V., Giordano, M., Imparato, S. I., & Nicolais, L. (2002). Autoclave manufacturing of thick composites. *Polymer Composites, 23*(5), 902-910.

ASME V&V 10-2006 (Ed.). (2006). *Guide for verification and validation in computational solid mechanics*. New York: American Society of Mechanical Engineers.

ASTM Standard E 2041. (2008). *Standard method for estimating kinetic parameters by differential scanning calorimeter using the borchardt and daniels method*. West Conshohocken, PA: ASTM International.

ASTM Standard E 2070. (2008). *Standard test method for kinetic parameters by differential scanning calorimetry using isothermal methods*. West Conshohocken, PA: ASTM International.

ASTM Standard E 2160. (2004). *Standard test method for heat of reaction of thermally reactive materials by differential scanning calorimetry*. West Conshohocken, PA: ASTM International.

ASTM Standard E 698. (2005). *Standard test method for arrhenius kinetic constants for thermally unstable materials*. West Conshohocken, PA: ASTM International.

Bogetti, T. A., & Gillespie, J. W. (1991). 2-dimensional cure simulation of thick thermosetting composites. *Journal of Composite Materials, 25*(3), 239-273.

Ciriscioli, P. R., Wang, Q. L., & Springer, G. S. (1992). Autoclave curing - comparisons of model and test-results. *Journal of Composite Materials, 26*(1), 90-102.

Convergent Manufacturing Technologies Inc. (2010).

Cytec Industries Inc. (2003a). *Thornel P-25 product data sheet*

Cytec Industries Inc. (2003b). *Thornel P-30 product data sheet*

Cytec Industries Inc. (2003c). *Thornel T-300 product data sheet*

Cytec Industries Inc. (2003d). *Thornel T-650/35 product data sheet*

Dykeman, D. (2008). Minimizing uncertainty in cure modeling for composites manufacturing. (PhD, The University of British Columbia).

Dykeman, D., & Poursartip, A. (2004). Process maps for design of cure cycles for thermoset matrix composite materials. *36th International SAMPE Technical Conference - Materials and Processing:Sailing into the Future, November 15, 2004 - November 18,* 1079-1087.

Ghariban, N., Lou, D. Y. S., & Haji-Sheikh, A. (1992). The effect of honeycomb flow straighteners on turbulence and heat transfer in an autoclave model. *Winter Annual Meeting of the American Society of Mechanical Engineers,* Anaheim, California. 45.

Guo, Z., Du, S., & Zhang, B. (2005). Temperature field of thick thermoset composite laminates during cure process. *Composites Science and Technology, 65*(3-4), 517-523.

Heisler, M. P. (1947). Temperature charts for induction and constant temperature heating. *Transaction of American Society of Mechanical Engineers, 69*, 227-236.

Hexcel Corporation. (2010a). *HexTow AS4 product data sheet*. Stamford, Connecticut:

Hexcel Corporation. (2010b). *HexTow IM10 product data sheet*. Stamford, Connecticut:

Hexcel Corporation. (2010c). *HexTow IM7 product data sheet*. Stamford, Connecticut:

Hubert, P., Johnston, A., Poursartip, A., & Nelson, K. (2001). Cure kinetics and viscosity models for Hexcel 8552 epoxy resin. *2001: A Materials and Processes Odyssey, Books 1 and 2, 46*, 2341-2354.

Hubert, P., Johnston, A., Vaziri, R., & Poursartip, A. (1995). A two-dimensional finite element processing model for FRP composite components. *Tenth International Conference on Composite Materials, 14-18 Aug. 1995,* Whistler, British Columbia, Canada. 149-156.

Johnston, A. (1997). An integrated model of the development of process-induced deformation in autoclave processing of composite structures. (PhD, The University of British Columbia).

Johnston, A., Hubert, P., Vaziri, R., & Poursartip, A. (1998). In Hoa S., Hamada H. (Eds.), *An investigation of autoclave convective heat transfer*. Lancaster; 851 New Holland Ave, Box 3535, Lancaster, PA 17604 USA: Technomic Publishing Co Inc.

Kutz, M. (1998). Heat transfer fundamentals. *Mechanical engineers' handbook* (2nd ed., pp. 1367) John Wiley & Sons.

Lienhard, J. H. (2006). *A heat transfer textbook: Third edition*. Cambridge: Phlogiston Press.

Logitech. (2010). *QuickCam orbit AF.* Retrieved April 9, 2010, from http://www.logitech.com/index.cfm/webcam_communications/webcams/devices/3480&cl=us,en

Loos, A. C., & Springer, G. S. (1983). Curing of epoxy matrix composites. *Journal of Composite Materials, 17*(2), 135-169.

Maijer, D., & Poursartip, A. (2005). Unpublished manuscript.

Merzkirch, W. (1987). *Flow visualization*. Orlando: Orlando : Academic Press.

Microelectronics Heat Transfer Laboratory. (1998). *Fluid properties calculator.* Retrieved June 14, 2010, from http://www.mhtl.uwaterloo.ca/old/onlinetools/airprop/airprop.html

MIL-HDBK-17-1F. (2002). *The composite materials handbook, volume 1: Polymer matrix composites: Guidelines for characterization of structural materials* ASTM International.

MIL-HDBK-17-2F. (2002). *The composite materials handbook, volume 2: Polymer matrix composites: Materials properties* ASTM International.

MIL-HDBK-17-3F. (2002). *The composite materials handbook, volume 3: Polymer matrix composites: Materials usage, design, and analysis* ASTM International.

Omega. (2010a). *88000 series: Thin leaf-type thermocouples.* Retrieved June 16, 2010, from http://www.omega.ca/shop/pptsc.asp?ref=88000_thinfoil&Nav=tema11

Omega. (2010b). *SA1 series: Surface thermocouple with self-adhesive backing.* Retrieved June 16, 2010, from http://www.omega.ca/shop/pptsc.asp?ref=SA1&Nav=tema11

Omega. (2010c). *SA2 series: Self-adhesive thermocouples molded silicone design.* Retrieved June 16, 2010, from http://www.omega.ca/shop/pptsc.asp?ref=SA2&Nav=tema11#

Omega. (2010d). *Thermocouples and thermocouple sensors.* Retrieved April 30, 2010, from http://www.omega.ca/prodinfo/thermocouples.html

Peters, S. T. (Ed.). (1998). *Handbook of composites* (Second Edition ed.). London: Chapman & Hall.

Pursley, M. (1987). Lockheed Corporation, *Heat flux meter*, US Patent 4,653,934. CA/USA.

Rasekh, A., Vaziri, R., & Poursartip, A. (2004). Simple techniques for thermal analysis of the processing of composite structures. *36th ISTC,* San Diego, CA.

Roberts, R. W. (1987). Cure quality control. *Engineering materials handbook* (pp. 745-760) ASM International.

Salagnac, P., Dutournié, P., & Glouannec, P. (2004). Curing of composites by radiation and natural convection in an autoclave. *AICHE Journal, 50*(12), 3149-3159.

Schuster, J., Heider, D., Sharp, K., & Glowania, M. (2009). Measuring and modeling the thermal conductivities of three-dimensionally woven fabric composites. *Mechanics of Composite Materials, 45*(2), 165-174.

Shimizu, T., Kotlik, J., Arafath, A. R. A., & Poursartip, A. (2008). Evaluation of temperature profiles in thick composite parts during autoclave processing. *23rd Intl. ASC Technical Conference,* Memphis, USA.

Shin-Etsu Chemical Co., L. (2004). *Shin-etsu silicone: RTV rubber product data sheet*

Spang, B. (2008). *Correlations for convective heat transfer.* Retrieved May 30, 2010, from http://www.cheresources.com/convection.shtml#flat

Springer, G. S., & Tsai, S. W. (1967). Thermal conductivities of unidirectional materials. *Journal of Composite Materials, 1*(2), 166-173.

TA Instruments. (2010). *Differential scanning calorimeters.* Retrieved May 3, 2010, from http://www.tainstruments.com/product.aspx?id=10&n=1&siteid=11

Toray Inc. (2005). *Functional and composite properties.* Retrieved April 17, 2010, from http://www.torayca.com/techref/en/images/fcp02.htm

Toray Inc. (2010a). *M35J product data sheet*. Santa Ana, California:

Toray Inc. (2010b). *M40J product data sheet*. Santa Ana, California:

Toray Inc. (2010c). *M46J product data sheet*. Santa Ana, California:

Toray Inc. (2010d). *M50J product data sheet*. Santa Ana, California:

Toray Inc. (2010e). *M55J product data sheet*. Santa Ana, California:

Toray Inc. (2010f). *M60J product data sheet*. Santa Ana, California:

Toray Inc. (2010g). *T1000G product data sheet*. Santa Ana, California:

Toray Inc. (2010h). *T300 product data sheet*. Santa Ana, California:

Toray Inc. (2010i). *T700S product data sheet*. Santa Ana, California:

Toray Inc. (2010j). *T800S product data sheet*. Santa Ana, California:

TRENDnet. (2010). *Wireless SecurView camera series - TV-IP410W*. Retrieved January 11, 2010, from http://www.trendnet.com/langen/products/proddetail.asp?prod=160_TV-IP410W&cat=148

Twardowski, T. E., Lin, S. E., & Geil, P. H. (1993). Curing in thick composite laminates: Experiment and simulation. *Journal of Composite Materials, 27*(3), 216-250.

Yi, S., Hilton, H. H., & Ahmad, M. F. (1997). A finite element approach for cure simulation of thermosetting matrix composites. *Computers & Structures, 64*(1-4), 383-388.

Zhang, G., Xia, Y., Wang, H., Tao, Y., Tao, G., Tu, S., et al. (2010). A percolation model of thermal conductivity for filled polymer composites. *Journal of Composite Materials, 44*(8), 963-970.

Zhang, J., Xu, Y., & Huang, P. (2010). Effect of cure cycle on temperature/degree of cure field and hardness for epoxy resin. *E-Polymers,* , 007.

Zielenkiewicz, W. (2008). Towards classification of calorimeters. *Journal of Thermal Analysis & Calorimetry, 91*(2), 663-671.

Appendix A - Process Maps

Process maps were generated using RAVEN process simulation software and material models provided by Convergent Manufacturing Technologies Inc. (Convergent Manufacturing Technologies Inc., 2010). The five material models were: ACG CF2426A/MTM45-1, Open Literature and NCAMP Hexcel AS4/8552, Toray T800H/3900-2, and Toray T700/2510 (Figure A-1 through Figure A-5, respectively). Note the difference between the Open Literature and NCAMP Hexcel AS4/8552 models: the cure rate and final DoC is higher in the NCAMP model than the Open Literature, Figure A-2 and Figure A-3. The steep slopes of the Toray 2510 curves show the high reactivity of the resin system, Figure A-5.

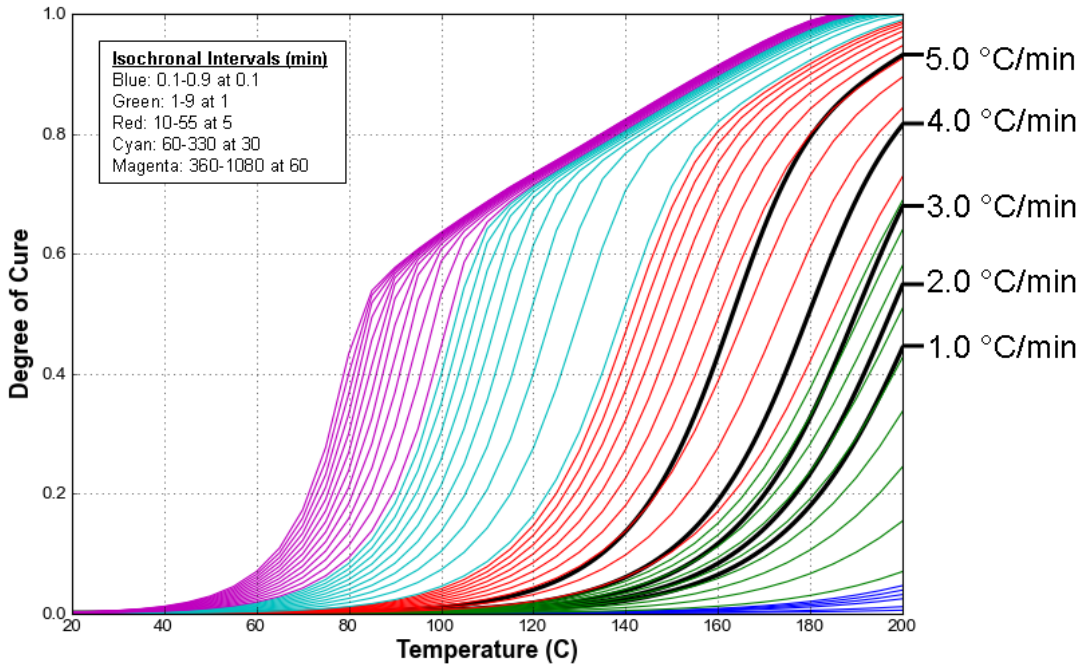

Figure A-1: Process map for ACG CF2426A/MTM45-1 with colored isochronal lines and black dynamic lines. Adapted from material provided by Convergent Manufacturing Technologies Inc. (2010).

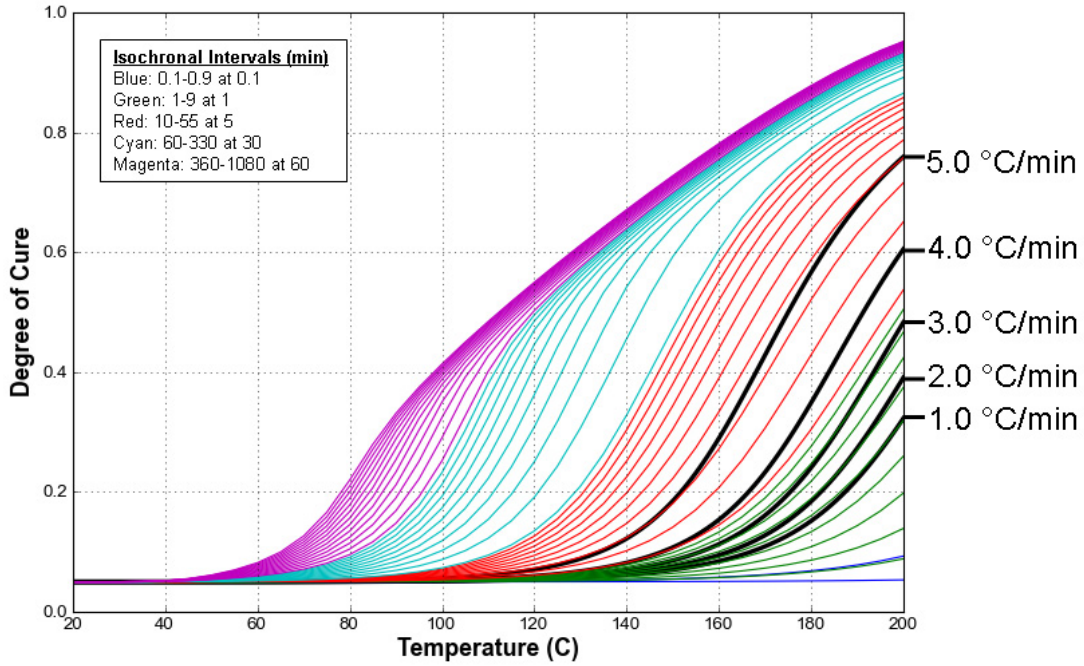

Figure A-2: Process map for Hexcel AS4/8552 Open Literature model with colored isochronal lines and black dynamic lines. Adapted from material provided by Convergent Manufacturing Technologies Inc. (2010).

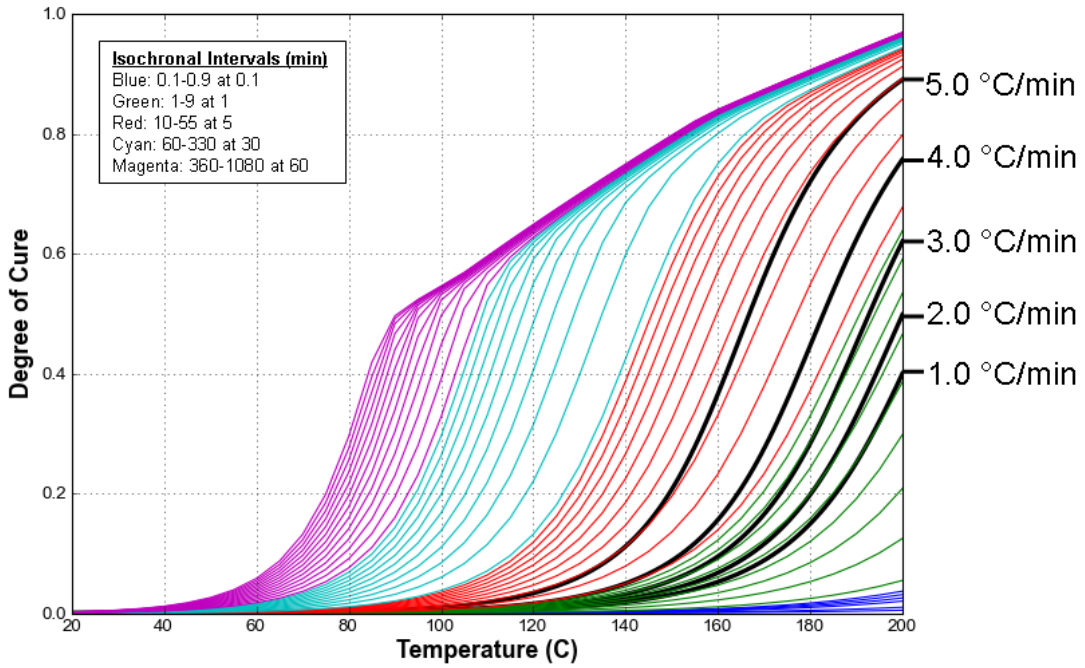

Figure A-3: Process map for Hexcel AS4/8552 NCAMP model with colored isochronal lines and black dynamic lines. Adapted from material provided by Convergent Manufacturing Technologies Inc. (2010).

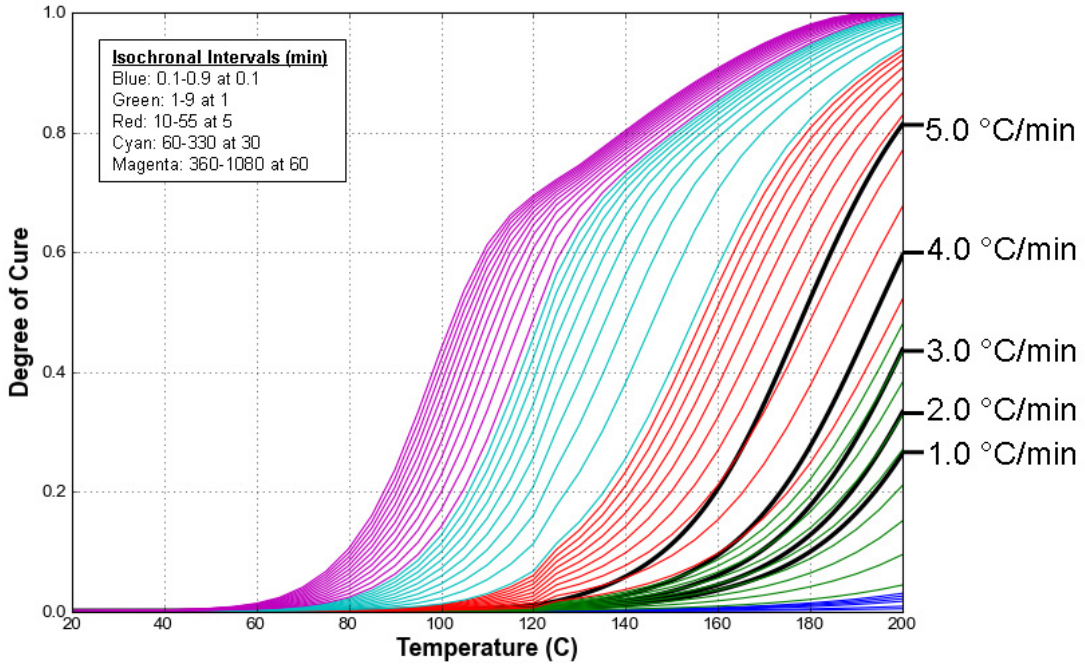

Figure A-4: Process map for Toray T800H/3900-2 with colored isochronal lines and black dynamic lines. Adapted from material provided by Convergent Manufacturing Technologies Inc. (2010).

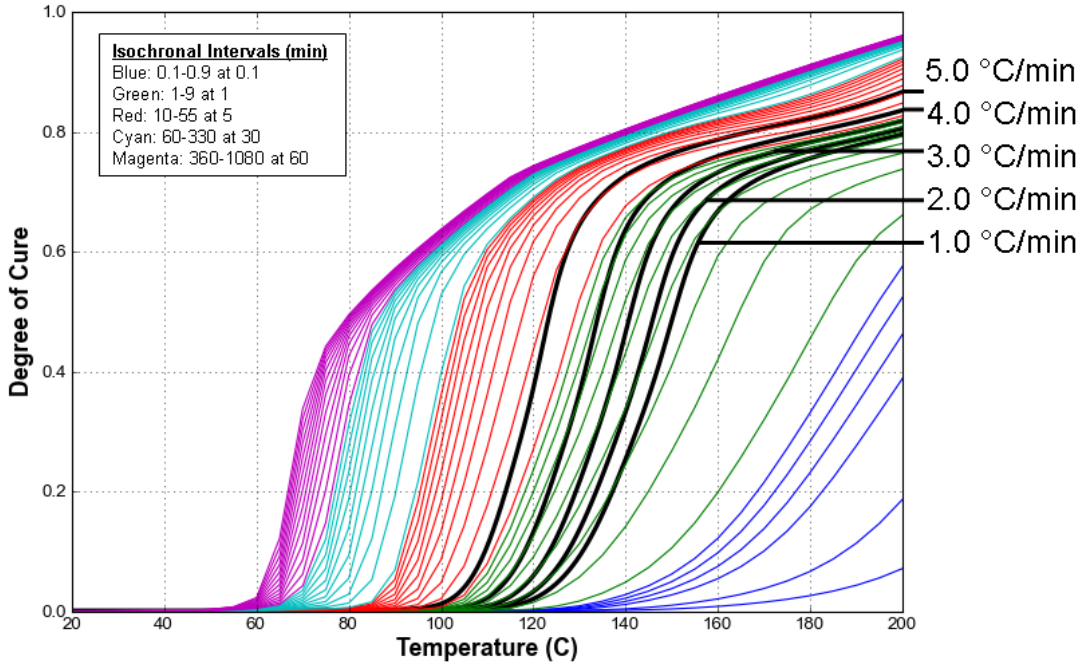

Figure A-5: Process map for Toray T700/2510 with colored isochronal lines and black dynamic lines. Adapted from material provided by Convergent Manufacturing Technologies Inc. (2010).

Appendix B - KE1204 Brick Fabrication

1. Place the TC tips inside slits that are cut at 3.0 mm intervals in a pre-cast 16.0 mm cube, Figure B-1. The wires are wrapped around the brick to provide strain relief and extend the lifespan of the brick.

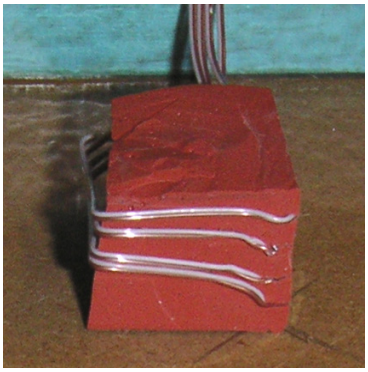

Figure B-1: Pre-cast cube with TCs tips inside slits.

2. Center precast cube with the embedded TCs in a 100 mm x 100 mm x 16 mm mold and fill the mold with uncured KE1204, Figure B-2 A. Place a flat caul plate on top of the mold to eliminate the curvature resulting from the surface tension of the liquid rubber, Figure B-2 B. Cure at room-temperature before demolding.

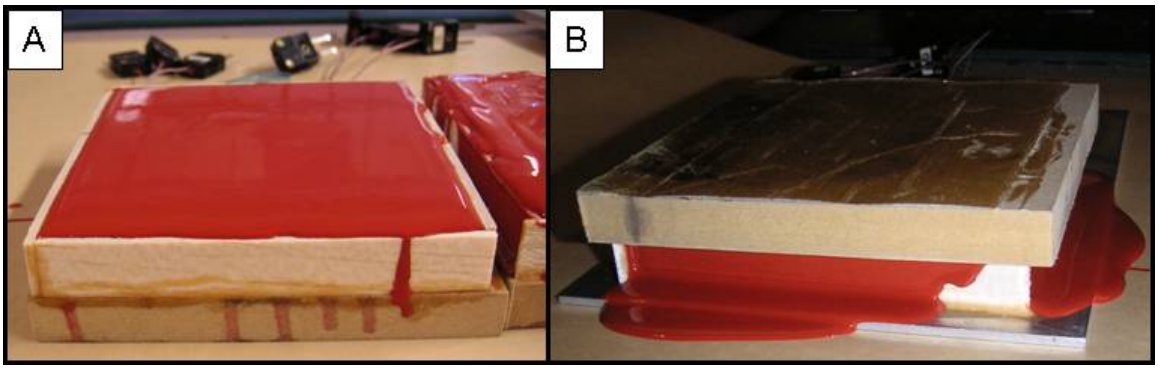

Figure B-2: A) Mold filled with uncured liquid KE1204; B) Caul plate on top of mold to remove curvature created by surface tension.

Appendix C - DSC Results

Specific heat capacities for the Shin-Etsu KE1204 rubber, the peel-ply, and FEP film were measured with a TA Instruments Q1000 DSC, Figure C-1, Figure C-2, and Figure C-3.

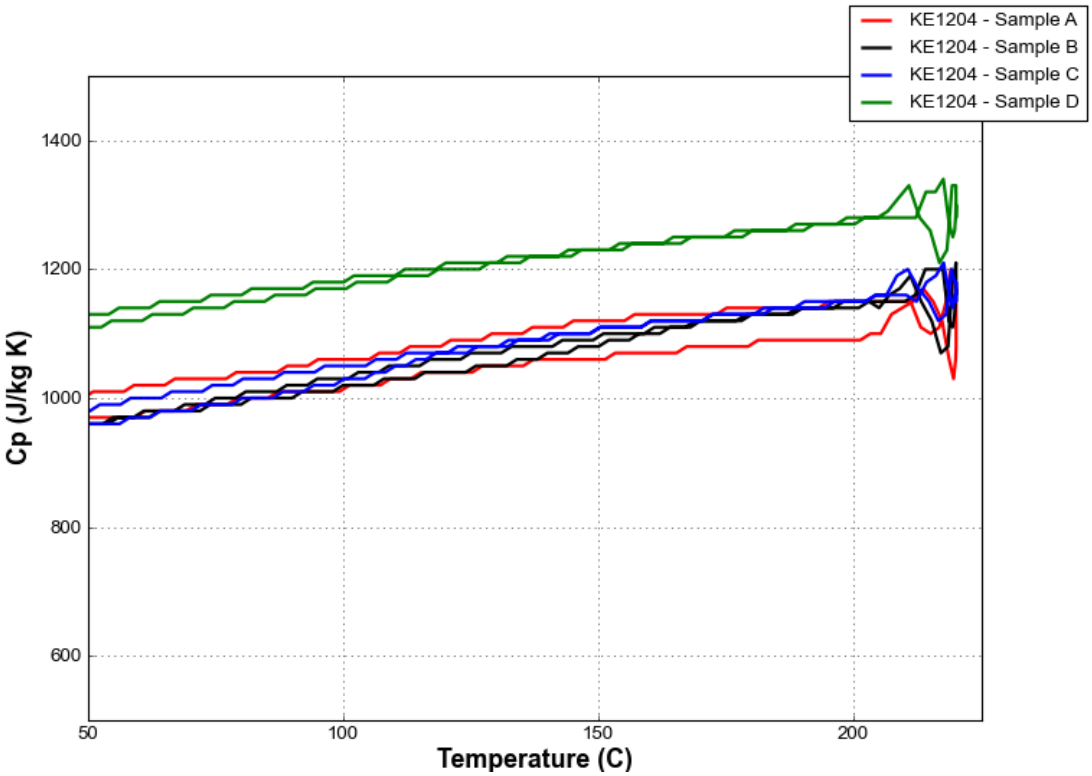

Figure C-1: DSC data for four KE1204 samples. Sample D was offset by 100 J/kgK, but had the same slope as the other samples.

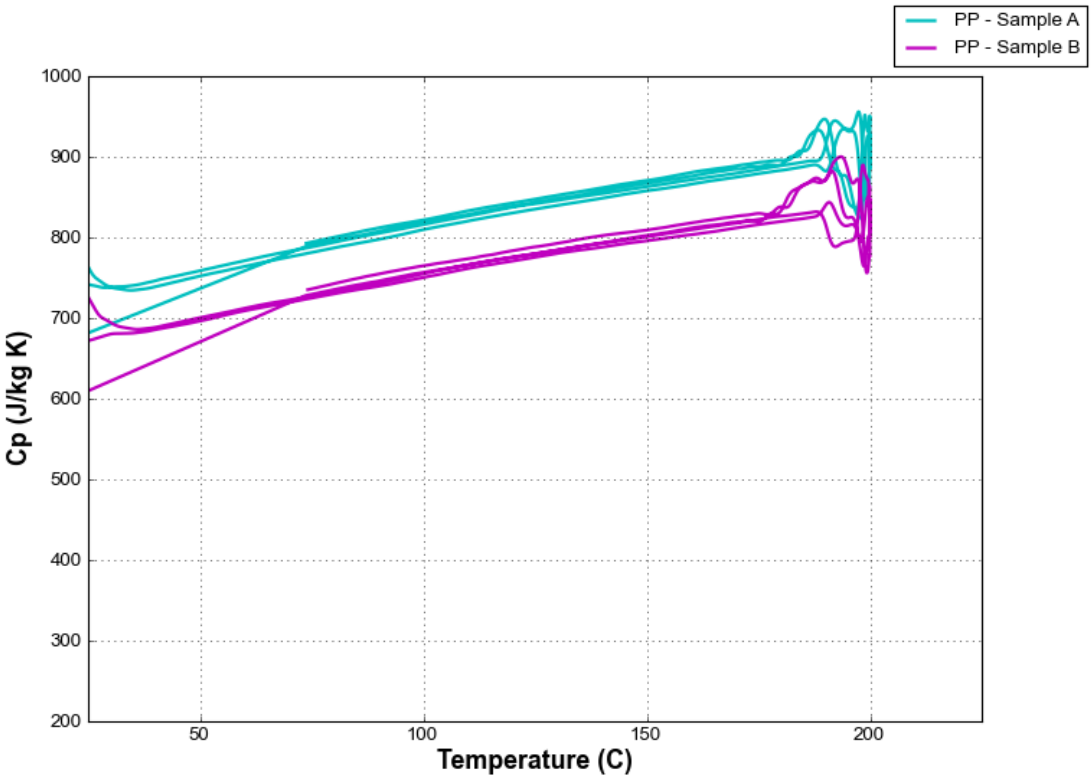

Figure C-2: DSC data for two peel-ply samples. There was an offset of 50 J/kg K, but the samples had the same slopes.

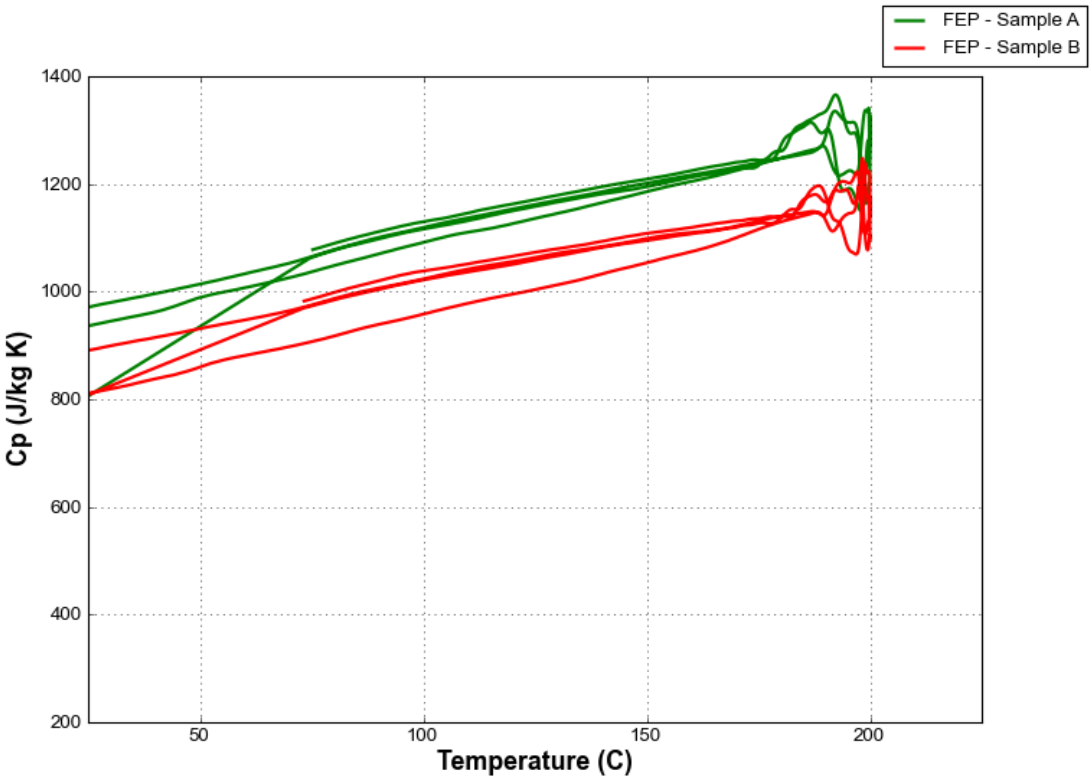

Figure C-3: DSC data for two FEP samples. There was an offset of 100 J/kg K, but the samples had the same slopes.

Appendix D - Conductive Validation Test Procedure

1. Place at least three TCs through the thickness of the center of the material to be investigated, Figure D-1.

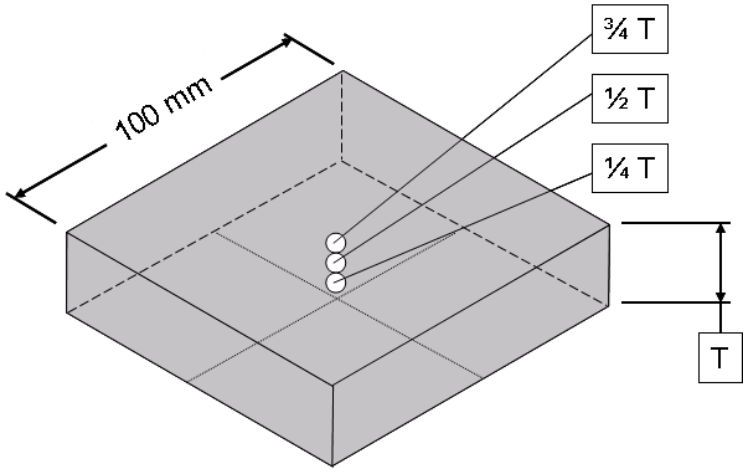

Figure D-1: Thermocouples are located at the center of the material at 1/4, 1/2, and 3/4 points of the thickness.

2. Place the instrumented material between two rubber bricks. Place TCs centered on the top and bottom surfaces of the brick, and at the interfaces between the two bricks and the material. A detailed through-thickness temperature profile can be recorded because there is now a total of 15 TCs aligned through the thickness of the stack (1 at the bottom surface, 4 in each brick, 3 in the material, 2 at the interfaces, and 1 at the top surface).

3. Insulate the edges of the stack with a 30.0 mm perimeter of breather cloth. The breather cloth is a low conductivity, low thermal mass material. The breather ensures that heat transfer is 1-D through the thickness without absorbing an excessive amount of heat. The amount of breather that is required varies depending on the dimensions and aspect ratios of the stack of materials; in this work 30.0 mm was sufficient to provide a 1-D solution, as verified by the absence of an experimental in-plane thermal gradient.

4. Envelope bag the assembly, being sure to keep the breather as square as possible. Vacuum-bagging is necessary to ensure that the materials are pressed together and that the pressure across the interfaces is consistent.

5. Record temperature data from all the TCs during a thermal cycle.

6. Use the measured surface temperatures as set-temperature boundary conditions for a 1-D simulation of the material stack. Using a set-temperature eliminates the uncertainty of the HTC boundary on the surfaces.

Appendix E - Thermochemical Validation Test Procedure

1. Lay up the laminate with TCs embedded at intervals of 1/4, 1/2, and 3/4 through the thickness, Figure E-1 Frame 1. Debulk the laminate per the manufacturer's recommendations, or as needed.

2. Measure and record the laminate mass and thickness. The mass is used to calculate the V_f. Comparing the uncured and cured thicknesses shows the amount of compaction that occurred during cure.

3. Wrap the laminate with peel-ply and perforated release film, Figure E-1 Frame 2. Controlling resin bleed while ensuring that voids are eliminated is critical since the thermal response of the laminate is sensitive to the V_f and porosity. The peel-ply contains most of the resin bleed, and the barrier film stop resin from flowing into the breather insulation.

4. Place TCs centered on the top surface, bottom surfaces, and at the interfaces between the two bricks and the material, Figure E-1 Frame 3. A detailed through-thickness temperature profile can be recorded because there is now a total of 15 TCs aligned through the thickness of the stack (1 at the bottom surface, 4 in each brick, 3 in the laminate, 2 at the interfaces, and 1 at the top surface).

5. Place the laminate between two rubber bricks, as in Figure E-1 Frame 4

6. Insulate the edges of the stack with a 30.0 mm perimeter of breather cloth, Figure E-1 Frame 5. The breather cloth is a low conductivity, low thermal mass material. The breather ensures that heat transfer is 1-D through the thickness without absorbing an excessive amount of heat, Figure 3-12. The amount of breather that is required varies depending on the dimensions and aspect ratios of the stack of materials; in this work 30.0 mm was sufficient to provide a 1-D solution, as verified by the absence of an experimental in-plane thermal gradient.

7. Envelope bag the assembly, being sure to keep the breather as square as possible, Figure E-1 Frame 6. Vacuum-bagging is necessary to ensure that the materials are pressed together, that the pressure across the interfaces is consistent, and that the laminate compacts properly during cure.

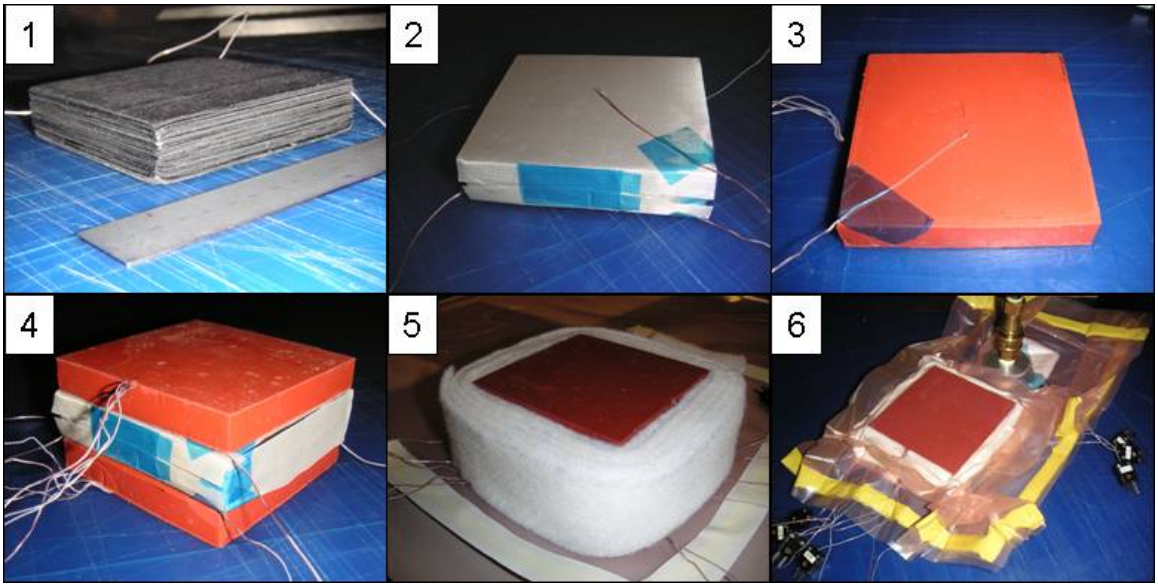

Figure E-1: Thermochemical validation specimen fabrication steps: 1) lay up laminate with through-thickness TCs; 2) wrap laminate with peel ply and barrier film; 3) place TCs at interface and surface of rubber bricks; 4) sandwich laminate between rubber bricks; 5) insulate edges with breather; 6) envelope bag entire cure assembly.

8. Record temperature data from all the TCs during a thermal cycle.
9. Repeat Step 8 on the fully cured material stack.
10. Measure and record the laminate mass and thickness.
11. Calculate the final V_f using Equation (E-1) below. A mass based V_f calculation is used because it is unaffected by porosity or thickness variations in the laminate. Several assumptions are made in the mass based calculation:
    - the mass of fibers does not change during cure
    - resin bleed is the only mass lost
    - the prepreg is initially at nominal V_f
    - data sheet values for fiber and cured resin density are correct

    The final fiber volume fraction is calculated using:

$$
\begin{aligned}
m_f &= \frac{m_{C0}}{\rho_C} V_{f\,\mathrm{nom}} \cdot \rho_f \\
m_r &= m_{Cf} - m_f \\
Final\,V_f &= \frac{\dfrac{m_f}{\rho_f}}{\dfrac{m_f}{\rho_f} + \dfrac{m_r}{\rho_r}}
\end{aligned}
\qquad \text{(E-1)}
$$

where m_f is fiber mass, m_r is resin mass, m_{C0} is the mass of the uncured composite, m_{Cf} is the mass of the cured composite, $V_{f\,nom}$ is the data sheet value for nominal fiber volume fraction, ρ_C is nominal composite density, ρ_f is fiber density, and ρ_r is resin density.

12. Use the measured surface temperatures as set-temperature boundary conditions for a 1-D simulation of the material stack. Using a set-temperature eliminates the uncertainty of the HTC boundary on the surfaces.

Appendix F - 1-D vs. 3-D Analysis

The objective of the test methodology was to be able to perform the simulations in 1-D to simplify and speed-up analysis, but resin bleed from the edges was a 2- or 3-Dimensional phenomenon. It can be shown, however, that a 1-D approximation was acceptable for V_fs up to 10% above nominal. Most of the heat generated by the bled resin was transferred to the laminate because of the high in-plane thermal conductivity. A mesh of 3920 8-noded linear solid elements (4725 total nodes) was used for 3-D simulation of the cure assembly. Due to the symmetry of the problem, a quarter section of the cure assembly was modeled, Figure F-1. A set-temperature boundary was applied to the surfaces of the rubber in 1-D, and the same boundary is applied to the top and bottom surfaces in 3-D, plus a different set-temperature on the exterior surface of the breather in 3D. All boundary temperatures were from experimental thermocouple data.

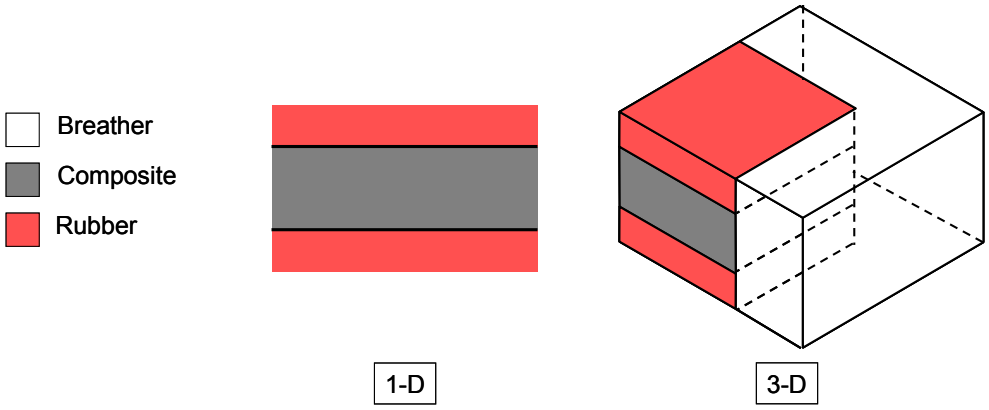

Figure F-1. Geometry of 1-D and 3-D models used for simulations.

A block of neat resin was modeled at the edge of the laminate model for the resin bleed in 3-D, Figure F-2. The mass of the resin bleed, the resin density, and the area of the exposed edges were used to calculate the thickness of the resin in the resin block:

$$T_{resin} = \frac{\frac{m_{bleed}}{\rho_{resin}}}{4 L T_{laminate}} \qquad \textbf{(F-1)}$$

where m_{bleed} is the mass of resin bleed, ρ_{resin} is the density of the resin, L is the length of the side of the laminate, and $T_{laminate}$ is the thickness of the cured laminate. The 50 ply 3-D laminate model uses the V_f of the cured experimental laminate in Table 4-1 and a 3.5 mm block of resin along the laminate edges.

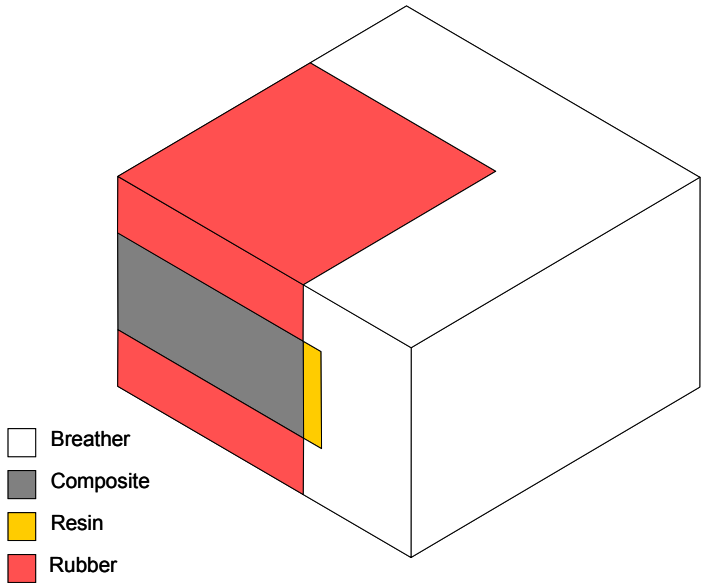

Figure F-2: 3D model with additional bled resin block

Simulation showed that there was significant in-plane heat transfer from the resin block, Figure F-3. Agreement for the 1-D simulation with nominal V_f (0.54) was not as good as the 3-D simulation, Figure F-4. The resin block improved the peak exotherm agreement between the experiment and the simulation from 1.1 °C to 0.2 °C. The 1-D simulation at the actual V_f under-predicted the exotherm by 1.2 °C because it had less total resin mass than the experiment, 1-D nominal V_f, and 3-D simulations. 3-D was the best solution since the laminate model has density, specific heat capacity, and thermal conductivity properties of the high V_f laminate while still having the correct total resin mass. However, approximating with a 1-D simulation at nominal V_f achieved agreement better than the 2.0 °C target with a simpler approach that did not require modifications to the material model.

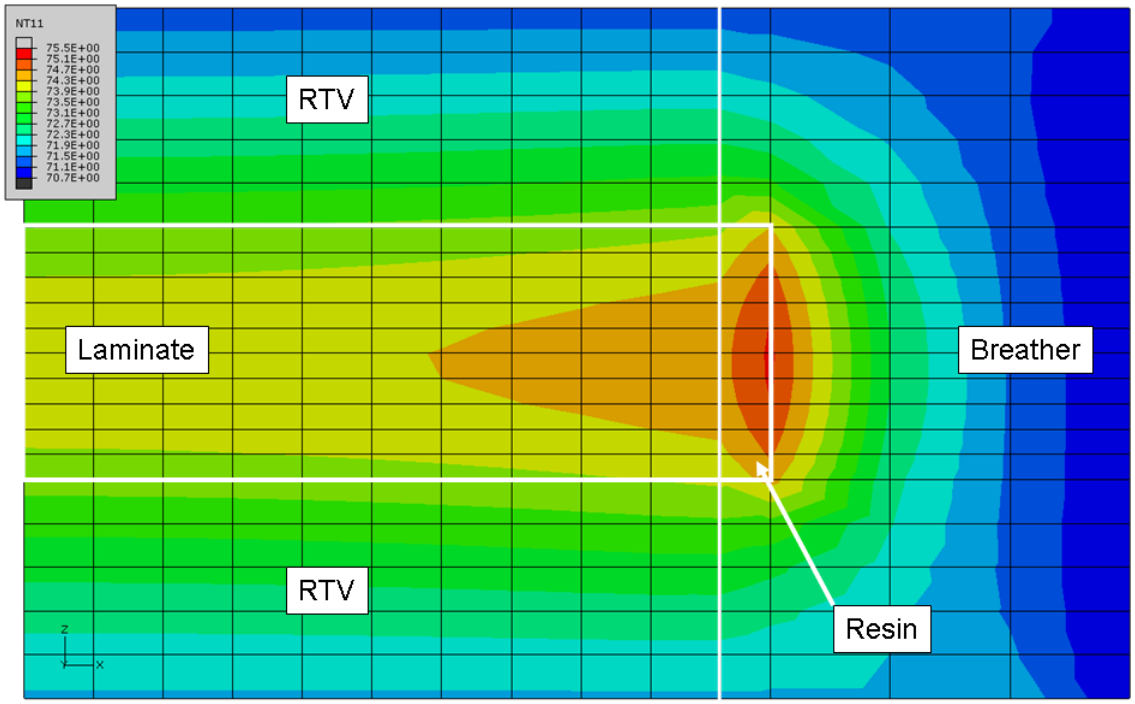

Figure F-3: Temperature contours of in-plane heat transfer from resin block exotherm.

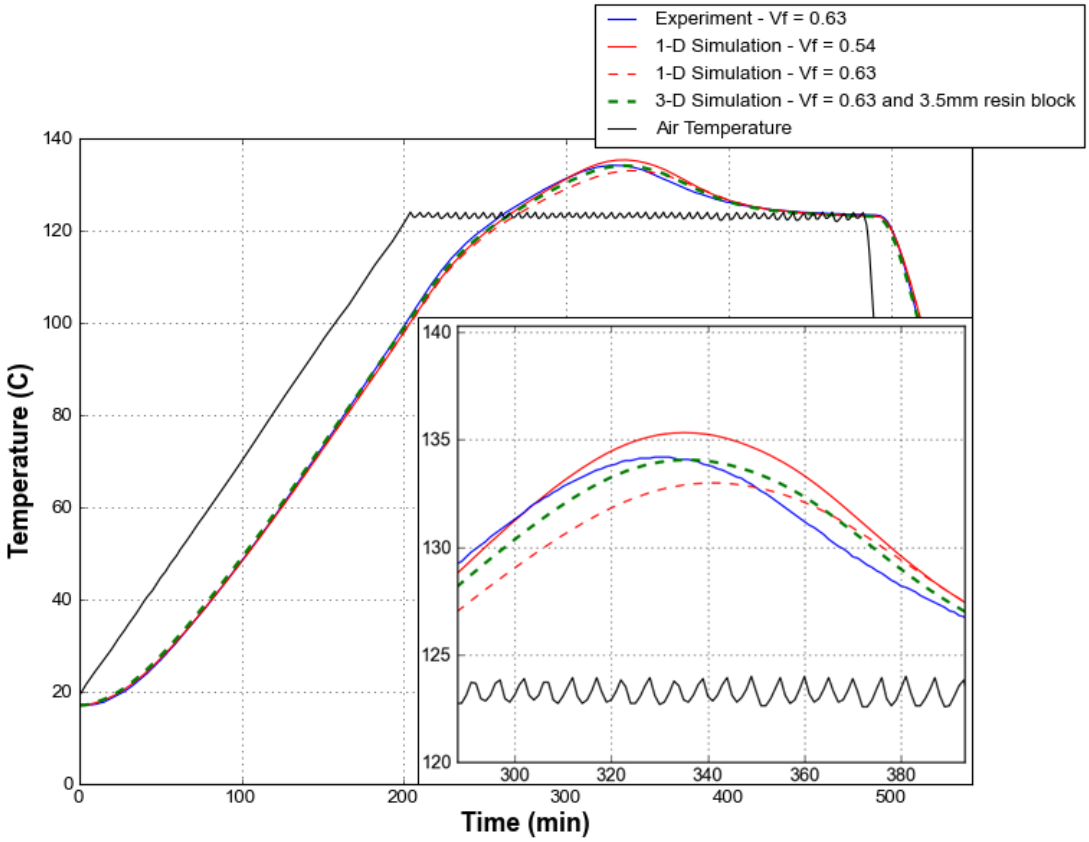

Figure F-4: Comparison of thermal histories for different simulations of 50 ply CF2426A/MTM45-1 laminate. 3-D simulation is the most accurate, but a nominal 1-D simulation is a good approximation due to the in-plane heat flow.